The structure of the southern Dead Sea basin revealed from local earthquake data

Dissertation

zur Erlangung des akademischen Grades

Doktor der Naturwissenschaften

am Fachbereich Geowissenschaften,

der Freien Universität Berlin

vorgelegt von

Benjamin Bräuer

Potsdam, Mai 2011

Erstgutachter: PD Günter Asch

Zweitgutachter: Prof. Michael Weber

Tag der Disputation: 08.07.2011

Erklärung

Hiermit erkläre ich, daß ich die vorgelegte Dissertation selbst verfaßt und mich dabei keiner anderen als der von mir ausdrücklich bezeichneten Quellen bedient habe. Weiterhin erkläre ich hiermit, daß ich an keiner anderen Stelle ein Prüfungsverfahren beantragt, bzw. die Dissertation in dieser oder anderer Form bereits anderweitig als Prüfungsarbeit verwendet oder einer anderen Fakultät als Dissertation vorgelegt habe.

Abstract

While the Dead Sea basin has been studied for a long time, the available knowledge about the detailed seismicity distribution in the area, as well as the deeper structure of the basin, is limited. Therefore, within the framework of the international project DESIRE (Dead Sea Integrated Research Project), a temporary local seismological network was operated in the southern Dead Sea area. 65 stations registered 655 events within 18 month of observation time.

A subset of 530 well locatable events were used to calculate a minimum 1-D model for P - and S - wave velocity. This minimum 1-D model served as an initial reference model for a v_P and v_P/v_S tomography. Since the study area is at first order two-dimensional, a gradual approach was chosen, which compromised a 2-D inversion followed by a 3-D inversion. The sedimentary basin, clearly imaged through low P velocities and high v_P/v_S ratios, shows an asymmetric structure with a vertical eastern boundary and an inclined western boundary. The lower boundary of the basin, indicated by a large gradient of the P velocity, is found at 17 km depth. The boundary between fluid containing sediments, deposited during the formation of the basin, and pre-basin sediments is found between 10 and 15 km depth through contrasts in the v_P/v_S ratios. The Lisan salt diapir is furthermore imaged through low v_P/v_S ratios.

Accurate earthquake locations are only revealed by tomographic inversions. The seismicity is concentrated in the upper crust down to 20 km depth while the lower limit of the seismicity is reached at 29 km depth. The seismic events at the eastern boundary fault in the southern part of the study area, represent the northwards transform motion of the Arabian plate along the Dead Sea Transform. North of the Boqeq fault the seismic activity, mostly related to the contrast between fluid containing sediments and ”dry” rocks, represent the transfer of the motion in the pull-apart basin from the eastern to the western boundary.

Zusammenfassung

Während das Sedimentbecken des Toten Meeres im allgemeinen schon seit langem erforscht wird, ist die genaue Verteilung der Seismizität im Gebiet des Beckens sowie seine tiefere Struktur kaum bekannt. Deshalb wurde innerhalb des internationalen Projekts DESIRE (DEad Sea Integrated REsearch project – Integriertes Forschungsprojekt am Toten Meer) ein temporäres seismologisches Netzwerk im Bereich des südlichen Toten Meeres installiert. 65 Stationen registrierten 655 lokale Erdbeben innerhalb von 18 Monaten.

530 gut lokalisierbare Beben wurden ausgewählt um ein 1-D Geschwindigkeitsmodel für P- und S-Wellen zu berechnen. Dieses 1-D Model wurde dann als Startmodel für eine v_P und v_P/v_S Tomographie verwendet. Da das Studiengebiet in erster Ordnung eine 2-D Struktur aufweist, wurde ein gradueller Ansatz gewählt, bei dem zuerst eine 2-D Tomographie berechnet wird, gefolgt von einer 3-D Tomographie. Das Sedimentbecken, abgebildet durch tiefe v_P und hohe v_P/v_S Verhältnisse, zeigt eine asymmetrische Struktur mit einer senkrechten östlichen Randstörung und einem geneigten westlichen Rand. Die Untergrenze des Sedimentbeckens, angezeigt durch einen hohen Gradient von v_P, wurde in 17 km Tiefe gefunden. Der Übergang zwischen Sedimenten mit hohem Fluidgehalt, abgelagert nach Beginn der Beckenbildung, und den Sedimenten, die sich schon vor Beginn der Beckenentstehung abgelagert hatten, wurde in Tiefen zwischen 10 und 14 km lokalisiert, abgebildet durch starke Kontraste in den v_P/v_S Verhältnissen.

Die genaue Bestimmung von Hypozentren im Untersuchungsgebiet ist nur durch tomographische Inversionsrechnung möglich. Die Seismizität konzentriert sich in der oberen Kruste bis 20 km Tiefe, während die tiefsten Beben in 29 km Tiefe gefunden wurden. Die Seismizität an der östlichen Randstörung im Süden des Untersuchungsgebiets repräsentiert die Nordwärtsbewegung der Arabischen Platte entlang der Toten Meer Transformstörung. Nördlich der Boqeq Störung findet der Transfer der Bewegung im Blattverschiebungsbecken (engl. pull-apart basin) von der östlichen Hauptstörung auf die westlichen Störungen statt. Die Seismizität tritt hier vor allem am Übergang zwischen fluidhaltigen und "trockenen" Gesteinen auf.

Contents

Chapter 1

Introduction

Three types of tectonic plate boundaries are defined for the earth: Convergent or active margins occur where two plates slide towards each other and divergent boundaries occur where two plates slide apart from each other. The third type are transform boundaries, also known as conservative boundaries, where the adjacent plates move along side each other. Such a movement is referred to as strike-slip motion. The most prominent transform faults in the world are the San Andreas Fault in California, the Alpine Fault in New Zealand, the North Anatolian Fault System in Turkey and the Dead Sea Transform (DST) in the Middle East. The seismicity at all strike-slip faults occurs typically at shallow depth, thus, even earthquakes with moderate magnitudes can cause massive destructions.

Oceanic transform faults usually connect segments of mid-ocean ridges in scales of tens to hundred kilometers, while continental transforms usually occur in more complex tectonic settings and can reach a length of more than thousand kilometers. A characteristic for continental transform faults is the more complex structure due to the previous deformation and faulting of the continental crust. This reflects in a generally inhomogeneous nature of continental crust, which may contain e.g. ancient lines of weakness along which rupture occurs preferentially (e.g. Kearey and Vine [1995]). The strike of faults therefore may depart from a simple linear trend, and the curvature of strike-slip faults gives rise to zones of compression and extension [Maercklin, 2004]. Compression results in structures like pressure ridges while in zones of extension pull-apart basins can arise. In such a case, the crust is literally ”pulled apart” in the section between the two strike-slip faults forming a large sedimentary basin.

The Dead Sea basin (DSB) is often referred to as a typical example for a pull-apart basin. It will be in the focus of this thesis. The DSB is a large sedimentary basin and hosts the world deepest depression on land. It can serve as an example for other sedimentary basins along the DST and also at other transforms faults in the world. The general question is why and how plate movement opens deep basins in the crust. Though the DSB has been studied for a long time, the available knowledge - based mainly on surface geology, drilling and seismic reflection surveys - gives only a partial picture of its shallow structure. The fault pattern at depth and the structure at mid- and deep-crustal levels are little known and poorly understood. The question is thus how the surface deformation of the transform widens in the crust and the underlying mantle.

Compaction and fluid content are important properties, with different values for various types of rocks. The elastic parameters, strongly influenced by these properties, control the seismic wave propagation. By imaging acoustic- and shear wave speed, the spatial distribution of the elastic parameters, and thus the different properties, of the rocks can be derived.

These topics have been in focus of the international and multi-disciplinary research project DESIRE (**DE**ad **S**ea **I**ntegrated **RE**search Project), funded by the *Deutsche Forschungsgemeinschaft* (DFG). It was planed and carried out by the following institutions: German Research centre for Geosciences (GFZ) in Potsdam; University of Kiel; Federal Institute for Geoscience and Natural Resources (BGR); University of Frankfurt/Main; Geophysical Institute of Israel (GII); University of Tel Aviv; Hebrew University of Jerusalem; Natural Resources Authority (NRA), Jordan; An-Najah National University Nablus, Palestine. Geologic, petrologic, geodetic and geophysical data have been acquired and analyzed to provide a detailed picture of the DSB and its formation. DESIRE is following the DESERT (**DE**ad **SE**a Rift **T**ransect) project from 2000, which was carried out ninety kilometers farther south in the Arava valley.

This thesis helps to answer the questions raised above by analyzing local earthquake data.

The tectonic setting and the evolution of the DST is described in Chapter 2. A more detailed description concentrates on the structure of the DSB, including its boundary faults and the sedimentary history. A short overview about paleo-, historical and recent seismic activity in the region is also given in this section. The data acquisition and preprocessing, including event detection and arrival time determination, is described in Chapter 3.

The theory and methods used for the different analysis is outlined in Chapter 4. Three methods, all based on the concept of inversion of travel time data, are introduced and described briefly.

A restricted dataset is used to construct a minimum 1-D velocity model for P- and S- waves derived from travel time data. This is the subject of Chapter 5.

Local earthquake tomography technique is used to investigate the structure of the basin in detail in Chapter 6. Resolution and stability tests are made to verify the results of the inversion.

The distribution and size of the earthquakes is presented in Chapter 7. A spatial and temporal cluster of earthquakes is analyzed in detail using a double difference relocation procedure. The focal plane solutions for the largest events of the dataset are furthermore presented.

In the discussion in Chapter 8 the distribution of the seismicity in the southern Dead Sea basin is combined with the results of the tomography and together they are compared to results of other investigations in the area.

The conclusions and an outlook are given in Chapter 9.

Chapter 2

Geology and Seismicity of the DST

2.1 Regional Setting

The Dead Sea transform (DST) crosses a continental area that was consolidated during late Proterozoic Pan-African Orogeny. The region then became a stable platform, on which sediments of continental and shallow marine origin were deposited in several periods from the Cambrian to the Early Cenozoic [Ben-Avraham et al., 2008]. Probably in Permian, Triassic and Early Jurassic times rifting activity occurred, which was related to the formation of the eastern Mediterranean branch of the Neo-Tethys and shaped its passive margins [Garfunkel and Ben-Avraham, 1996]. In the Late Cretaceous, the closure of the Neo-Tethys started, accompanied by mild compressional deformation. The resulting structures are known as the Syrian fold belt, stretching from western Sinai in the southwest to the Palmyrides in the northeast (Figure 2.1). This produced NNE-SSW to ENE-WSW-trending faults, and lineaments trending close to east-west, along which right-lateral shearing of up to a few kilometers took place. The latter is the central Negev-Sinai shear belt [Bartov, 1974] which extends across Sinai and the central Negev to about 200 km east of the Dead Sea.

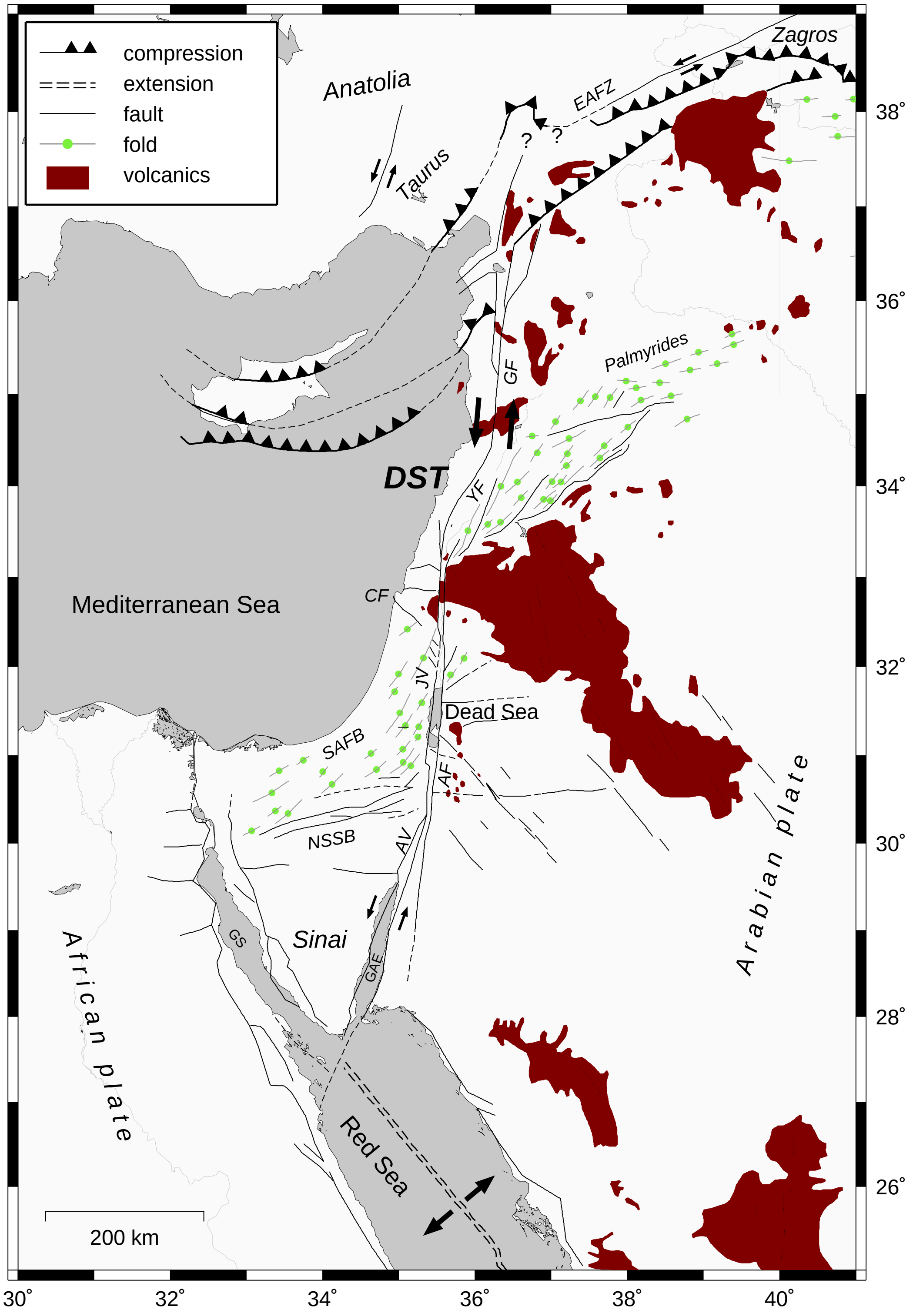
compression
extension
fault
fold
volcanics
Anatolia
Zagros
EAFZ
Taurus
? ?
GF
Palmyrides
DST
YF
CF
Mediterranean Sea
JV
Dead Sea
SAFB
AF
NSSB
AV
Sinai
GS
GAE
Arabian plate
African plate
Red Sea
200 km
38°
36°
34°
32°
30°
28°
26°
30°
32°
34°
36°
38°
40°

Figure 2.1: Tectonic setting of the Dead Sea Transform (DST) in the Middle East, compiled after Garfunkel [1981, 1997] and Salamon et al. [1996] from Maercklin [2004]. Arrows indicate directions of relative motion at faults. Abbreviations: AV - Arava Valley, AF - Arava Fault, CF - Carmel Fault, EAFZ - East Anatolian fracture zone, GAE - Gulf of Aqaba/Elat, GF - Ghab Fault, GS - Gulf of Suez, JV - Jordan Valley, NSSB - Negev-Sinai shear belt, SAFB - Syrian arc fold belt (including Palmyrides), YF - Yammouneh Fault.

The continental breakup of Arabia from Africa began in the Middle Cenozoic and was accompanied by widespread, predominantly basaltic volcanism (Garfunkel [1981] and references therein). Radiometric dating indicates the initiation of igneous activity in the Oligocene, mainly 35 - 20 Ma. However, major rifting began only after 20 Ma, i.e. in the Miocene, creating the Red Sea through sea-floor spreading. The DST takes up most of the Arabian-African plate motion, but a part of the motion was accommodated by opening of the Suez rift [McKenzie et al., 1970, Joffe and Garfunkel, 1987, LePichon and Gaulier, 1988]. The continuing activity of both lines is evidenced by faulting of young sediments and by ongoing seismicity [Garfunkel and Ben-Avraham, 1996].

The geology of areas facing each other across the DST today is remarkably different due to the lateral motion of juxtaposed areas that were originally far from each other. Various markers matching across the transform indicate a left-lateral offset of approximately 107 km [Quennel, 1958, Freund et al., 1970, Bartov, 1974]. The markers are different sedimentary units of the Cambrian and the Cretaceous from southern Lebanon and southward as well as some features of the basement (Ben-Avraham et al. [2008] and references therein) and magnetic anomalies [Hatcher et al., 1981]. However, across the northern part of the rift ophiolite nappes that were thrust onto the edge of the Arabian platform in the late Cretaceous are offset by 80 km only. Garfunkel [1981] explained this difference with the non-rigidity of the lands bordering the northern half of the DST. Further analysis of the plate kinematics of the opening of the Red Sea, taking into account stretching of its margins and the opening of the Suez rift, indicates a left-lateral motion of approximately 100 km (Ben-Avraham et al. [2008] and references therein). Recent estimates of the current slip rate along the southern segment of the DST range from 1 mm a^{-1} to 10 mm a^{-1} (Maercklin [2004] and references therein). Klinger et al. [2000a] estimate a slip rate of 4 ± 2 mm a^{-1} determined from offset Pleistocene alluvial fans in the Arava valley. On the basis of two Global Positioning System (GPS) campaigns, 6 years apart, at 17 sites distributed in Israel and Jordan, Le Beon et al. [2008] computed the present-day deformation across the southern segment of the DST. Elastic locked-fault modeling of fault-parallel velocities provides a slip rate of 4.9 ± 1.4 mm a^{-1} and a best fit locking depth of ~ 12 km. Even at the northern end of the DST, in south Turkey, Karabacak et al. [2010] found similar results (4.94 ± 0.13 mm a^{-1}) as well as Reilinger et al. [2006] (~ 4 mm a^{-1}) who derived the whole velocity field for the region of the Arabian, African and Eurasian plates by GPS measurements.

The development of the DST was accompanied by uplifting and igneous activity on a regional scale [Ben-Avraham et al., 2008]. Elevations are variable, mostly between 0.7 and 1.5 km, although in some places a 2 - 3 km uplift of the topography can be observed. Prior to the continental breakup, the region crossed by the transform was below sea level until 40 Ma ago. 15-12 Ma ago it was still low enough for the sea to extend 20 - 30 km inland of the present coast [Garfunkel and Ben-Avraham, 1996]. Thus, most of the uplift of the transform flanks occurred during the past 10 Ma while the transform was active. The igneous activity accompanying the transform development is not obviously related to the transform but situated mostly east of it, up to some hundred kilometers away from the fault [Garfunkel and Ben-Avraham, 1996].

While the total slip along the DST, as well as the current slip rate, is known, the history of motion is not well constrained. The youngest markers affected by the entire lateral motion are 20 - 25 Ma old (Miocene) dikes of the Red Sea dike system [Eyal et al., 1981]. Thus, the transform motion must have begun later. The oldest structures that can be associated with the transform are 17 - 18 Ma old basins near Tiberias and under the DS [Garfunkel, 1997, Garfunkel and Ben-Avraham, 2001]. This agrees with the acceleration of the opening of the Gulf of Aden and the Red Sea [Garfunkel and Beyth, 2006]. Magnetic anomalies in the southern Red Sea indicate a maximum of 40 km of displacement along the DST since the onset of oceanic crust accretion in the Red Sea 4.7 Ma ago [LePichon and Gaulier, 1988]. Furthermore, the formation of the Sea of Galilee and the Hula depression, as well as the initiation of the main subsidence of the DSB and the Gulf of Aqaba is dated to be ca. 5 Ma old as well [Garfunkel and Ben-Avraham, 2001]. All this evidence for a change in the kinematics along the DST is explained by a movement of the Eulerian pole of relative plate motion between the African and Arabian plate by about 5° to the East [Garfunkel, 1981, Joffe and Garfunkel, 1987].

From the combination of two seismic refraction profiles crossing the DST perpendicularly across the DST, Mechie et al. [2009] inferred that the DST was formed at the point where the crust starts to thin toward the Mediterranean Sea. This was already hypothesized by El-Isa et al. [1987], assuming that the transform will preferentially form in the thicker, weaker crust at the western edge of the Nubo-Arabian shield than in the thinner, stronger crust in the vicinity of the Mediterranean Sea. At the same point there is a thickening of the sediments deposited prior to the formation of the DST toward the west [Mechie et al., 2009].

The DST can be divided into two segments: south and north of 33.16°N [Ben-Avraham et al., 2008]. The southern part of the DST is marked by conspicuous morphotectonic depressions, 10 - 20 km wide, partly filled by sediments [Garfunkel, 1981]. These are generally delimited by faults indicating normal displacement [Garfunkel, 1981]. It is unclear why the basically left-lateral strike-slip movement along the DST produce rift-like structures which are normally related to extensional regimes. New analogue tectonic modeling experiments [Smit et al., 2010] suggest that the rift-like morphology is a logical consequence of the change in plate kinematics ca. 5 Ma ago which was already suggested by [Garfunkel, 1981]. The models indicate that the near vertical faults that delineate the rift valley were formed as strike-slip faults and further accommodated vertical displacement, during transtension due to the change of the Eulerian pole of relative plate motion 5 Ma ago [Smit et al., 2010]. Furthermore, asymmetric subsidence combined with stronger uplift on the eastern than on the western shoulder is revealed by the models and also found in different parts of the southern DST segment [Ben-Avraham, 1992, Zak and Freund, 1981, Garfunkel and Ben-Avraham, 1996, Neev and Hall, 1979]. The different parts of the southern segment (marked on Figure 2.1) are briefly introduced here.

The Gulf of Aqaba/Elat segment is the widest and the deepest of the whole DST. It is bordered on the east and on the west by normal faults, which are responsible for steep escarpments and submarine slopes. Gravity anomalies indicate that 6 - 8 km thick sedimentary sections exist within the basin [Ben-Avraham et al., 2008]. Three deep basins, which are arranged en-echelon, form the floor of the Gulf [Garfunkel, 1981]. The active structures that define these pull-apart basins are probably relatively young, having formed during the last stages of lateral motion [Garfunkel and Ben-Avraham, 2001].

The Arava Valley/Fault is a 160-km-long morphotectonic depression connecting the Gulf of Aqaba and the DSB. It is a narrow, sub-vertical zone cutting through the entire crust down into the lithosphere [Weber and DESERT Group, 2009]. The Arava Fault is a system of almost pure strike-slip faulting. Similar to the San Andreas Fault, the Arava Fault shows a strong asymmetry in sub-horizontal lower crustal reflectors and a deep reaching narrow deformation zone about 5 km wide in the middle and the lower crust (Weber and DESERT Group [2009] and references therein).

North of the DSB, which is discussed in the next section, the *Jordan Valley* is located, which resembles the Arava valley with a rather simple structured strike-slip fault. In some parts the valley is flanked by volcanic fields of middle Miocene - Quaternary age [Garfunkel, 1981]. Two depressions are part of the valley: The depression of the Sea of Galilee and of Lake Hula, both formed about 5 Ma ago. Both are characterized by a negative gravity anomaly indicating sediment filling. The Sea of Galilee is bigger, older and has a thicker sediment fill than the Hula depression [Garfunkel and Ben-Avraham, 2001].

The northern segment of the DST is remarkably different. The transform bends here to the east, leading to mainly transpressional structures [Maercklin, 2004]. This is in good agreement with the analogue modeling experiments of [Smit et al., 2010], which showed transpressional structures in the north assuming a shift of the Eulerian pole of motion to the East. The transform system is furthermore split into several distinct branches, trending roughly parallel to the strike of the Palmyrides fold range (Garfunkel [1981], Girdler [1990], Gomez et al. [2003], see Figure 2.1). The lateral slip appears to be distributed over the different branches. As the faults observed there do not seem to accommodate the total lateral slip, the Palmyrides represent some internal deformation of the Arabian plate [Maercklin, 2004]. The Ghab fault is the northernmost segment of the DST. It trends N5°E and reaches the Tauros-Zagros collision zone between Arabia and Anatolia.

2.2 Local Setting

The Dead Sea Basin (DSB) is a large sedimentary basin situated at the Dead Sea transform (DST) between the Arava valley in the south and the Jordan valley in the north. The northern part is occupied by the Dead Sea, a salt lake with a salinity of around 330 g kg^{-1} and a decreasing sea level for the last 30 years. The DSB is between 15 and 17 km wide and thought to be 150 km long (e.g. Garfunkel and Ben-Avraham [2001]) as its northern and southern margins are not clearly identified. The area east of the basin forms a plateau 1.0 - 1.4 km above sea level which descends gradually away from the transform. The crystalline basement at about 3 km depth is overlain by rocks of Precambrian and Cretaceous age [Mechie et al., 2009]. The area on the western side reaches only 0.6 - 0.8 km, and rarely 1.0 km, above sea level [Garfunkel and Ben-Avraham, 1996]. Jurassic, Triassic, Permian and Precambrian sequences underlie the exposed Cretaceous rocks [Gilboa et al., 1993] and the basement is reached at about 3 km depth [Mechie et al., 2009].

The DSB contains the lowest point on land on earth at 418 m below mean sea level. The bottom of the Dead Sea in the northern part lies about 700 m below sea level. The northern and southern ends of the DSB do not show any topographic expression. Due to this rift-like morphology the DSB was called 'Dead Sea rift' or 'Dead Sea - Jordan rift' in many older publications (e.g. Quennel [1958], Ginzburg et al. [1979], Kashai and Croker [1987]). However, already Quennel [1958] showed the 107 km shift along the DST which clearly proves that the main movement is left-lateral. This movement is most likely responsible for the development of the DSB, and therefore, most authors agree on the concept of a pull-apart basin (also called ‘strike-slip basin‘ or ‘rhomb-shaped basin‘) for the formation of the DSB (extensive discussion in Garfunkel [1997]). The main strike-slip motion side-steps from the east side of the valley at the southern end of the basin to the west side of the valley north of the basin (e.g. Garfunkel [1981], Gardosh et al. [1997], ten Brink et al. [1993]). However, the characteristic length to width ratio of 1:3, found by Aydin and Nur [1982] who compared 70 different pull-apart basins, is not supported for the DSB where it is 1:6 [Kashai and Croker, 1987]. Furthermore, Niemi et al. [1997] and Shamir [2006] suggest that the DSB cannot be explained as a classical pull-apart basin. The length (150 km) being longer than the entire shift along the DST (107 km) is moreover difficult to reconcile with a pull-apart basin. Only the Step-over Basin model of Aydin and Nur [1982] would explain it. In this model several coalescing basins are formed between a series of overstepping, en-echelon segments of the main strike slip [Lazar et al., 2006]. However, this model would result in non-parallel border faults. Lazar et al. [2006] used seismic data from the northern part of the DSB to refine older models of the development of the DSB. These authors found three main elements controlling the development of the Dead Sea basin system: Motion along the strands of the strike-slip, activity along transverse faults, which divide the basin into sub-basins; and subsequent subsidence of the floor of the sub-basins [Lazar et al., 2006]. Thermo-mechanical modeling of the pull-apart structure including all geological and geophysical knowledge of the area has been carried out by Petrunin and Sobolev [2008]. Their model shows that basin subsidence results from the competition of extension of the brittle part of the lithosphere and of the compensating flow of the deeper ductile part of the lithosphere, which pushes the extended brittle block upwards. The formation of the deep narrow DS pull-apart basin in relatively cold lithosphere (indicated by a low heat flow of 40 mW/m^2 [Ben-Avraham et al., 1978]) requires very low friction at the major faults [Petrunin and Sobolev, 2008].

Some authors point out the asymmetry of the basin in the E - W direction with a deep and nearly vertical eastern boundary fault (EBF) and a shallower western boundary fault inclined to the east [Neev and Hall, 1979, Zak and Freund, 1981, Garfunkel and Ben-Avraham, 1996, Garfunkel, 1997, Shamir, 2006]. Ben-Avraham and Zoback [1992] introduced, as an alternative to the idea of a pull-apart basin, the concept of an asymmetric basin with transform-normal extension (in addition to the main left-lateral motion) explained by a weak transform fault embedded in a strong crust. In an asymmetric basin, one of the two boundary faults (here the eastern boundary, Figure 2.2) is approximately vertical and shows a strike-slip movement, while the other boundary fault (here the western boundary, Figure 2.2) is flatter and shows primarily transform - normal extension, i.e. normal faulting [Ben-Avraham and Zoback, 1992]. This is supported by magnetic measurements from Frieslander and Ben-Avraham [1989] in the northern part of the basin. These authors found magnetic anomalies crossing the western faults (WF) uninterrupted, indicating normal faulting along the western side of the basin. Meanwhile, across the eastern border fault magnetic contours are discontinuous, suggesting predominant strike-slip motion resulting in major lithological changes across the eastern border fault. However, an E-W reflection seismic line across the southern DSB suggests a full graben, at least for the upper part visible in the seismic section [Al-Zoubi et al., 2002].

2.2.1 Stratigraphy

The initiation of the formation of the DSB was 18 - 15 Ma ago [Garfunkel, 1981, Garfunkel and Ben-Avraham, 1996] between the Arava fault in the southeast and the Jericho fault in the northwest (see Figure 2.2). Stratigraphic analysis of the DSB fill [Kashai and Croker, 1987, Garfunkel, 1997] points out that already in the early and middle Miocene the DSB became an accentuated depression [Horowitz, 1987]. More than half of its present length was filled with several kilometers of clastics until the late Miocene. These clastics, called Hazeva Formation, were deposited outside the area of the transform as well. A river system flowed across the DSB and deposited these

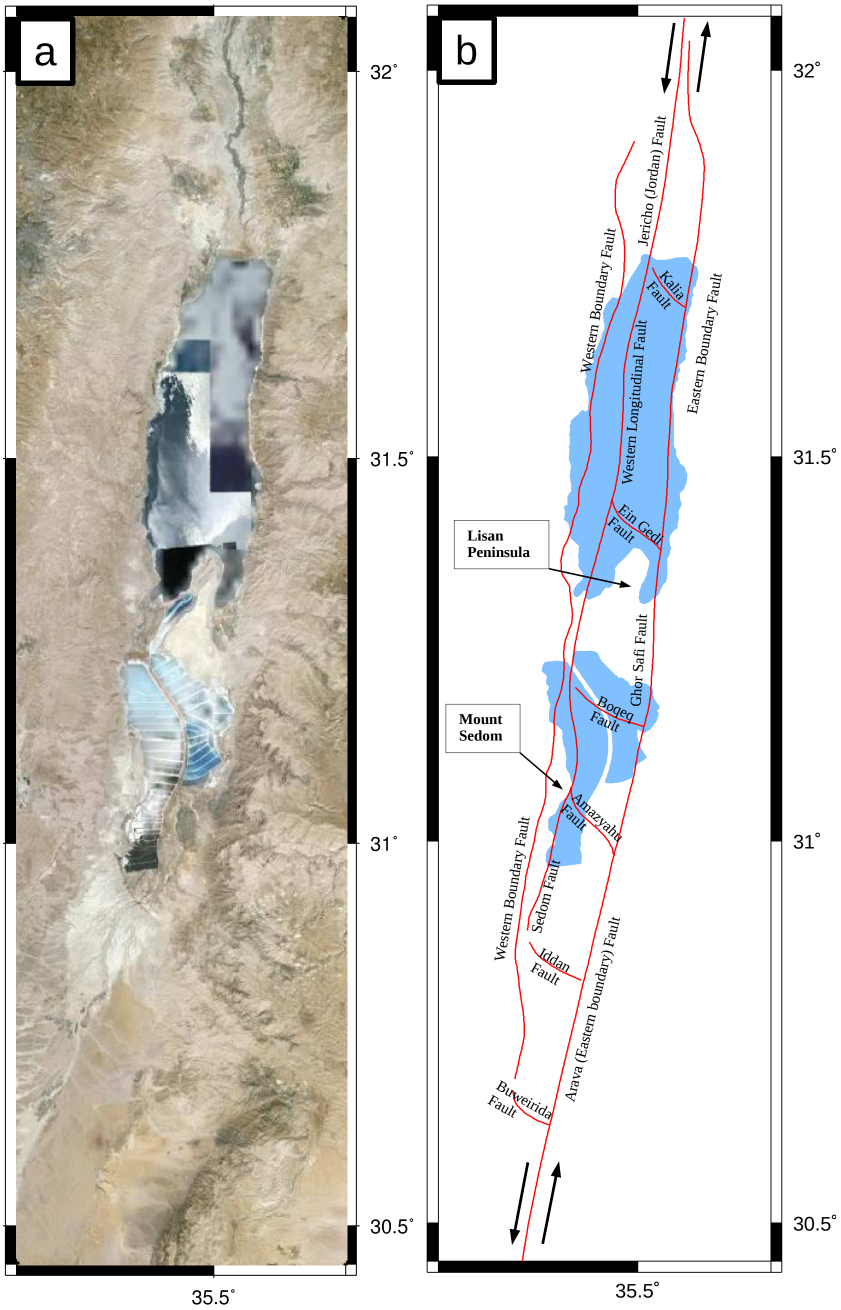

Figure 2.2: Satellite image from the DS region (a). Main faults of the DS region from Garfunkel [1997], Larsen et al. [2002], Smit et al. [2008] (b). The areas which are covered with water recently are marked in blue. The Western Boundary fault, the Western Longitudinal fault and the Sedom fault are summarised as Western faults (WF) in the following Chapters.

clastics, showing that subsidence was interrupted at that time and the basin flanks had not yet formed topographic barriers (Garfunkel [1997], Garfunkel and Ben-Avraham [2001] and references therein). Subsequently, an arm of the Mediterranean reached the DSB most probably from the north resulting in marine sedimentation. The Sedom Formation, consisting predominantly of halite, was deposited in a ca. 70 km long segment in the northern part of the DSB, whereas its southern part stopped subsiding [Garfunkel and Ben-Avraham, 2001]. From different seismic reflection profiles in the area of the Lisan peninsula an original thickness of about 2 km is assumed for the Sedom Formation in the southern Dead Sea basin (SDSB) [Al-Zoubi and ten Brink, 2001, Larsen et al., 2002] while today the layer is about 1 km thick as part of the salt ascended as Lisan and Sedom diapir [Al-Zoubi and ten Brink, 2001]. This is also supported by recent teleseismic P-wave tomography studies [Hofstetter et al., 2000] excluding salt as a main component of the basin fill [Ben-Avraham and Lazar, 2006]. The extent of the salt layer in the northern DSB is not well known [Al-Zoubi and ten Brink, 2001]. A Pliocene age is obtained for the evaporites in the Dead Sea from palynological dating [Horowitz, 1987] but also a late Miocene age would be possible [Garfunkel and Ben-Avraham, 2001]. The subsidence during the deposition is explained by the onset of the transtensional motion along the southern DST in early Pliocene 5 Ma ago.

Sometime later in the Pliocene, the connection with the sea was cut and the valley became a land-locked depression in which lakes of varying size - depending on climate fluctuations - developed. Since then clastics, some evaporites and carbonates of fluviatile and lacustrine origin were deposited in the northern part of the basin forming a layer of almost 4 kilometers thickness [Al-Zoubi and ten Brink, 2001]. A deep topographic depression developed because sedimentation lagged behind subsidence (Garfunkel and Ben-Avraham [2001] and references therein). The current surface geology for the Dead Sea region is presented in Figure 2.3.

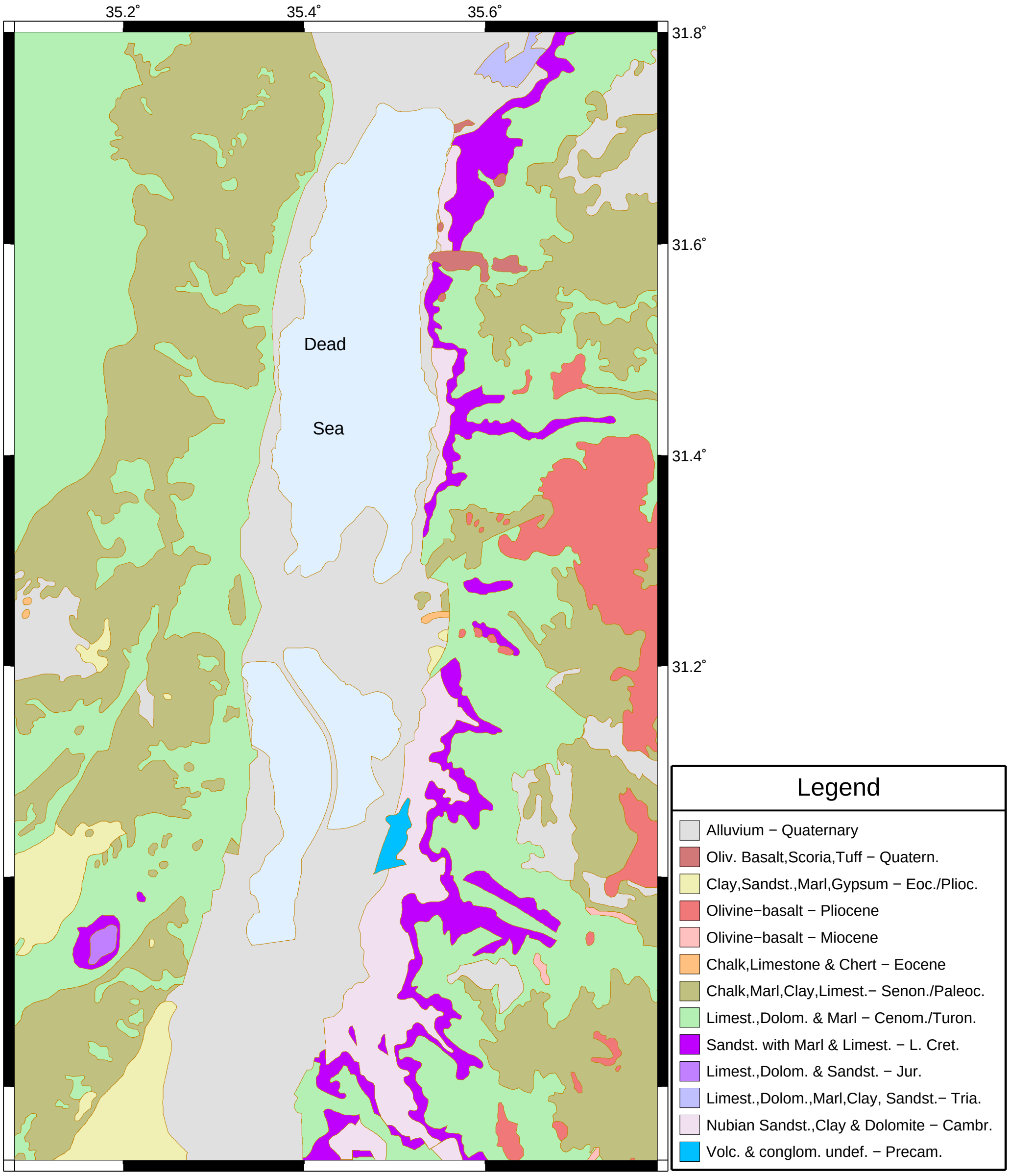

Figure 2.3: Geological map, simplified from Bartov [1990], of the Dead Sea region.

2.2.2 Structure

The structure of the DSB is dominated by longitudinal intra-basinal faults, the extensions of the Arava and Jericho master faults [Garfunkel and Ben-Avraham, 2001, Garfunkel, 1997] which accommodate the main left lateral movement responsible for the basin formation (Figure 2.2). The basin is furthermore bounded to the west by normal faults accounting for the secondary extensional motion. Following e.g. Garfunkel and Ben-Avraham [1996] it is crossed obliquely by several transverse faults that divide it into different segments with different depths. These transverse faults, trending mostly NW-SE obliquely across the basin, are observed in all parts of the basin [Ben-Avraham and Ten Brink, 1989]. The Buweirida fault (Figure 2.2), a N-facing scarp which extends across the Arava valley, is the southernmost of these faults [Garfunkel, 1997]. However, since recently this fault is not considered to be part of the DSB as the Iddan fault farther north is found to form the southern end of the DSB (e.g. Larsen et al. [2002], Ben-Avraham and Lazar [2006], Figure 2.2). This discrepancy in the definition of the southern end of the DSB, as well as the vague northern end of the basin where no transverse fault forming a clear boundary is found, results in the varying interpretations of the length of the DSB (107 km deduced from the amount of displacement of the DST, e.g. Larsen et al. [2002]; 135 km, ten Brink et al. [1993]; 150 km, e.g. Ben-Avraham and Lazar [2006]; 230 km, Shamir [2006]). Larsen et al. [2002] used reflection seismic data tied to data from wells in the area to analyze the southernmost transverse faults in detail. The N-facing Iddan fault borders the DSB to the south and the salt layer previously suggested to finish further north, reaches as far south as the Iddan fault. The Amazyahu fault further north was for a long time thought to be a listric fault facing north but not reaching the top of the basement (e.g. Csato et al. [1997]). Its formation was believed to be the result of extension due to salt withdrawal [Larsen et al., 2002]. New processing of previous seismic data across the southern DSB suggests that the Amazyahu fault is indeed a normal fault cutting through the sedimentary section down to the crystalline basement [Ginzburg et al., 2007]. As the next transverse fault to the north, the S-facing Boqeq fault is suggested, forming the southern border of the Lisan peninsula [Larsen et al., 2002, Ben-Avraham and Ten Brink, 1989] while Al-Zoubi and ten Brink [2001] interpret this area as the edge of the Lisan diapir without an active fault. The Lisan diapir is bordered to the north by the Ein Gedi fault according to Ben-Avraham and Ten Brink [1989]. Rotstein and Arieh [1986] found seismic activity in the area of the Ein Gedi fault but their location accuracy was limited due to the small number of stations at the time of their investigation. The Kalia fault (Figure 2.2), mapped in seismic cross sections by Lazar et al. [2006], is the only transverse fault which can be clearly assigned to seismic activity namely the 11th February 2004 ($M_W = 5.1$) event. In particular, its aftershock distribution clearly represents a fault trending NW-SE [Hofstetter et al., 2008]. All of the events occur at around 15 km depth, which indicates a deep-rooted fault. None of the previously mentioned faults are identified to this depth as all reflection seismic profiles (e.g. Larsen et al. [2002], Al-Zoubi et al. [2002]), mainly used for the identification of the transverse faults, are limited by the salt layer (Sedom formation) at a depth of around 5 km. North of the Kalia fault the eastern and western boundary faults start to converge, which is likely to be the end of the basin (Lazar et al. [2006], Figure 2.2).

The DSB is divided into a northern and a southern sub-basin, separated by the Lisan Peninsula (see Figure 2.2). The slight topographic height, forming the Lisan Peninsula, is due to a large buried salt diapir below it, which is probably bounded to the north and south by the oblique normal faults [Ben-Avraham et al., 2008]. Seismic data correlated to several deep wells determined the size of the Lisan diapir to be 13 x 10 km with a maximum depth of 7.2 km and its roof 125 m below the surface [Al-Zoubi and ten Brink, 2001]. These authors inferred from seismic stratigraphy that the diapir started rising during the early Pleistocene as the basin underwent rapid subsidence and significant N-S extension of the overburden. The salt of the diapir comes from the Sedom formation, which gets its name from the second diapir in the basin, the Sedom diapir (below Mount Sedom in Figure 2.2) in the southwest of the basin. This diapir has pierced the surface during the Holocene, creating an $\sim$200 m high ridge [Al-Zoubi and ten Brink, 2001, Zak, 1967] where a ca. 2 km thick section is exposed. Its formation is assigned to a local compression due to the rotation of the Amazyahu fault which squeezes the diapir laterally [Al-Zoubi and ten Brink, 2001].

A north-south seismic refraction profile shows a considerable difference between the northern and southern sub-basins [Ginzburg and Ben-Avraham, 1997]. Whereas the northern sub-basin appears to be filled with a 6-8 km thick sediment sequence in the southern sub-basin 14 km of sedimentary fill is suggested. The difference between the north and the south may indicate that the northern sub-basin is younger than the southern one or that greater subsidence was prevalent in the southern basin [Ben-Avraham and Lazar, 2006]. The southern DSB, the largest part of the study area, is furthermore characterized by the largest negative teleseismic P-wave velocity anomaly in a tomography study for the whole of Israel suggesting also sediments thicker than 10 km for the SDSB [Hofstetter et al., 2000]. This is confirmed by a seismic refraction profile [Mechie et al., 2009] crossing the DSB W-E in the area of the Lisan peninsula (Figure 2.2). These authors furthermore suggest only a small variation of the Moho below the DSB, contradicting e.g. Garfunkel [1997], and a boundary between the upper and lower crust at 20 km depth acting as a decoupling zone. Thus, the DSB does not follow the classical behaviour of sedimentary basins with crustal thinning related to the amount of subsidence due to the requirement of isostatic equilibrium. Instead, it seems to be an upper crustal feature with small to no effects of crustal thinning and mantle upwelling [Mechie et al., 2009]. P-wave velocity models deduced from the refraction profile show that the sedimentary fill is about 11 km, of which about 8.5 km are associated with the formation of the basin and about 2 km of older sediments, deposited before the basin formation [Mechie et al., 2009]. The only reflection seismic profile available for the SDSB crossing the whole basin E-W is from Al-Zoubi et al. [2002], and is actually a combination of two profiles running from the western shore to the Israel-Jordan border and from the border to the eastern shore of the basin, respectively. The upper 6 km of the basin and both shoulders are mapped including the Sedom diapir and the upper sedimentary layers within the basin. The thickness of the uppermost Pleistocene layer is found to be about

4000 m consisting of marl, clay, sand, gravel and some evaporites as revealed from deep wells in the area. Underneath, the Pliocene salt layer is identified. Thereunder, the thickness of the fluviatile - lacustrine Miocene layer is not recognizable. This limits the area resolvable by reflection seismic experiments to the uppermost 6 km. Al-Zoubi et al. [2002] identified furthermore a rim block and an intermediate block on each side of the basin, concluding that the SDSB is a full graben.

A magnetotelluric W-E profile crossing the SDSB over the Lisan peninsula was presented by Meqbel [2009]. He identified the Lisan diapir as a resistive body, concluding that it is composed of dry salt with low porosity. A P-wave first-arrival tomography from a seismic reflection experiment crossing the SDSB along the same profile as Meqbel [2009] identified the Lisan diapir through relatively high velocities [Paschke, 2009]. The Pleistocene sediments west of the diapir show low P-wave velocities and very low resistivity, indicating that the DS brines reach depths of several kilometers. Furthermore, the (EBF) seems to be nearly vertical as imaged through sharp contrasts in resistivity and P-wave velocity [Paschke, 2009] while the western faults (WF) shows no sharp contrast in resistivity [Meqbel, 2009].

A detailed interpretation of the seismic, gravimetric and wells data for the SDSB is given in Ben-Avraham and Schubert [2006]. The reprocessing of seismic reflection data brought these authors to the conclusion that the SDSB is bounded by deep rooted faults in all directions and the Amazyahu fault in the middle is a basement fault, following Ginzburg et al. [2007]. Together with gravity models they interpret the SDSB as a full graben divided into two sub-basins by the Amazyahu fault which forms the border between the shallower southern part (about 10 km deep) and the extraordinarily deep northern part (about 14 km deep). Hence, Ben-Avraham and Schubert [2006] introduced a deep 'drop down' model for the northern sub-basin of the SDSB in which the whole lithosphere beneath it is dropped down with respect to the surroundings, right at the start of the formation of the DSB. According to that study the northern part of the SDSB is filled with 8 km of Pliocene to recent sediments overlying 4-5 km of Cretaceous and pre-Cretaceous sediments which were deposited before the formation of the DSB.

2.3 Regional and Local Seismicity

The paleoseismicity of the DST was investigated extensively by different authors. Marco et al. [1996] studied the temporal distribution of earthquakes in the DSB from a 50,000 - year paleoseismic record recovered in laminated sediments of the Late Pleistocene Lake Lisan (paleo Dead Sea). These authors identified layers composed of mixtures of brecciated laminae as seismites, e.g. earthquake-induced deformations of the sediment. Assuming that each mixed layer is a seismite that was formed in a single, $M_L \geq 5.5$ event the recurrence period of stronger earthquakes in the Dead Sea graben is about 1.6 ka. Begin et al. [2005] re-examined sections of the Lisan Formation in order to find a way to distinguish between moderate ($M_L \approx 5.5$) and large ($M_L \geq 7$) events. Considering both the thickness of the breccia beds and the lithology of beds directly overlying them eleven $M_L > 7$ earthquakes were identified that originated in the DSB between 54 and 16 ka. The time interval between consecutive earthquakes increased from hundreds of years to a background recurrence interval of ~ 11 ka since ca. 40 ka. Since this recurrence interval is similar to the $M_L > 7.2$ recurrence interval in the DSB, as extrapolated from present seismicity, the present seismic regime in the DSB, as reflected in its magnitude-frequency relationship as well as in its deficiency in seismic moment, has been stationary for the past 40 ka (Begin et al. [2005] and references therein). Hamiel et al. [2009] even suggested a period of 60,000 years through which the DST moves with a constant slip rate deduced from frequency-magnitude relations. Furthermore these authors see evidence for an unchanged Gutenberg-Richter relation in this time span. Three different areas were therefore investigated [Hamiel et al., 2009]: The Arava valley in the south, the DSB and the Jordan valley in the north (see Figure 2.4). The calculated b-values (from paleoseismic as well as from historical records) for all three segments are between 0.85 and 1, similar to other major strike-slip faults in the world. Shapira and Feldmann [1987] state that a b-value of 0.8 most likely persists the same along the whole DST while they determined a-values between 3.2 and 3.5 for earthquakes of $2 \leq M_L \leq 4$.

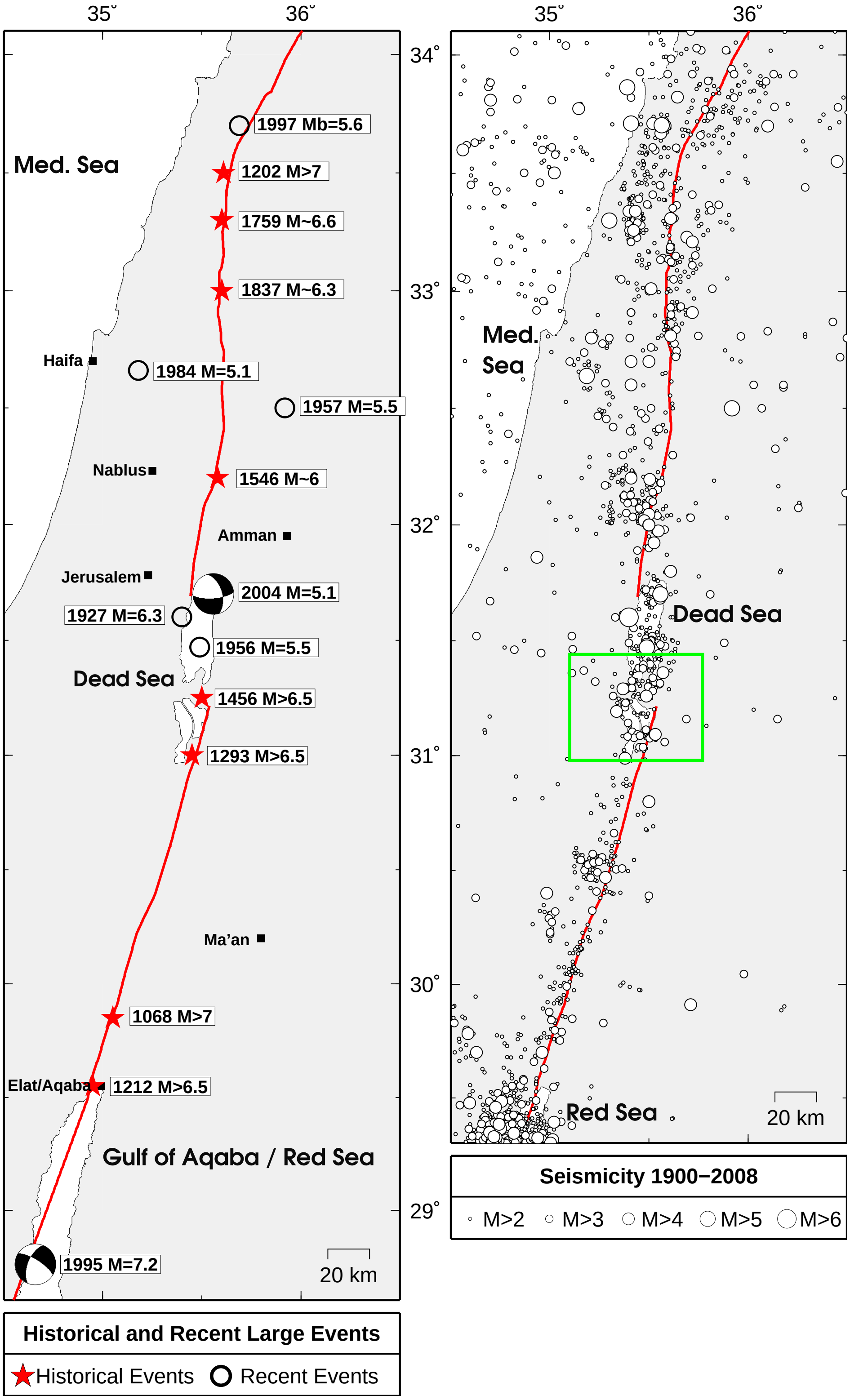
35°
36°
34°
33°
32°
31°
30°
29°
Med. Sea
1997 Mb=5.6
1202 M>7
1759 M~6.6
1837 M~6.3
Haifa
1984 M=5.1
1957 M=5.5
Nablus
1546 M~6
Amman
Jerusalem
2004 M=5.1
1927 M=6.3
1956 M=5.5
Dead Sea
1456 M>6.5
1293 M>6.5
Ma'an
1068 M>7
Elat/Aqaba
1212 M>6.5
Gulf of Aqaba / Red Sea
1995 M=7.2
20 km
Historical and Recent Large Events
Historical Events
Recent Events
Med. Sea
Dead Sea
Red Sea
20 km
Seismicity 1900–2008
M>2
M>3
M>4
M>5
M>6

Figure 2.4: (left) Historical events from 1000-1900 and events with $M > 5$ of the last century along the southern part of the DST. For the 11/02/2004 event the focal plane solution is shown. (right) Seismicity in the southern part of the DST between 1900 - 2008 [Hofstetter, personal comm.]. The green box indicates the study area.

The earthquake database in the historical timescale is extraordinarily good for the DST area. The Middle East is one of the rare regions in the world where evidence for earthquake activity has been documented over the past four millenia. Ben-Menahem [1991] identified forty-two earthquakes in the magnitude range $6.7 \leq M_L \geq 8.3$ originating along the DST during the past 2500 years. The known locations for events within the past millennium are indicated in Figure 2.4. In the DS region proper most of the seismic activity in the last 4100 a has been confined to the vicinity of its eastern shore [Ben-Menahem, 1991].

Seismicity analysis in the 20th century [Salamon et al., 1996] and geomorphological studies [Klinger et al., 2000b] lead to potential recurrence intervals of 385 a and about 200 a, respectively, for earthquakes with a moment magnitude $M_W = 7$ along the DST. Salamon [2010] investigated historical material in order to look for damaging earthquakes and clustered event sequences. For the last 2000 a he found evidence for about a hundred damaging earthquakes in and around the DST, about half of which were associated with additional felt shocks. Thirty-five mainshock-aftershock sequences were noted, lasting between hours and more than a year.

Instrumental recording of earthquakes started at the beginning of the last century. Figure 2.4 shows the distribution of the seismicity along the southern DST for the time from 1900 - 2008 [Hofstetter, personal comm.], where the DSB is one of the active parts. The first major earthquake in the area to be recorded instrumentally, which was also the strongest seismic event ($M = 6.2$) in the 20th century, occurred on June, 11th in 1927. It caused massive destructions in many places around the DS as e.g. Jerusalem, Jericho and Ramleh. 285 people were killed and about 1,000 injured. Its original identified location 40 km north of the DS was corrected to a location on the northwestern coast of the DS (Avni et al. [2002] and references therein, Figure 2.4). Another larger earthquake occurred in the northern DSB on the Feb., 11th in 2004 ($M_W = 5.1$, $Depth = 17$ km), but at the eastern shoulder of the DS (Hofstetter et al. [2008], Figure 2.4). Its focal plane solution represents the regional left lateral strike slip motion along the DST. However, its aftershocks are not distributed along the main fault but perpendicular to it [Hofstetter et al., 2008]. Thus, they represent the Kalia fault, one of several transverse faults trending NW-SE (Garfunkel and Ben-Avraham [1996], as discussed in Section 2.2).

The largest event recorded instrumentally at the DST was the 22/11/1995 Gulf of Aqaba earthquake with a magnitude $M_W = 7.3$ [Klinger et al., 1999]. It occurred on the eastern border of the Aragonese Deep, one of three asymmetric pull-apart basins in the Gulf of Aqaba (Figure2.1) [Ben-Avraham, 1985, 1992]. Analysis of the focal mechanism shows a clear left lateral strike slip motion parallel to the major DST. An aftershock series occurred, from which teleseismic moment tensor inversions confirm the long term left lateral motion along the DST [Hofstetter et al., 2003].

Beginning in 1984 a permanent seismic network was installed in Israel, which enabled to monitor the microseismic activity at the DST. Combined with data from a mobile seismic network Rotstein and Arieh [1986] presented the first picture of the distribution of the microseismicity along the DST, where the DSB shows a remarkable activity. van Eck and Hofstetter [1990] confirmed this observation with a significantly longer observation time of 8 a and found also seven spatial clusters of events with similar waveforms. The long term left lateral motion on the DST is represented through the earthquake mechanics shown in van Eck and Hofstetter [1989] and van Eck and Hofstetter [1990]. However some events in the DSB show clear normal faulting indicating a transtensional regime (e.g. Garfunkel [1981]). In the study of van Eck and Hofstetter [1989], which is focused on the DS region, the seismicity in the SDSB is concentrated at the eastern and western boundary faults, including some spatial clusters on both sides.

All these studies made with data only from stations in Israel suffer from the lack of stations east of the two active faults, resulting in limited depth accuracy of the earthquakes. Aldersons et al. [2003] overcome this problem by also using stations from Jordan and found that most of the earthquakes nucleated between 20 and 32 km depth, thus in the lower crust, while the upper mantle appears to be aseismic for the 14-year observation period.

Begin and Steinitz [2005] outlined the observations of the seismic activity along the DST for the 20 a period 1984 - 2004. The earthquake catalog presented is complete for events with $M \leq 2$ from 1986. Begin and Steinitz [2005] used a relationship between fault offset and the annual number of earthquakes ($M \leq 3$) per km fault length, normalized per 1 mm of annual slip rate of Wesnousky [1990] to show that the DST is comparable to the San Andreas Fault.

Nevertheless, focused on the SDSB, Figure 2.5 shows clearly the limits of the dataset of Begin and Steinitz [2005]. Due to the fact that only israeli stations (all located west of the border faults) are used to locate the events, the accuracy of the locations is limited. The events seems to be randomly distributed over the DSB, showing no concentration on any of the known or other faults while the depth limit of 31 km also looks quite artificial. From the catalog of Begin and Steinitz [2005] about 50 - 60 local events per year are to be expected for the SDSB, assuming a threshold magnitude of $M = 1$.

Hofstetter et al. [2007] used data from stations on both sides of the basin in Israel and Jordan to determine the regional stress tensor and focal mechanisms. The long term left lateral motion is recovered by the most focal mechanisms showing strike-slip faulting. However, also normal faulting components are detected to some extent. For the DSB strike-slip faulting also dominates. However, some events show right lateral faulting instead of the left lateral direction of the large scale movement at the DST. Hofstetter et al. [2007] speculate about a movement on secondary faults striking E-W to explain this [Ben-Avraham and Zoback, 1992, Gilat, 1991].

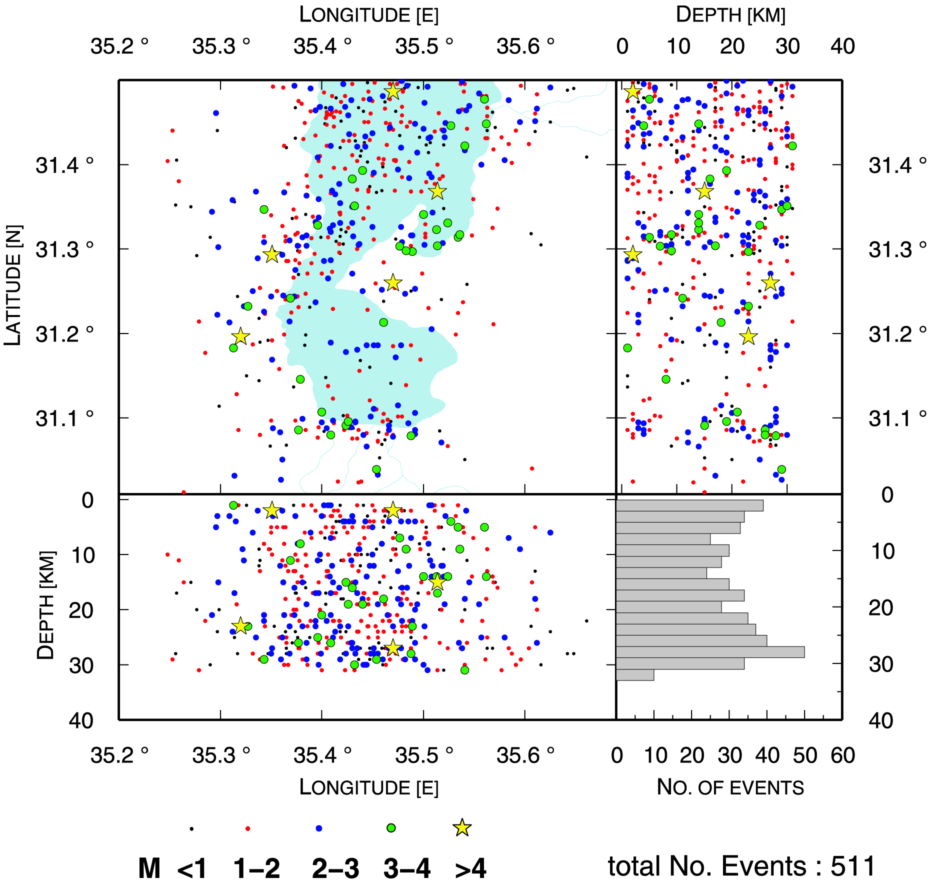

Figure 2.5: Distribution of the seismicity in the southern part of the Dead Sea area from the catalog of Begin and Steinitz [2005], Figure from Asch [personal comm.].

Chapter 3

Experiment and Data processing

3.1 Experimental setup

For the study presented here, between October 2006 and March 2008 a dense seismic network consisting of 65 stations was deployed in the Dead Sea region, with emphasis on the south, covering the Dead Sea basin as well as the shoulders east and west of it (Figure 3.1). The network was installed and maintained by the German Research centre for Geosciences (GFZ) located in Potsdam supported by the Geophysical Institute of Israel (GII), the Natural Resources Authority (NRA) in Jordan and the An-Najah National University in Palestine.

Figure 3.1: Site map of the DESIRE seismograph network. Used stations of the permanent networks in Israel and Jordan are also indicated. Some of them are located outside the area of this map. The areas which are covered with water recently are marked in blue: in the north the natural Dead Sea, in the south the evaporation ponds which are filled artificially with water to harvest minerals through evaporation. The dashed line shows the coastline from 1967 [Neev and Hall, 1979] indicated in many previous maps of the area. The red box is indicating the original study area which will be the section shown in most of the figures in the following chapters, e.g. Figure 5.3 auf Seite 51. On the bottom a topographic profile from West to East at LAT 31.25° is shown with the see level indicated by a dashed line.

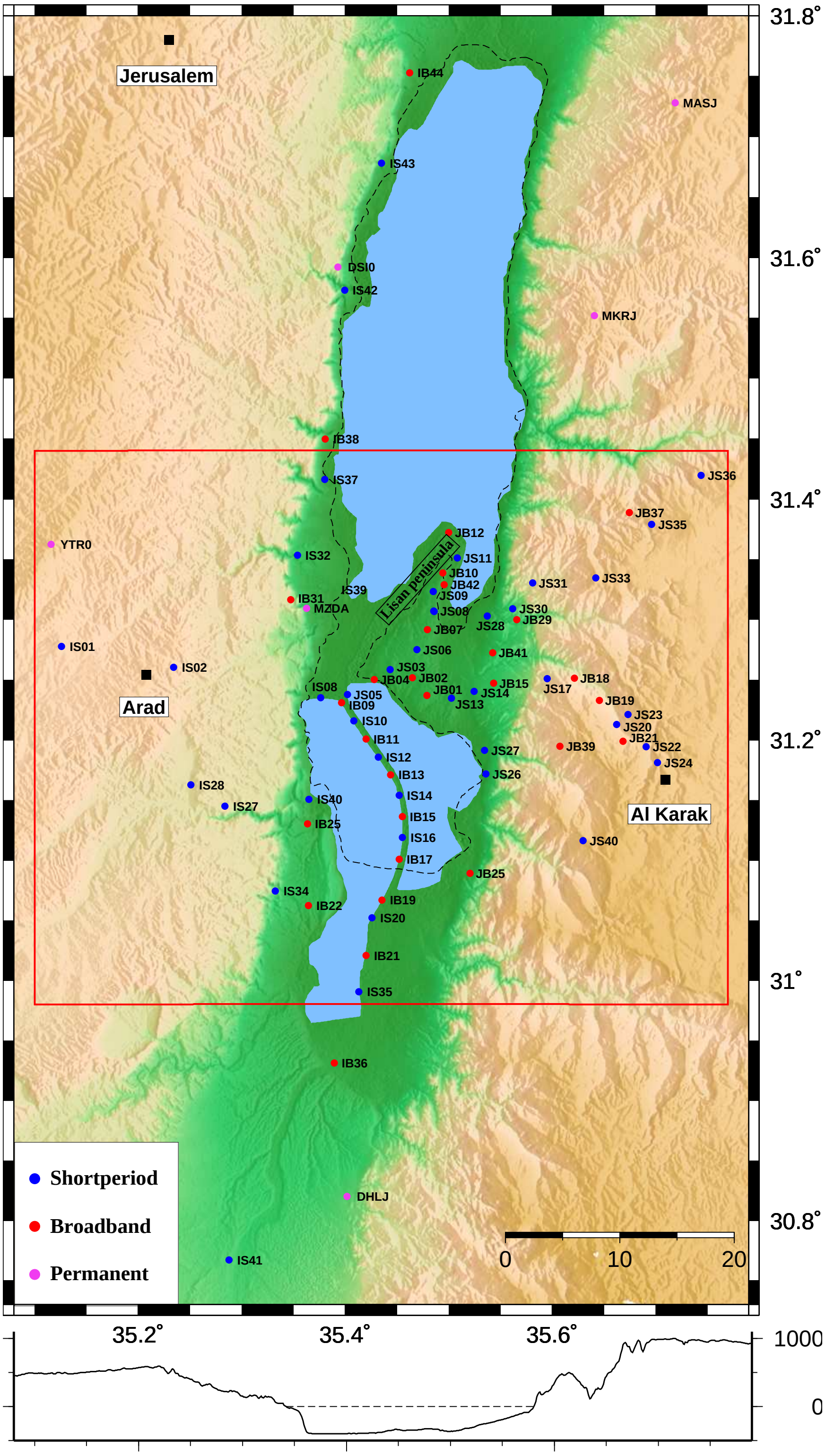
Jerusalem
IB44
MASJ
IS43
DSI0
IS42
MKRJ
IB38
IS37
JS36
JB37
JS35
JB12
YTR0
IS32
JS11
JB10
JB42
JS31
JS33
IS39
JS09
IB31
MZDA
Lisan peninsula
JS08
JS28
JS30
JB29
JB07
IS01
JS06
JB41
IS02
Arad
JS03
JB04
JB02
JB15
JS17
JB18
IS08
JS05
JB01
JS14
JS13
IB09
JB19
JS23
IS10
JS20
IB11
JB21
JB39
JS22
JS27
IS12
JS24
IB13
JS26
IS28
IS14
IS27
IS40
IB15
Al Karak
IB25
IS16
JS40
IB17
JB25
IS34
IB19
IB22
IS20
IB21
IS35
IB36
Shortperiod
Broadband
Permanent
DHLJ
IS41
0
10
20
31.8°
31.6°
31.4°
31.2°
31°
30.8°
35.2°
35.4°
35.6°
1000
0

The average spacing (distance to the first neighbor) was 2.5 km in Jordan and 4.5 km in Israel. In Jordan the stations in the basin were mostly located at or around the Lisan peninsula which is now the southern border of the Dead Sea (Figure 3.1). Farther south most of the stations are deployed on artificial dams of Dead Sea Works. Dead Sea Works (Israel) and the Arab Potash Company (Jordan) are harvesting minerals from the Dead Sea. The water of the Dead Sea is pumped into evaporation ponds where different minerals, mainly potassium chloride and potash, can be extracted (Figure 3.2). The evaporation ponds are delimited by large dams on which we deployed part of our stations (Figure 3.1). As the Dead Sea basin (DSB) is the deepest point on land the stations in the basin were located below 300 m mean sea level (Figure 3.2). At the shoulders of the basin the highest station was located at an elevation of 614 m (Israel - West) and 1096 m (Jordan - East), respectively. This network configuration made it appropriate to observe the local microearthquake activities as well as teleseismic events. About 1-2 local events per day were recorded.

All stations were equipped with Earth Data Loggers (EDL) as recording units. 38 of our stations were equipped with Mark L-4C-3D short period sensor, sampled at 200 Hz in high gain mode. The other 27 recorders were equipped with GURALP CMG-40T and CMG-3T, and with STS-2 seismometers, all sampled at 100 Hz. GPS (**G**lobal **P**ositioning **S**ervice) satellites provided accurate time stamps for the waveform data. Each station was equipped with a photovoltaic system including a battery (65 Ah), battery charger and one or two solar panels (50 W each) (Figure 3.2).

Figure 3.2: Images from the study area and the deployment of the stations. a) View over the DSB from western shoulder towards the East with the DS on the left and the evaporation ponds on the right. b) The view over the basin from mean sea level in the West. c) Evaporation pond with a dam on the right. d) Broadband station deployment in Jordan. e) Station on a dam in Israel with the EDL covered by plastic against the sun and a solar panel for electricity supply.

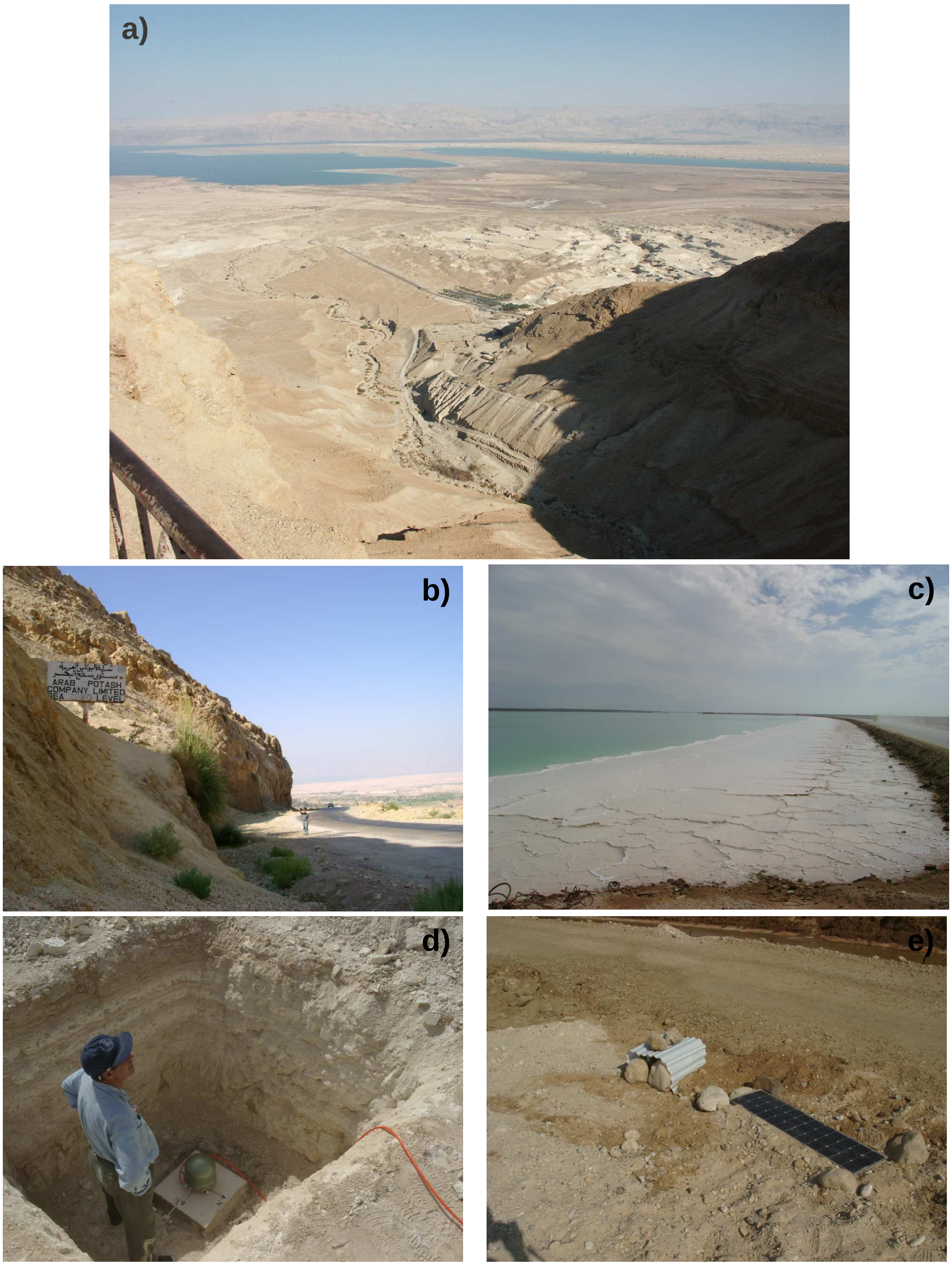
a)
b)
شركة البوتاس العربية
مستوى سطح البحر
ARAB POTASH
COMPANY LIMITED
SEA ZERO LEVEL
c)
d)
e)

Each station produced between 30 (broadband) and 100 (shortperiod) Mega bytes of compressed raw data per day, the total amount of collected station days amount to $\sim$ 26000 days. The total size of collected raw data was about two terra bytes (2000 GB). The stations were visited, checked and the data recovered in cycles of approximately four month. Most of the stations worked reliably. However, some broken cables caused interruption in the energy supply or the GPS connection. Unfortunately we encountered problems with vandalism and thefts in some locations in Israel so we lost some stations and had to dismantle all stations in unguarded areas. For the redeployment of these stations in June 2008 we had to enlarge the study area to the North and to the South (see Figure 3.1). Thus, some stations were running only half of the deployment time (see Appendix A). The red box in Figure 3.1 indicates the original deployment area where all following analysis will be focused on.

3.2 Data compilation

Event detection was done manually due to the expected large number of events with very low magnitude, e.g. with low signal to noise ratio. Half hour of data from all short period stations of the continuous data stream was inspected visually to find as many events as possible. Figure 3.3 shows the raw waveforms for all short period stations for 09/02/2007 23H00 - 24H00. Three detected events of different size are marked with red boxes.

The general data quality was good with significant differences between Israel and Jordan. The noise level was higher in Israel due to generally more human activity close to the station sites. Furthermore, in Israel the seismometers were buried at shallower depth (Israel $\sim$ 1 m, Jordan $\sim$ 2 m) and many station sites were placed on dams, e.g. not on natural soil (Figure 3.2). Thus, onsets for P- and S - waves were often superimposed with noise, e.g. the onset detection was less accurate or even sometimes impossible (Figure 3.4 and 3.5).

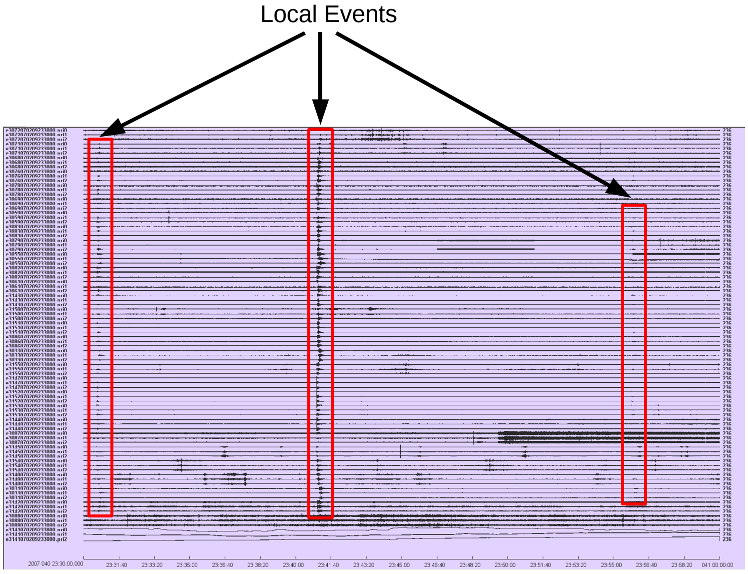

Figure 3.3: Example of waveforms from all working short period stations on 09/02/2007 23H30 - 24H00. Red boxes show three events of different magnitudes.

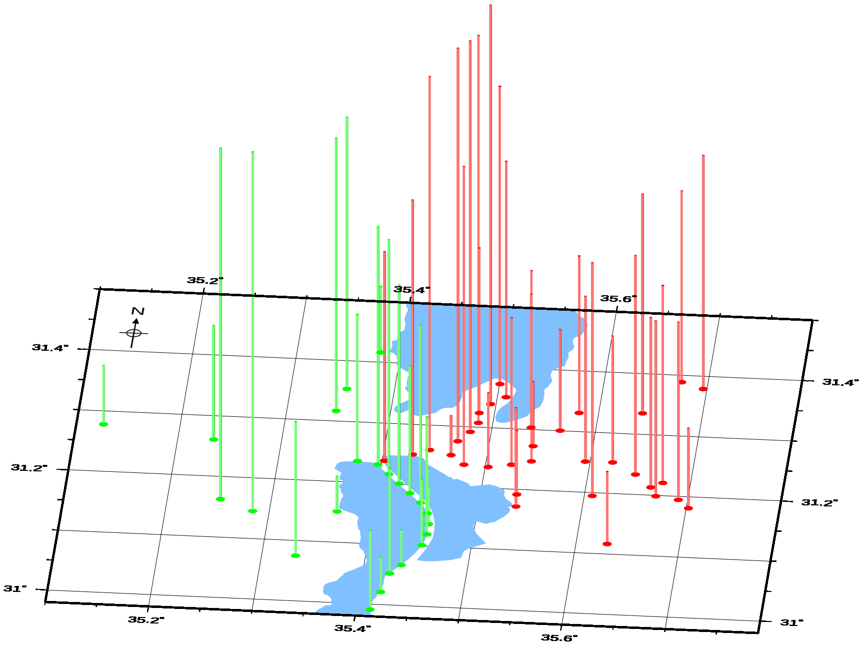

Figure 3.4: Relative amount of P- and S- picks per month for stations in Israel (green) and Jordan (red).

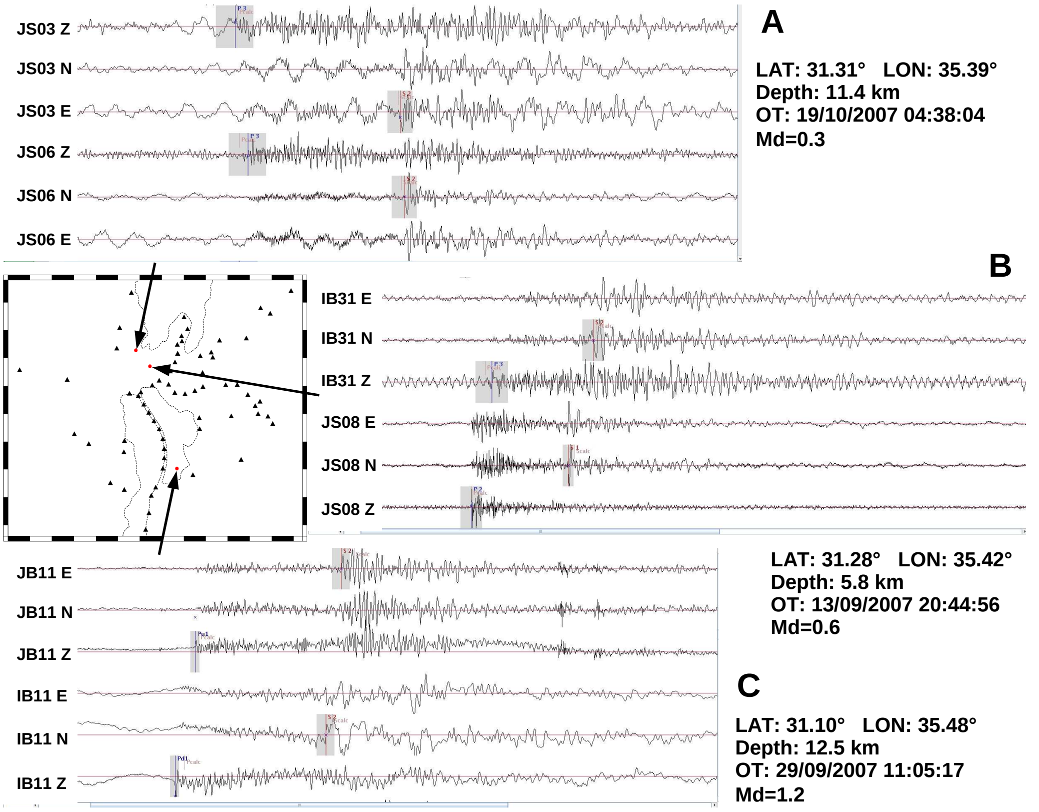

Figure 3.5: Three example recordings of events with different magnitudes. Even for small events (A: $M = 0.3$) waveform onsets were detectable. In (B) and (C) the difference of noise level between stations in Jordan (J***) and Israel (I***) is observable.

Determination of accurate arrival times and initial locations was done manually with the software JSTAR provided by the GII. The arrival time determination was done on unfiltered raw date, whenever possible. However, for the stations on the dams filtering was often necessary to detect waveform onsets. In total 655 local events were detected during the experiment and 29703 arrival times were determined.

Chapter 4

Theory and Methods

In this chapter the basic theory underlying the methods applied is presented. The inversion of travel time data is used in different manners here. A minimum 1-D velocity model (presented in Chapter 5), established following Kissling et al. [1994], is the basis of all further analysis. This 1-D model is used as the starting model for the inversion of a 3-D velocity model presented in Chapter 6. Furthermore, the double-difference procedure HypoDD [Waldhauser and Ellsworth, 2000], which is used to relocate a spatial cluster of earthquakes (see Chapter 7.2), is described.

4.1 Joint Inversion of the 1-D Velocity model

The arrival time of a seismic wave generated by an earthquake is a nonlinear function of the station coordinates (s), the hypocentral parameters (h), including origin time and geographic coordinates, and the velocity field (m) [Kissling et al., 1994]:

$$t_{obs} = f\left(s, h, m\right) \tag{4.1}$$

This equation is not solvable directly as all hypocentral parameters and the velocity field are unknown, while only the arrival times and the station coordinates are measurable quantities. Hence, using an a priori velocity model, rays are traced from a trial source location to the receivers and the theoretical arrival times (t_{calc}) are calculated. The residual travel time (t_{res}), the difference between observed and calculated arrival time, can be expanded as functions of differences (Δ) between estimated and true hypocentral and velocity parameters [Kissling et al., 1994]. To calculate suitable corrections to the hypocentral and model parameters, the dependence of the observed travel times on all parameters is crucial. For the velocity parameters and hypocentre locations this dependence is nonlinear, even in a 1-D model [Pavlis and Booker, 1983, Thurber, 1985]. A first-order Taylor series expansion to equation 4.1, written in matrix notation is [Kissling et al., 1994]:

$$\mathbf{t} = \mathbf{Hh} + \mathbf{Mm} = \mathbf{Ad} + \mathbf{e} \tag{4.2}$$

where:

$\mathbf{t}$	vector of travel time residuals (differences between observed and calculated travel time)
$\mathbf{H}$	matrix of partial derivatives of travel time with respect to hypocentral parameters
$\mathbf{h}$	vector of hypocentral parameter adjustments
$\mathbf{M}$	matrix of partial derivatives of travel times with respect to model parameters
$\mathbf{m}$	vector of velocity parameter adjustments
$\mathbf{e}$	vector of travel time errors, including contributions from errors in measuring the observed travel times, errors in the calculated travel times due to errors in station coordinates, use of the wrong velocity model and the hypocentral parameters, and errors caused by linear approximation
$\mathbf{A}$	matrix of all partial derivatives
$\mathbf{d}$	vector of hypocentral and model parameter adjustment

In standard earthquake localization the velocity parameters are kept fixed to a priori values and the observed travel times are minimized by perturbating hypocentral parameters. This neglecting of the coupling between hypocentral and velocity parameters can introduce systematic errors in the hypocentre location [Thurber, 1992, Eberhart-Phillips and Michael, 1993]. Furthermore, error estimates strongly depend on the assumed a priori velocity structure [Kissling et al., 1994]. In the concept of the minimum 1-D model hypocentre and velocity parameters are simultaneously inverted to achieve precise hypocentre locations and error estimates [Kissling, 1988]. The minimum 1-D velocity model obtained by this trial-and-error process represents the velocity model that minimizes the average of the RMS (Root-Means-Square error) values for all earthquakes [Kissling et al., 1995b]. Station corrections are used to account for lateral variations in the shallow subsurface but also the unresolvable part (3-D effects) of the model is absorbed by the station delays [Schurr, 2000].

4.2 The Coupled Hypocentre - Vel. Problem in 3-D

The arrival time T_{ij} for a source i to a seismic station j is expressed using ray theory as a path integral along the ray [Thurber, 1993]:

$$T_{ij} = \int_{source}^{station} u \, ds \tag{4.3}$$

where u is the slowness (reciprocal of velocity) and ds is an element of path length. For travel time inversions arrival times t_{ij} of seismic waves are the actual observations, where

$$t_{ij} = \tau_{ij} + T_{ij} \tag{4.4}$$

and τ_{ij} is the earthquake origin time [Thurber, 1993]. For a given set of arrival times t_{ij}^{obs}, the calculated arrival times t_{ij}^{cal} can be determined from equations 4.3 and 4.4 using trial hypocentres, origin times and an initial model of the seismic velocity structure [Lange, 2008]. The misfit between observed and calculated arrival times is the residuel r_{ij}:

$$r_{ij} = t_{ij}^{obs} - t_{ij}^{cal} \tag{4.5}$$

The residuals r_{ij} can then be related to perturbations of source and velocity parameters by a linear approximation as the residuals r_{ij} are not linearly dependent on the travel time. A Taylor approximation of first degree is applied around the start model (focal coordinates x_i^0, earthquake origin time τ_i^0 and initial velocity model m_0) and finite parametrization of the velocity structure [Thurber, 1983, Schurr, 2000]:

$$r_{ij} = \Delta\tau_i + \sum_{k=1}^{3} \frac{\delta T_{ij}}{\delta x_{i_k}} \Delta x_{i_k} + \sum_{l=1}^{L} \frac{\delta T_{ij}}{\delta m_l} \Delta m_l \tag{4.6}$$

with

$$\Delta\tau_i = \tau_i - \tau_i^0,\ \Delta x_i = x_i - x_i^0,\ \Delta m_l = m_l - m_l^0$$

$\Delta\tau_i$ and Δx_{i_k} are perturbations to the hypocentral parameters in time and space, m_l represents the L parameters of the velocity model. The velocity model partial derivatives $\delta T_{ij}/\delta m_l$ are essentially line integrals along the ray-path reflecting the relative influence of each model parameter on a given travel time datum [Thurber, 1993]. As the problem linearized in equation 4.6 is highly non-linear, a solution is usually derived in an iterative procedure.

The Poisson ratio μ is an important parameter to characterize rocks. It is related to the ratio between the P wave velocity v_P and the S wave velocity v_S through:

$$v_P/v_S = \sqrt{2\left(\frac{\mu}{1-2\mu} + 1\right)} \tag{4.7}$$

However, S arrival times are generally subject to greater uncertainties than P arrivals due to their arrival in the P coda, mode conversions, anisotropy and their inherently lower dominant frequency. This diminishes the resolution of S models which makes it difficult to compare it with P wave models. To overcome this problem, a 3-dimensional v_p model and a constant v_p/v_s ratio (based on Wadati diagram analysis) is used to construct an initial model to invert for v_p/v_s instead of inverting for a less consistent S velocity model.

The Derivation of v_p/v_s from S-P times as data is equivalent to the above treatment for P times, except for the forward problem stated in 4.3, which is now expressed as [Schurr, 2000]:

$$t_{ij}^{S-P} = \int_{source}^{station} \left[\frac{1}{v_s} - \frac{1}{v_p}\right] ds = \int_{source}^{station} \left[\frac{v_p}{v_s} - 1\right] \frac{1}{v_p} ds \tag{4.8}$$

4.2.1 The Inverse Problem

The hypocentre-velocity structure coupling in equation 4.6 can be rewritten in a more general notation [Menke, 1989]:

$$\mathbf{d} = \mathbf{G}\mathbf{m} \tag{4.9}$$

where **d** is the vector of the residual of the data, **m** is the model correction vector incorporating all $\Delta m,\ \Delta\tau,\ \Delta u.$ Matrix **G** contains the partial derivatives of travel times with respect to the model parameters. If **G** is square, e.g. number of unknowns and number of observations is equal, than a direct solution for equation 4.9 exists. As this is not often the case equation 4.9 is changed to [Menke, 1989]

$$\mathbf{m}^{\mathbf{est}} = \mathbf{G}^{-\mathbf{g}}\mathbf{d} \tag{4.10}$$

where $\mathbf{G}^{-\mathbf{g}}$ is called the generalized inverse. In seismic tomography there are normally more observations than unknowns, thus, the inverse problem is nominally overdetermined. For every observation a prediction error

$$e_i = d_i^{obs} - d_i^{pre} \qquad \text{for i=1,2,...,N} \tag{4.11}$$

is defined [Menke, 1989] as a measure of the misfit of the model. Thus, the aim is to minimize the prediction error $\mathbf{e} = \mathbf{d}^{\mathbf{obs}} - \mathbf{d}^{\mathrm{pre}}$ which leads to the **Least Squares Solution**

$$\mathbf{m}^{\mathrm{est}} = \left[\mathbf{G}^{\mathrm{T}}\mathbf{G}\right]^{-1}\mathbf{G}^{\mathrm{T}}\mathbf{d} \tag{4.12}$$

[Menke, 1989]. $\mathbf{G}^{\mathrm{T}}$ is the transpose of $\mathbf{G}$. $\mathbf{G}^{\mathrm{T}}\mathbf{G}$ is square and symmetric, so theoretically it is invertible and its eigenvalues are real [Lay and Wallace, 1995]. However, as the rays show an irregular distribution, model parameters can be overdetermined and underdetermined in the same problem, which makes it a mixed determined problem [Husen, 1999]. To avoid very small or zero eigenvalues for the underdetermined model parameters, damping is introduced to stabilize the numerical solution [Menke, 1989]. The solution of equation 4.12 is called the **Damped Least Squares Solution**:

$$\mathbf{m}^{\mathrm{est}} = \left[\mathbf{G}^{\mathrm{T}}\mathbf{G} + \epsilon^{\mathbf{2}}\mathbf{I}\right]^{-1}\mathbf{G}^{\mathrm{T}}\mathbf{d} \tag{4.13}$$

where ϵ^2 is a damping parameter and $\mathbf{I}$ is the identity matrix. ϵ^2 can be seen as taring between prediction error and solution length. *Damped least-squares* means that the norm of the model perturbations (complexity of the model) is weighted and combined with the squared data misfit - the combination is minimized at each iteration [Evans et al., 1994]. The damped least-squares solution is applied in the programs `SIMULPS`, `HypoDD` and also `VELEST`, which are used for the travel time inversion of this study.

In `SIMULPS` the velocity model is represented by velocity values specified on a three-dimensional grid of nodes. The spacing between any pair of adjacent planes can be chosen arbitrarily [Evans et al., 1994]. The velocity for a given point ($x = (x_1, x_2, x_3)$) inside the grid is calculated by linearly interpolating the eight neighboring grid nodes $(p_{1,1}, p_{1,2}, p_{1,3})$, $(p_{1,1}, p_{1,2}, p_{2,3})$, ..., $(p_{2,1}, p_{2,2}, p_{2,3})$ [Thurber, 1983]:

$$v(x_1, x_2, x_3) = \sum_{i_1=1}^{2}\sum_{i_2=1}^{2}\sum_{i_3=1}^{2} v(p_{i_1,1}, p_{i_2,2}, p_{i_3,3}) \cdot \prod_{j=1}^{3}\left(1 - \left|\frac{x_j - p_{i_j,j}}{p_{2,j} - p_{1,j}}\right|\right) \tag{4.14}$$

4.2.2 Resolution and Covariance

The quantification of the resolution and the error estimation of the derived solution is a crucial part of all seismic inversion techniques. The model resolution matrix $\mathbf{R}$ defines, how well the estimated solution, $\mathbf{m}^{\mathrm{est}}$ (4.10) resolves the true solution $\mathbf{m}^{\mathrm{true}}$(for which $\mathbf{Gm}^{true} = \mathbf{d}$ holds). *True* means in this case *true* within the model parametrization and not true, 'real earth'. Following Menke [1989] the model resolution matrix is defined as:

$$\mathbf{m}^{\mathrm{est}} = \mathbf{G}^{\text{-g}}\mathbf{d}^{\mathrm{obs}} = \mathbf{G}^{\text{-g}}\left[\mathbf{Gm}^{\mathrm{true}}\right] = \left[\mathbf{G}^{\text{-g}}\mathbf{G}\right]\mathbf{m}^{\mathrm{true}} = \mathbf{Rm}^{\mathrm{true}} \tag{4.15}$$

$\mathbf{R}$ is a $M \times M$ matrix and M the number of model parameters. Each row of $\mathbf{R}$ is an averaging vector describing the influence of other parameters on a single resolved parameter. The *spread function* [Menke, 1989] of each vector is a measure of how localized the velocity averaging is that yielded the grid point velocity, i.e. how well each parameter is resolved and how much smearing into adjacent nodes is present [Toomey and Foulger, 1989]. Therefore this function is an indicator of the scale of feature resolved and is defined as:

$$S_p\left(\mathbf{r}_p\right) = \mid \mathbf{r}_p \mid^{-1} \sum_{q=1}^{M} w(p,q) R_{pq}^2 \tag{4.16}$$

where $\mathbf{r}_p$ is the *averaging vector* of the pth parameter (i.e. the pth row of the resolution matrix), $w(p,q)$ is a weighting function defined as the distance between pth and qth grid points, R_{pq} is an element of the resolution matrix, and m is the number of parameters. A small *spread value* indicates a well resolved model parameter while high values are representing broad shapes of averaging vectors.

The model covariance specify how data errors are mapped into model space [Menke, 1989]:

$$\mathbf{C}^m = \sigma_d^2 \mathbf{G}^{-g}(\mathbf{G}^{-g})^T \tag{4.17}$$

where $\mathbf{C}^d = \mathbf{I}\sigma_d^2$ is assumed, that is, data errors are independent and have a common variance σ_d^2 [Schurr, 2000]. The diagonal elements of $\mathbf{C}^m$ are the standard errors of the model, and the off-diagonal elements depict error correlation of the model parameters. It is important to note that the standard error is limited as it often underestimates the true error [Schurr, 2000].

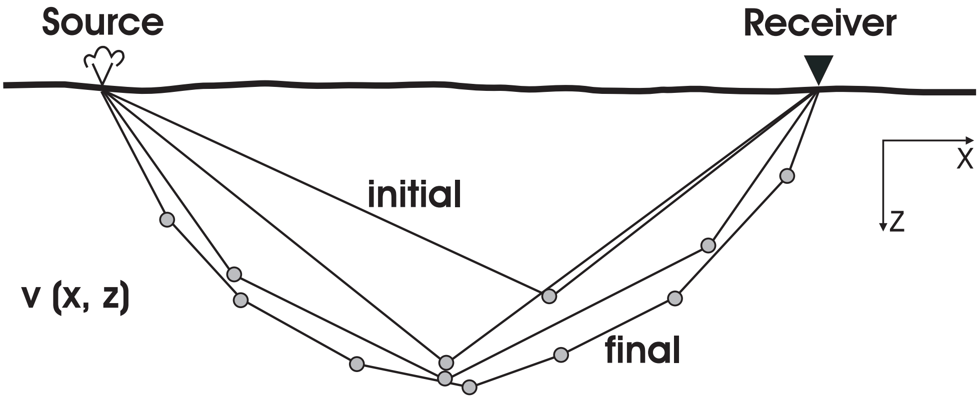

Figure 4.1: Schematic diagram of the pseudo-bending method of Um and Thurber [1987] from Rawlinson and Sambridge [2003]. For explanation see text.

4.2.3 Ray tracing

The determination of the propagation path of the seismic wave between each source and receiver, including the wave travel time along that path, is another important part of a local earthquake tomography (LET) procedure. The travel time is needed in order to calculate the arrival time residual, and the ray path is needed for the computation of the hypocentre and velocity partial derivatives. To increase the computational speed of the calculation, approximate ray tracing (ART) techniques are applied in LET. In `SIMULPS, the` pseudo bending approximate ray tracing (ART-PB) method is applied, developed by Um and Thurber [1987], here described following Rawlinson and Sambridge [2003]. The bending method operates by adjusting the geometry of an initial path that joins the source and the receiver (Figure 4.1).

In the first step of the pseudo bending method, the model between source and receiver is scanned by a large number of circular arcs of different curvature and dip angles, and the fastest one is selected as the approximate ray following Fermat's principle [Thurber, 1983]. This initial guess path is defined by three points which are linearly interpolated (Figure 4.1). The centre point is then iteratively perturbed using a geometric approximation of the ray equation until the extremum of the travel time converges within a specific limit, at which point the ray equation will be approximately satisfied. In the next step the number of path segments is doubled and the perturbation scheme is repeated working from both endpoints to the center. This procedure is repeated iteratively by doubling the number of segments at each step until the change in travel-time between successive iterations reach a certain value defined as convergence criterion. Um and Thurber [1987] showed that the pseudo-bending technique is much faster compared to earlier bending methods.

4.3 Double-Difference Algorithm

The description of the Double-Difference algorithm HypoDD is fully presented by [Waldhauser and Ellsworth, 2000] and only an overview will be given here.

The accuracy of absolute hypocentre solutions is controlled by several factors, including the network geometry, available phases, arrival-time reading accuracy, and knowledge of the crustal structure [Pavlis, 1986, Gomberg et al., 1990]. Especially, limited knowledge about the velocity structure influences the location accuracy. The effect of errors in structure can be effectively minimized by using relative earthquake location methods (e.g. Poupinet et al., 1984, Fremont and Malone, 1987). If the hypocentral separation between two earthquakes is small compared to the event-station distance and the scale length of the velocity heterogeneity, then the ray path between the source region and a common station is similar along almost the entire ray path. In this case, the difference in travel times for two events observed at one station can be assigned to the spatial offset between the events with high accuracy. This is true, because the absolute errors are of common origin, except in the small region where the ray path differ close to the sources. The relative arrival-time readings can be furthermore improved by using waveform cross-correlation methods. Similar waveforms are produced at a common station from two different earthquakes if their source mechanisms are virtually identical and their sources are co-located so that the signal scattering due to velocity heterogeneities along the ray path is small. The two events i and j in Figure 4.2 are located close together (as e.g. two events in a cluster).

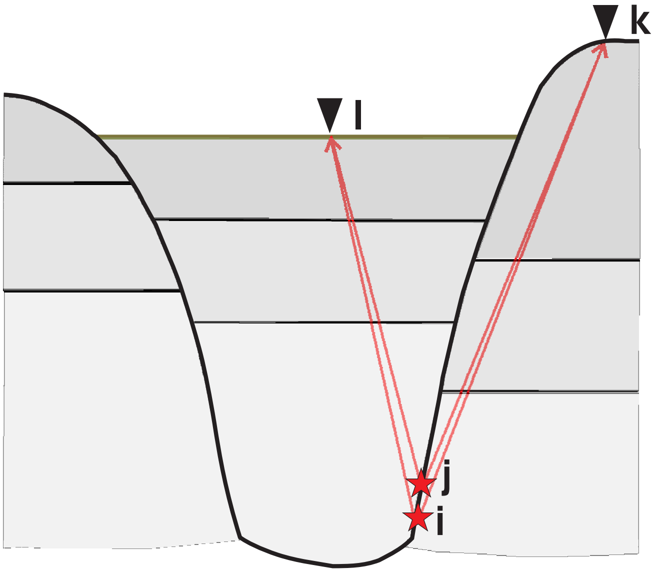

Figure 4.2: Schematic diagram to illustrate the double-difference algorithm. Two very close events i and j in a cluster are registered at two stations l and k situated above different geological units. For explanation see text.

The rays from these two events to station k are taking almost the same path. Thus, the differences in arrival times are directly linked to the differences in the hypocentre location. Equation 4.5 is therefore changed to:

$$dr_k^{ij} = (t_k^i - t_k^j)^{obs} - (t_k^i - t_k^j)^{cal} \tag{4.18}$$

Equation 4.18 is defined as the **double-difference**. Measured arrival times can be used in equation 4.18, where the observables are absolute travel times t, or cross-correlation relative travel-time differences. Like equation 4.5, equation 4.18 can also be brought to the form of a system of linear equations:

$$\mathbf{WGm} = \mathbf{Wd} \tag{4.19}$$

where **G** defines a matrix of size M x 4N (M, number of double-difference observations; N, number of events) containing partial derivatives, **d** is the data vector containing the double-differences (4.18), **m** is a vector of length 4N, $[\Delta x, \Delta y, \Delta z, \Delta T]^T$, containing the changes in hypocentral parameters that need to be determined, and **W** is a diagonal matrix to weight each equation.

For a small amount of data and for well-conditioned systems, equation 4.19 can be solved by the method of singular value decomposition (SVD):

$$\hat{\mathbf{m}} = \mathbf{V}\boldsymbol{\Lambda}^{-\mathbf{1}}\mathbf{U}^{\mathbf{T}}d \tag{4.20}$$

where **U** and **V** are two matrices of orthonormal singular vectors of the weighted matrix **G**, and $\boldsymbol{\Lambda}$ is a diagonal matrix of the singular values of **G**. SVD is used to investigate the behavior of small systems, as the matrices **U**, Λ and **V** in equation 4.20 store information on the resolvability of the unknown parameter **m** and the amount of information (or lack thereof) supplied by the data **d**. The least squares errors, e_i, are estimated for each model parameter i by

$$e_i^2 = C_{ii} \cdot var, \tag{4.21}$$

where C_{ii} are the diagonal elements of the covariance matrix $\mathbf{C} = \mathbf{V}\boldsymbol{\Lambda}^{-\mathbf{2}}\mathbf{V}^{\mathbf{T}}$, and var is the variance of the weighted residuals calculated by

$$var = \frac{\sum_{i_1=1}^{M}(d_i - \overline{d})^2 - \frac{(\sum_{i=1}^{M} d - \overline{d})^2}{M}}{M - (4N)}, \tag{4.22}$$

$\overline{d}$ being the mean of the residual vector and d_i the residual of the ith observation. As the system becomes larger, SVD is inefficient and the solution is found by using the conjugate gradient algorithm LSQR of Paige and Saunders [1982].

Chapter 5

Inversion for a 1D - Velocity Model

Hypocentre determination of local earthquakes is highly dependent on the velocity model used for the localization. Furthermore, an appropriate initial model is essential for LET [Kissling et al., 1994]. Hence, arrival time data were used for a joint inversion of 1-D velocity structure, station delays and hypocentral coordinates with the `VELEST` software [Kissling et al., 1994, 1995a]. The velocity model is parametrized by horizontal layers with constant velocity. The inversion of hypocentral parameters and velocities is done separately and iteratively. The search for a minimum 1-D model starts with a trial-and-error process using a wide range of realistic and possibly unrealistic velocity models to define the entire range of possible mathematical solutions. To delimit the influence of three dimensional velocity changes, station corrections relative to the velocity of the top layer and a reference station are included in the concept of minimum 1-D model. A good reference station should not lie at the edges of the network and should have a large number of readings with preferably high observation weights. Station IB31 achieves these criterias (see Appendix A) and was therefore defined as reference station.

The calculation of a minimum 1-D model requires a set of well locatable events. The hypocentre-velocity coupling would cause instabilities in the inversion process in case of large uncertainties in hypocentre locations. The largest azimuthal gap of observations (GAP) and the minimum number of observation per event are prime selection criteria to ensure good locatability [Husen et al., 1999]. With the condition of a GAP $\leq 180°$ all events are compromising 12 onset times, containing at least 6 S wave observations. This reduced the number to 530 well constrained events with 13,970 P- and 12,760 S-wave travel time observations. A Wadati-diagram delivered a starting value for the v_P/v_S ratio of 1.74 (see Figure 5.1).

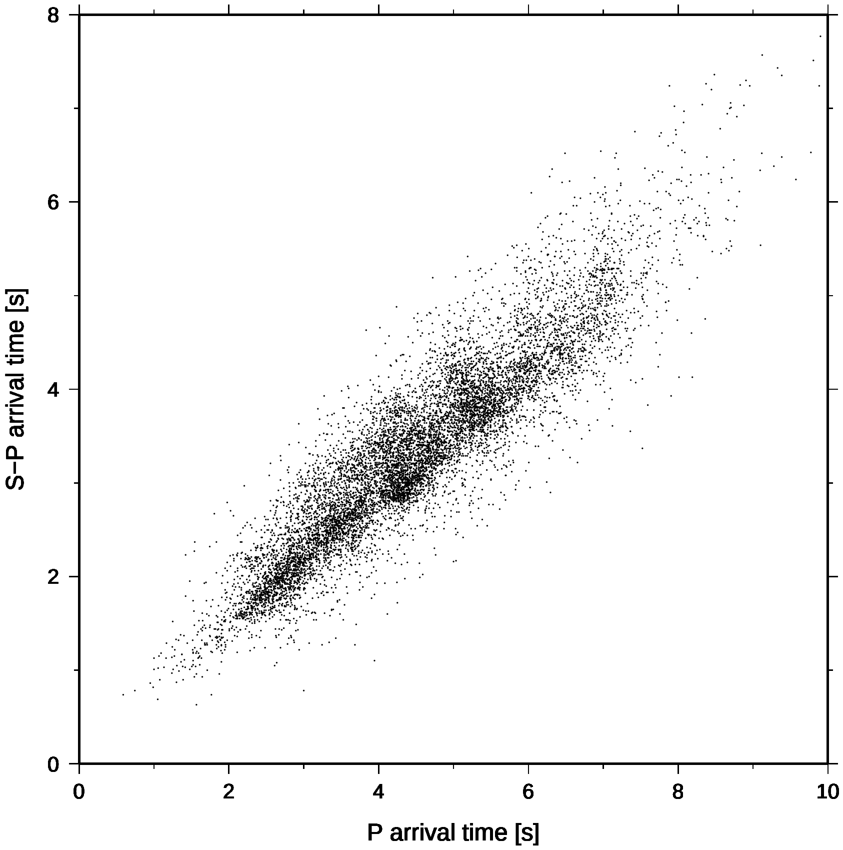

Figure 5.1: Wadati Diagram of events selected for the P- and S-wave inversion. Picks lying far off the main trend were eliminated. The estimated v_P/v_S ratio is 1.74.

A wide range of initial velocity models (indicated in Figure 5.2) was used to investigate the quality and stability of the final velocity models. The dense station distribution and the good quality of the S-wave picks allowed to invert for the P- and the S-velocity model independently. The final 1-D models consist of 8 layers down to a depth of 30 km. A first-arrival tomography of a controlled source seismic experiment [Paschke et al., 2010] crossing the study area from West to East showed clearly that the uppermost 2 km are laterally very inhomogeneous, e.g. the P-wave velocity at 1 km depth is varying between 3.5 and 5 km/s. This explains the varying velocity values (for different start models) for the top layer.

depth [km]	v_P $[km/s]$	v_S $[km/s]$	v_P/v_S
-1.5- 0.5	3.81	1.21	3.15
0.5- 2.5	3.98	2.31	1.72
2.5- 4.5	4.33	2.48	1.75
4.5- 6.5	4.39	2.60	1.69
6.5- 8.5	5.02	2.65	1.89
8.5-10.5	5.36	3.16	1.69
10.5-20.5	5.36	3.23	1.66
20.5-30.5	5.36	3.33	1.61

Table 5.1: The minimum 1-D velocity model

A P-wave velocity of 3.8 km/s is calculated for the top layer (see Figure 5.2 and Table 5.1). The velocity increases to 5.36 km/s at 8 km depth. This velocity remains constant until a depth of 30 km, where Mechie et al. [2009] estimated the Moho. However, the velocity layers below 20 km depth are poorly resolved because of the reduced seismicity at greater depth.

The S-wave velocity is very low (1.2 km/s - lower than all the tested start models, see Figure 5.2) in the uppermost layer due to weathered and partly water-saturated rocks near the surface in the basin. Therefore, the v_P/v_S value is high, about 3.2. In the next layer the S-wave velocity is 2.3 km/s and increases slowly to 3.16 km/s at 8 km depth. At 30 km depth a velocity of 3.3 km/s is reached. The v_P/v_S ratio shows small variations between 1.61 and 1.89 from the second layer downwards having an average value of 1.71.

Inverted station delays are in the range of -1.61 and +0.51 sec for P and in the range of -3.03 and +1.28 for S (Figure 5.3, Appendix B). In general, one can see larger values of station corrections (related to low velocities) in the basin and smaller values (high velocities) on the shoulders of the basin.

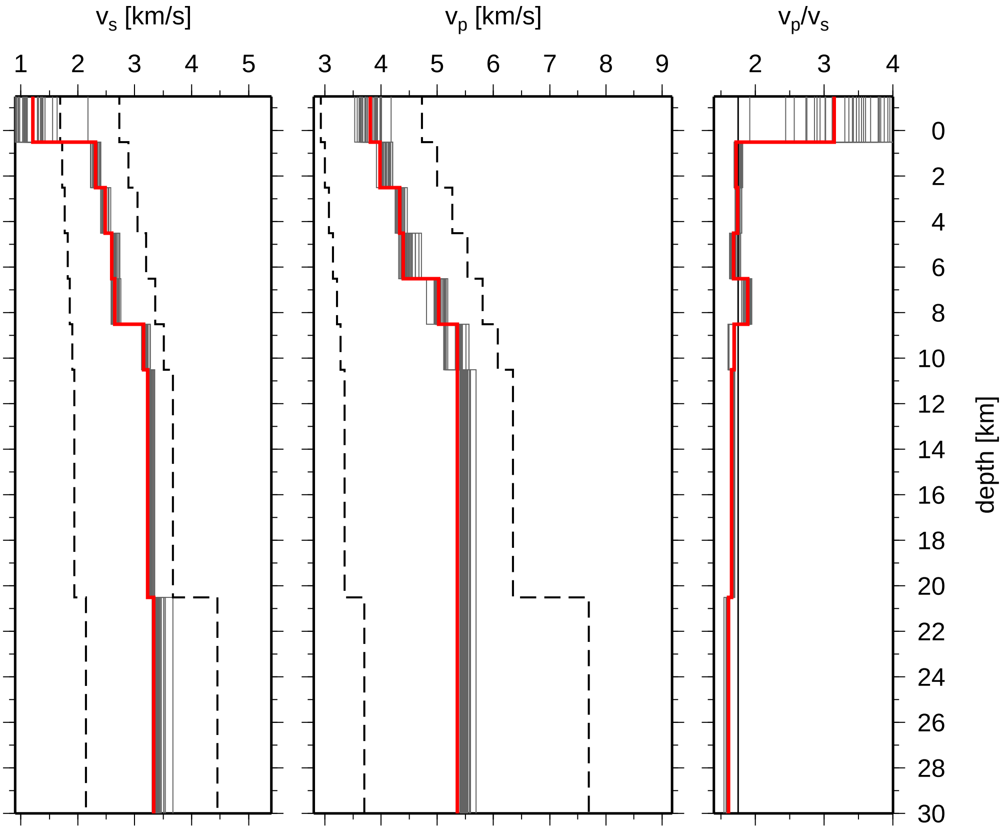

Figure 5.2: Resulting minimum 1-D velocity models for P-waves, S-waves and the v_P/v_S ratio versus depth are depicted. Best model (= lowest RMS) plotted in red, all other resulting models are plotted in grey. The range of input models for P and S velocity is marked with the dashed lines.

Furthermore, the corrections on the eastern shoulder are smaller than on the western shoulder. The distribution of seismicity is discussed in Section 7.1. The properties of the datatset with all events relocated with the minimum 1-D model is shown in Figure 5.4. Figure 5.5 displays the final residual histograms for each observation weight and both wavetypes P and S. The residual distribution follow Gaussian distribution. Picks with extremely high residuals were checked.

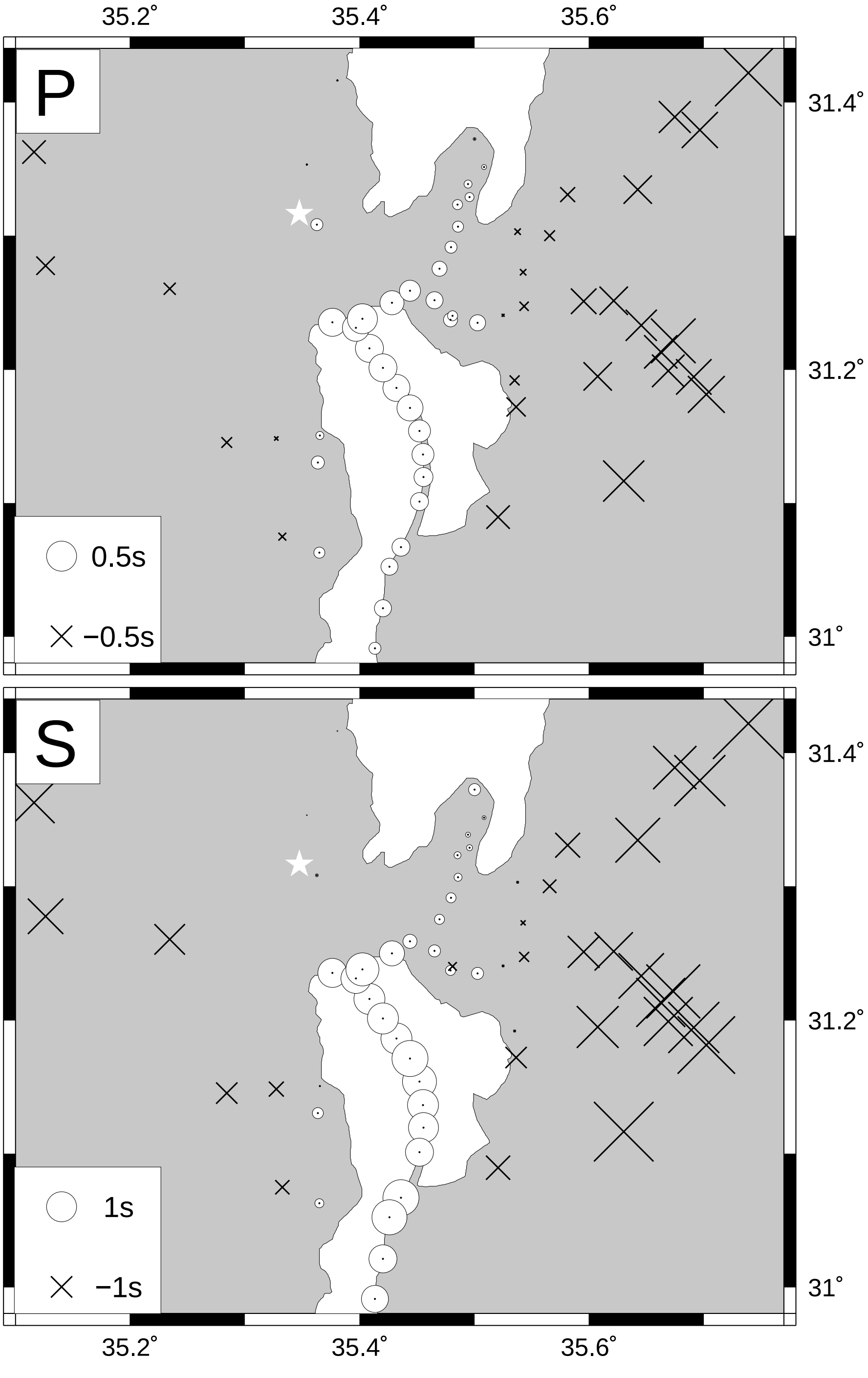

Figure 5.3: Station correction for P-wave (top) and S-wave (bottom) onsets. The reference station is marked with a star.

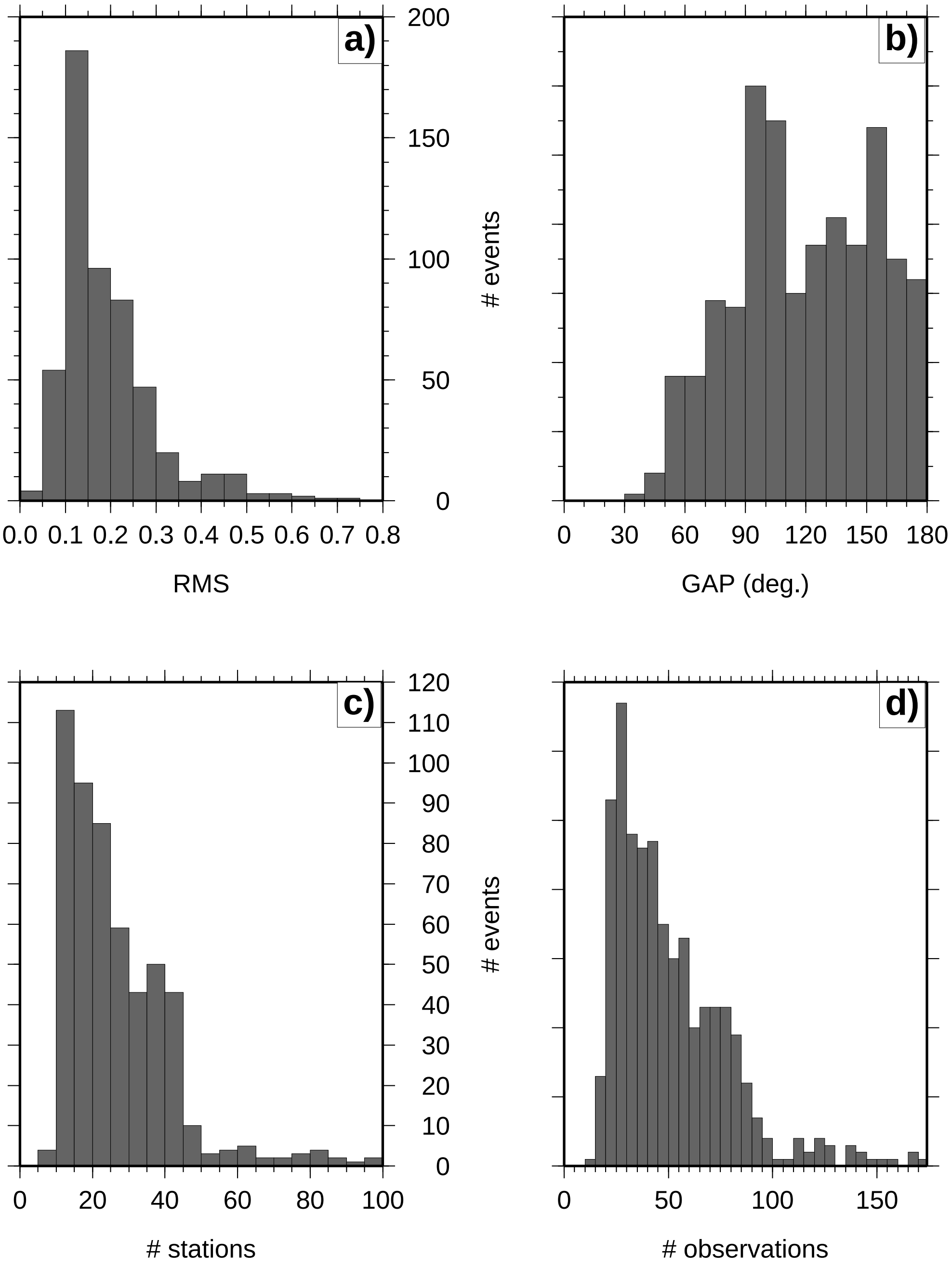

Figure 5.4: Histograms of distribution of RMS (a), GAP (b), amount of observing stations (c) and number of observations (d) over all events for the hypocentres located with the minimum 1-D model.

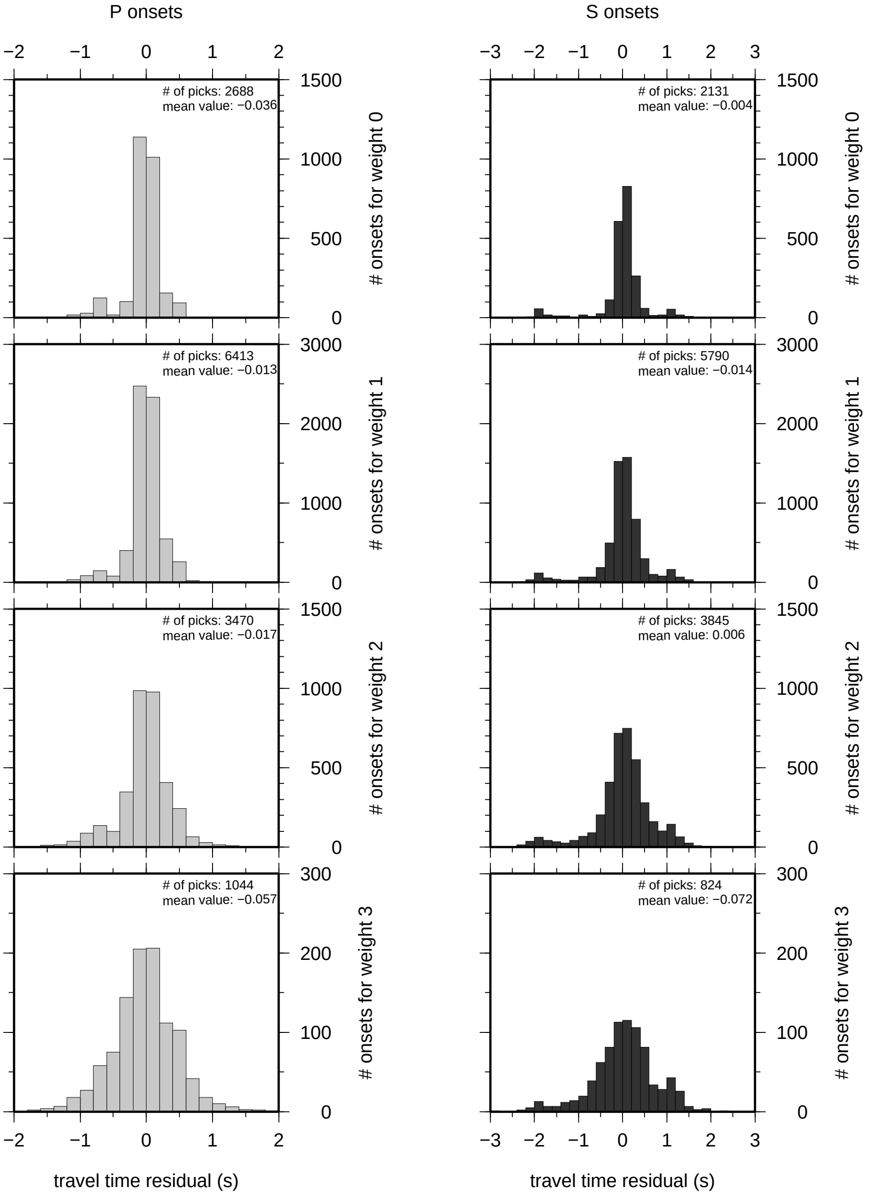

Figure 5.5: P-wave (left column) and S-wave (right column) residuals for each observation weight for all events selected for the 1-D Inversion.

Quality and stability tests are crucial to verify the conclusions of inversions. Shifting hypocentres randomly in one direction by 2-3 km before introducing them in the joint velocity hypocentre inversion, provides a check for a bias in the hypocentre locations and for the stability of the solution of the coupled problem [Kissling et al., 1994, Husen et al., 1999]. If the proposed minimum 1-D velocity model denotes a robust minimum in the solution space, no significant changes in velocity and hypocentre locations are expected. The dislocations in focal depth, latitude and longitude are plotted in Figure 5.6 after shifting the original hypocentres 2-3 km randomly and introducing them in the inversion. All events generally relocate close to their original position, proving that the hypocentre locations obtained by the inversion process are not systematically biased. The dislocations of the hypocentres plotted in Figure 5.6 are yielding standard derivation of about 100 m for the longitude shift, about 200 m for the latitude shift and about 300 m for the depth shift.

Furthermore, the accuracy of the obtained hypocentres can be verified with a jackknife test (Figure 5.7), i.e. subsets of different amounts of observations for certain events are selected randomly and relocated with the final velocity model (e.g. Lange [2008]). For relocations with 26 stations, which is the average amount of stations at all events, we obtain a location variance of about 1 km (Figure 5.7). This is assumed to be representative for the location accuracy and is confirmed by a similarly small misfit of the relocalization of an artificial explosion in the area.

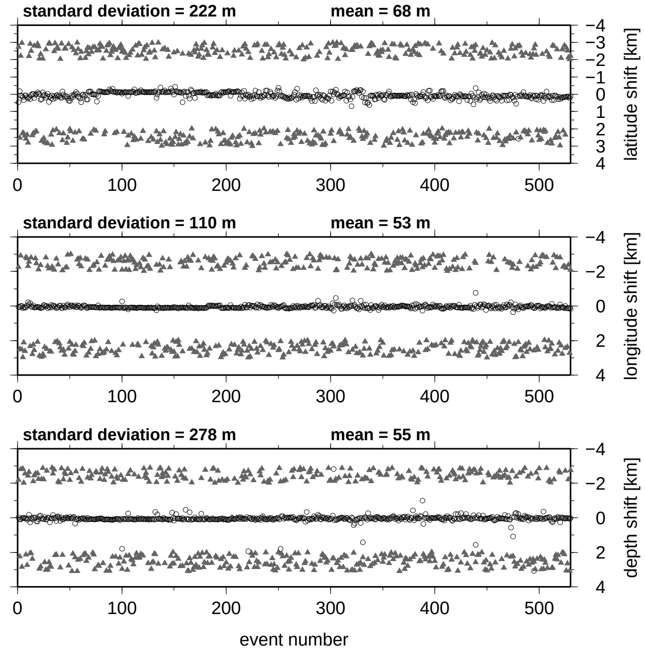

Figure 5.6: Shift in hypocentre locations (circles) after test with random shifted hypocentres. The triangles denote the original shift of the hypocentre before introducing them in the 1-D inversion. The resulting average shift and variance after the inversion is shown on top of each graphic.

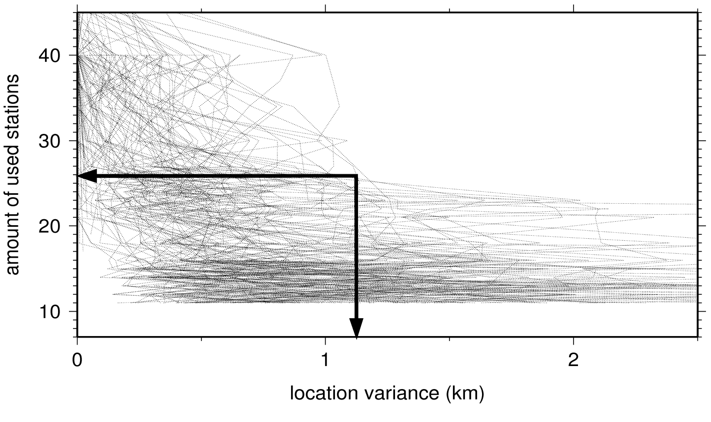

Figure 5.7: Subsets of observations for certain events randomly selected and relocated to estimate location accuracy (jackknife test). Location variance is plotted against the number of stations used. The arrows are indicating the location variance (about 1 km) for the average number of stations (26) which is assumed to be representative for the average hypocentre accuracy.

Chapter 6

Tomography

Various authors described the importance of a careful selection of the initial model for local earthquake tomography studies [Kissling, 1988, Eberhart-Phillips, 1990, Kissling et al., 1994]. The inversion to obtain a minimum 1-D model [Kissling et al., 1994] for P- and S-waves described in Chapter 5 was calculated in order to obtain an initial 1-D model for the tomography. The average of the 3-D velocities in each layer (weighted by the total ray length) is represented by the 1-D model, which is not biased by a priori input other than the choice of the layer depth and thickness [Schurr, 2000]. The same selection criteria for the tomography were used as in the 1-D inversion (GAP$\leq$ 180°; at least 12 onset picks) as a change (e.g. increase of the GAP to 200°) would not increase the number of events. The number of observations and unknown variables for the inversion is shown in Table 6.1.

knowns			unknowns			
P-obs	S-obs	total	model $x * y * z$ for v_P and v_P/v_S	hypo centres	origin times	total
			$16 * 16 * 9 * 2$	$3 * 530$		
13970	12760	26730	4608	1590	530	6728

Table 6.1: Number of observations and variables of the 3-D inversion

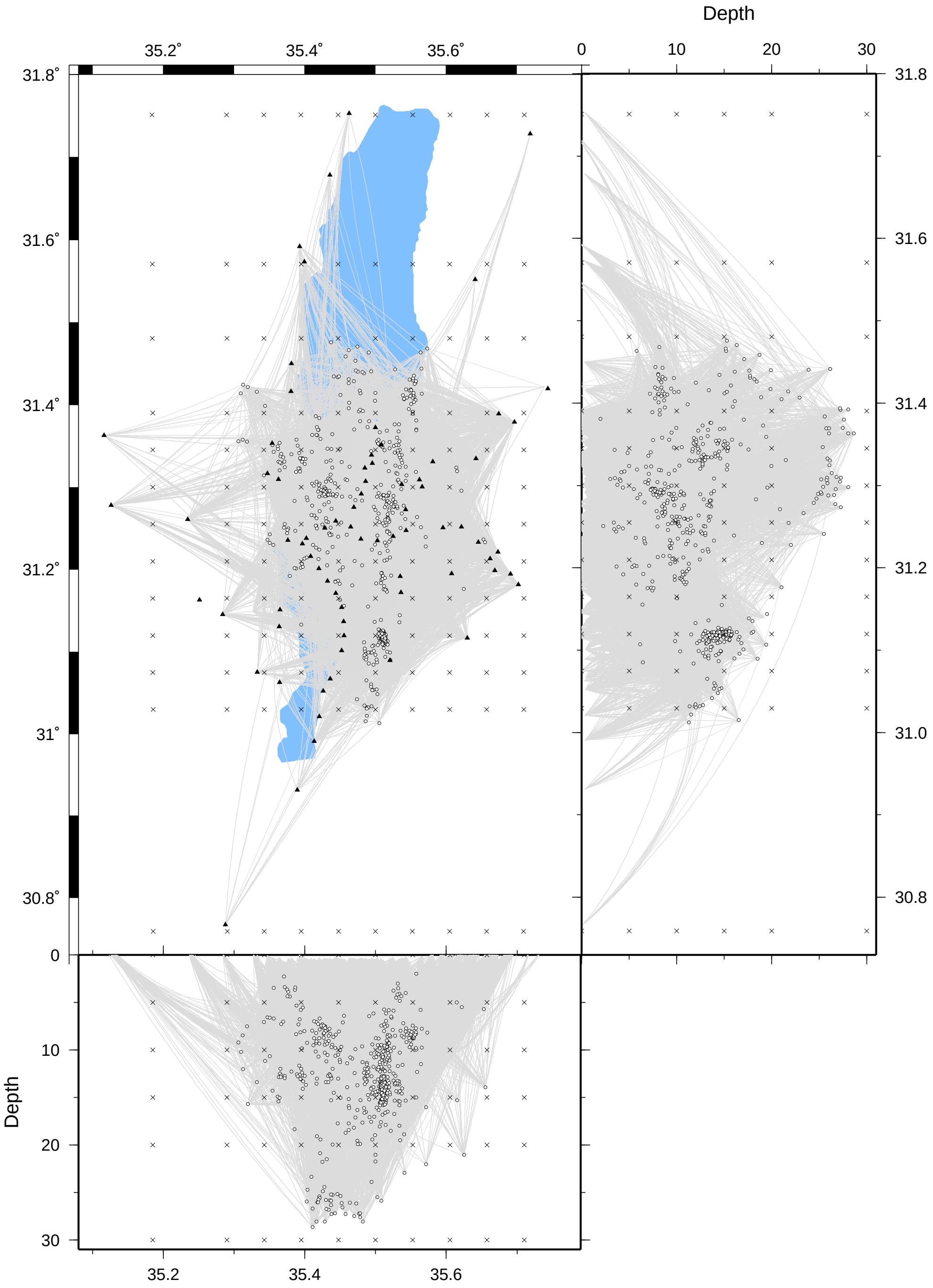

Figure 6.1: Ray path of the 3-D `SIMULPS` inversion, indicated in grey. Final locations are plotted as white circles and the stations are marked with black triangles. The distance between the nodes of the inversion, indicated by crosses, range from 20 km at the edges of the model to 2.5 km in the centre.

The parametrization in `SIMULPS` should be based on the distribution of the events and stations and the ray coverage, respectively. In Figure 6.1 the ray coverage is shown together with the distribution of the events and the stations. The ray coverage was very good around the eastern boundary fault where most of the events occurred, station density was high and noise level was low. The western faults (WF) are covered by many rays despite the lower density of stations and events. Two model parametrizations were used to adopt the distances between the model nodes to the heterogeneous earthquake and station distribution: a coarse grid spacing of 10 × 10 km for the outer areas and a fine parametrization of 5 × 5 km for the area of dense station and earthquake distribution (Figure 6.1).

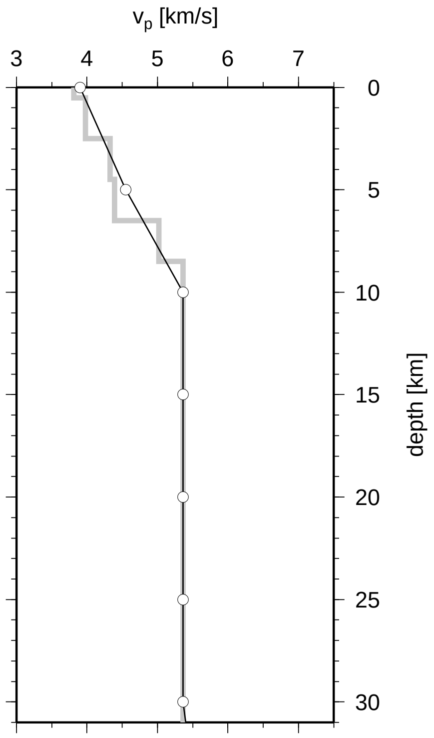

Figure 6.2: Minimum 1-D v_P model (grey line) and the corresponding starting model (black line) for the tomography with the parametrization points as white dots. In between the velocity has been linearly interpolated.

One node 30 km away to the north and one to the south, were added to account for some stations farther away. Vertical node spacing of 5 km was used until 20 km depth where the seismic activity decrease rapidly, followed by a node at 30 km depth (Figure 6.2). For technical reasons one additional node is introduced at large distances (depth: 100 km; NS/EW: 750 km) following Evans et al. [1994]. The density of the network and the amount of local events allowed for a 3-D inversion of the data. Three different approaches were chosen:

- A gradual approach, following Haberland et al. [2009], with an initial coarse 2-D inversion. The inversion for the following fine 2-D inversion uses the velocities of the coarse inversion as initial velocities. The last step is a fine 3-D inversion (a).
- Another gradual approach, following Husen et al. [2000], also starting with a coarse 2-D inversion, performs then a coarse 3-D inversion and a fine 3-D inversion (b).
- The third approach includes a direct coarse 3-D inversion followed by a fine 3-D inversion ((c) in Table 6.2).

The gradual approaches (a) and (b) is based on the assumption in areas of low resolution, the true structure is better recovered by using a 2-D model as initial model than by using an initial 1-D model [Eberhart-Phillips et al., 1995, Husen, 1999].

All three different approaches a, b, c, show comparable values P data variance reduction (∼84 %) and S data variance reduction (∼78 %) (Table 6.2). Thus, results of all three approaches are presented and compared as they all fit the data equally well. For the direct 3-D inversion the model parameters in regions with low ray coverage are poorly resolved and thus remain close to the initial model. For the gradual approach the model perturbations in areas of low ray coverage represents mainly those of the 2-D inversion [Husen, 1999]. The use of the gradual approach ensures that the velocity values of poorly resolved nodes will not be allowed to deviate significantly from the initial model, therefore avoiding complicated artifacts in the 3-D inversion [Haberland et al., 2009]. The goal of the 2-D inversion was furthermore to establish a regional model which reflects the dominant structural elements

(a)	Spacing [km]	P data var.	%	S data var.	%
start		0.204	100	0.354	100
2D coarse	5	0.036	18	0.083	23
2D fine	4	0.036	18	0.083	23
3D fine	4	0.033	16	0.078	22
(b)	Spacing [km]	P data var.	%	S data var.	%
start		0.204	100	0.354	100
2D coarse	5	0.036	18	0.083	23
3D coarse	5	0.033	16	0.080	23
3D fine	4	0.033	16	0.078	22
(c)	Spacing [km]	P data var.	%	S data var.	%
start		0.204	100	0.354	100
3D coarse	5	0.034	16	0.078	22
3D fine	4	0.034	16	0.078	22

Table 6.2: Data variance for P and S waves of the three different approaches: 2-D coarse, 2-D fine, 3-D fine (a); 2-D coarse, 3-D coarse, 3-D fine (b); 3-D coarse, 3-D fine (c).

in the area, i.e. the sedimentary basin in the centre characterized by lower velocities and the two shoulders east and west of it with presumably higher velocities. The small reduction increase from the 2-D to the 3-D inversion in the gradual approach (1-2 %) supports the assumption of a primarily two dimensional structure of the volume under investigation (Table 6.2).

The damping value (ε^2 in equation 4.13) is a critical parameter in LET. The damping determines the trade-off between model variance and the data variance. Low damping values will lead to high model perturbations with large reduction in data variance, whereas high damping values yield low model perturbations and small data variance reduction. The appropriate damping value was selected empirically from a series of one-step inversions with different damping values [Eberhart-Phillips, 1986]. The model variance values for the different inversions are plotted as a function of the data variance values to determine the ”trade-off” curve (Figure 6.3). The preferred damping values are chosen in order to achieve the best compromise between data misfit reduction and model variance. Figure 6.3 shows as an example trade-off curves for the direct 3-D inversion. Such ”trade-off” curves were determined for all inversions steps in all three different approaches a, b and c.

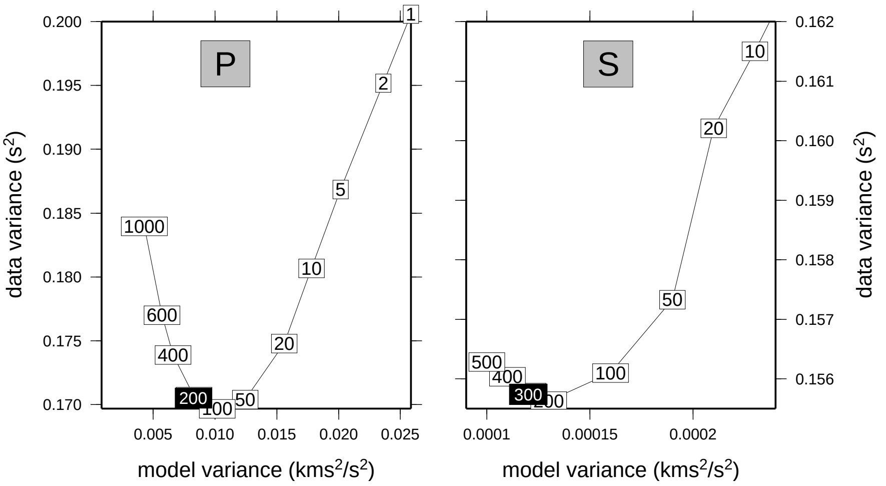

Figure 6.3: The model variance plotted versus data variance for different damping values for the direct 3D inversion. The trade-off curves for v_P (left) and v_P/v_S (right) models are used to determine the preferred damping values, which are marked with black background colour.

6.1 Resolution

An important part of a seismic tomography study is the assessment of the solution quality. Regions of good resolution need to be separated from poorly resolved zones. As discussed in Section 4.2.2, the spread function of the resolution matrix is a possibility to asses the resolution of the model nodes. In contrast to classical methods as hit count or derivative weight sum (DWS), the full resolution matrix contains informations about the interdependence between model parameters which influence the model resolution [Schurr, 2000]. In Figure 6.4 the spread values for the v_P and v_P/v_S models are shown. However, following Toomey and Foulger [1989] and Kissling et al. [2001] resolution estimates based on spread values still depend on the damping values and the model parametrization. The threshold which defines the range of acceptable spread values is therefore not universally applicable [Diehl, 2008]. The choice of the threshold is thus based on the ray coverage, the relative size of the spread value and on the results of synthetic checkerboard tests (see next Section).

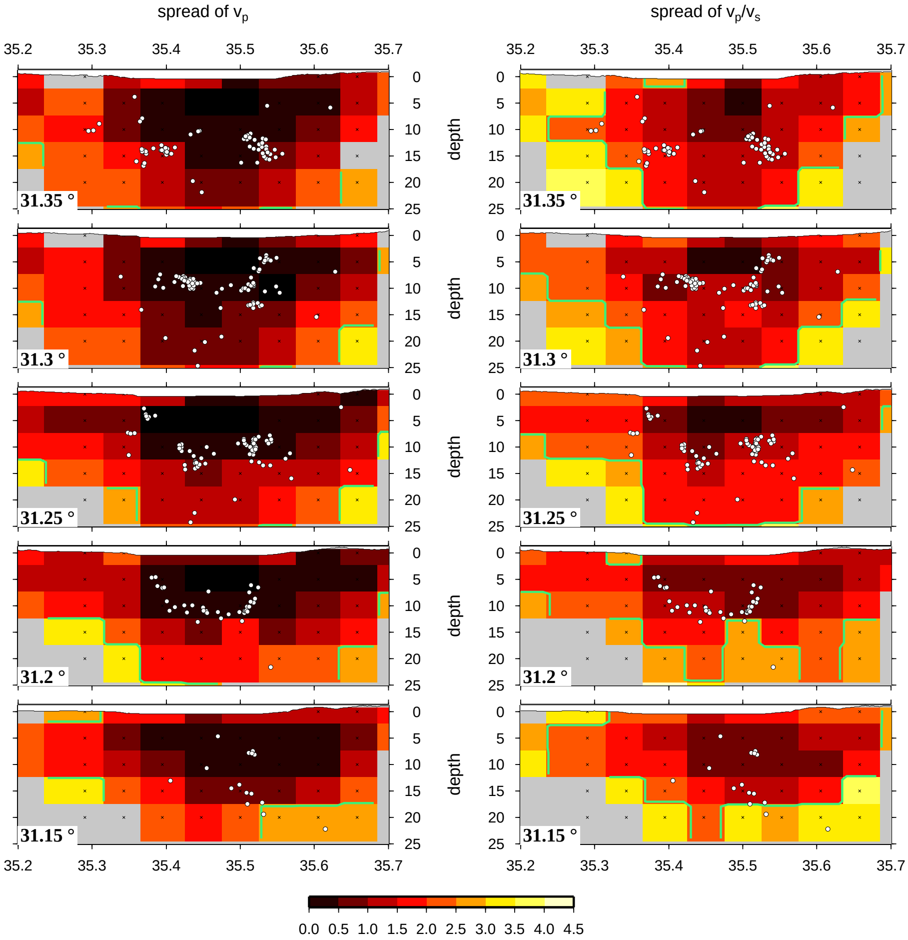

Figure 6.4: Longitude - depth sections of spread values of the model resolution matrix for the 3-D v_P (left) and the v_P/v_S (right) model for different latitudes. The model resolution is high in areas where the spread matrix holds low values. White dots are indicating events around the section and crosses are indicating the model nodes. The green contour lines border regions with acceptable resolution. Vertical exaggeration (VE) 1.4.

6.1.1 Checkerboard - Tests

A widespread method to asses the resolving capacity of the given model configuration involves synthetic checkerboard tests. Checkerboard models are built up of lateral and vertically alternating positive and negative velocity perturbations of a background model (Figure 6.5-6.7). Whether the regular structure of the checkerboard model is recovered or not helps to distinguish regions of different resolution capacity.

The checkerboard model is generated by superimposing the initial velocity model of the real inversion with velocity perturbations of $\pm 5\%$ of the absolute velocity value. Afterwards, forward calculation of travel time data within this synthetic model is done. The resulting travel times are then disturbed with random noise, the extent of which dependent on the pick accuracy. Gaussian distributed random noise was added, following Husen et al. [2000], with a standard deviation ranging from 0.01 for highest quality observations, to 0.05, for lowest quality observations for the P wave onsets. For the S wave onsets the values for the different quality observations are ranging between 0.02 and 0.10. The noise was added using the program `simul_random` [Haberland, 1999]. In the last step the resulting travel times were inverted using the original station and event distribution.

The results for checkerboard test with $2 \times 2 \times 2$ model nodes perturbations are shown in map view in Figure 6.5 and in longitude - depth section in Figure 6.6 for the P velocity model and the model of v_P/v_S ratios, respectively. Between 35.35° and 35.55°E longitude and until a depth of 12 km the perturbations are very well restored, affirming the good ray coverage within the basin and near to its boundaries. Furthermore in the north until 31.25°N latitude the well restored part reach 20 km depth due to deeper earthquakes in the north. In order to obtain the limit of the restoring capacity of the model also perturbations applied to each model node are tested (Figure 6.7). In the basin and at its eastern boundary, until a depth of about 12 km, the shape of these checkerboards can be restored but not their amplitude.

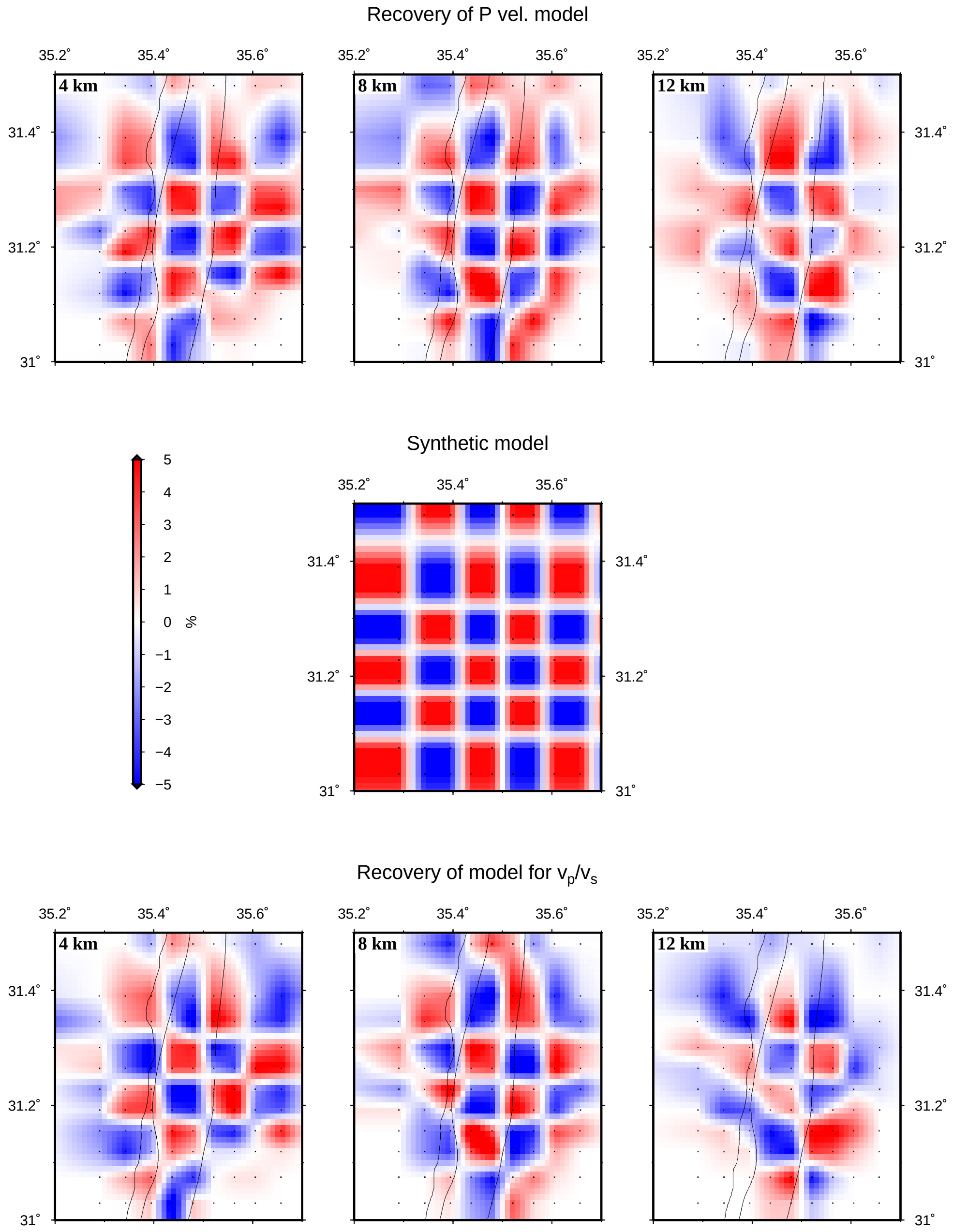

Figure 6.5: Map view of the reconstruction of the 2 × 2 × 2 checkerboard model for v_P at different depth (top row). Original 2 × 2 × 2 checkerboard model (middle). Map view of the reconstruction of the model for the v_P/v_S ratios at different depth (bottom row). Fine black lines indicate the main boundary faults.

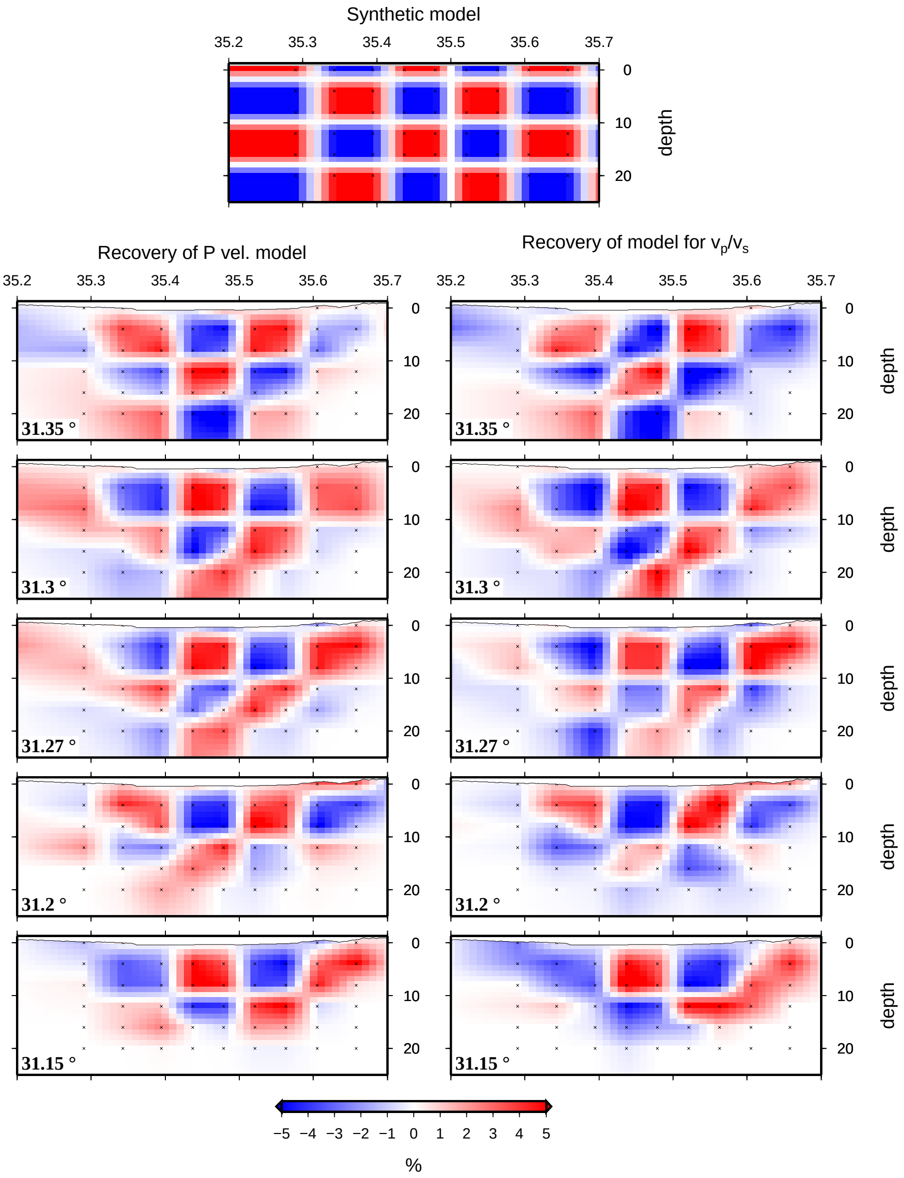

Figure 6.6: Longitude - depth sections of the original $2 \times 2 \times 2$ checkerboard model (topmost) and the reconstruction of the synthetic v_P model (left column) and the model of v_P/v_S ratios (right column) at different latitudes. Crosses indicate the model nodes. VE: 1.4.

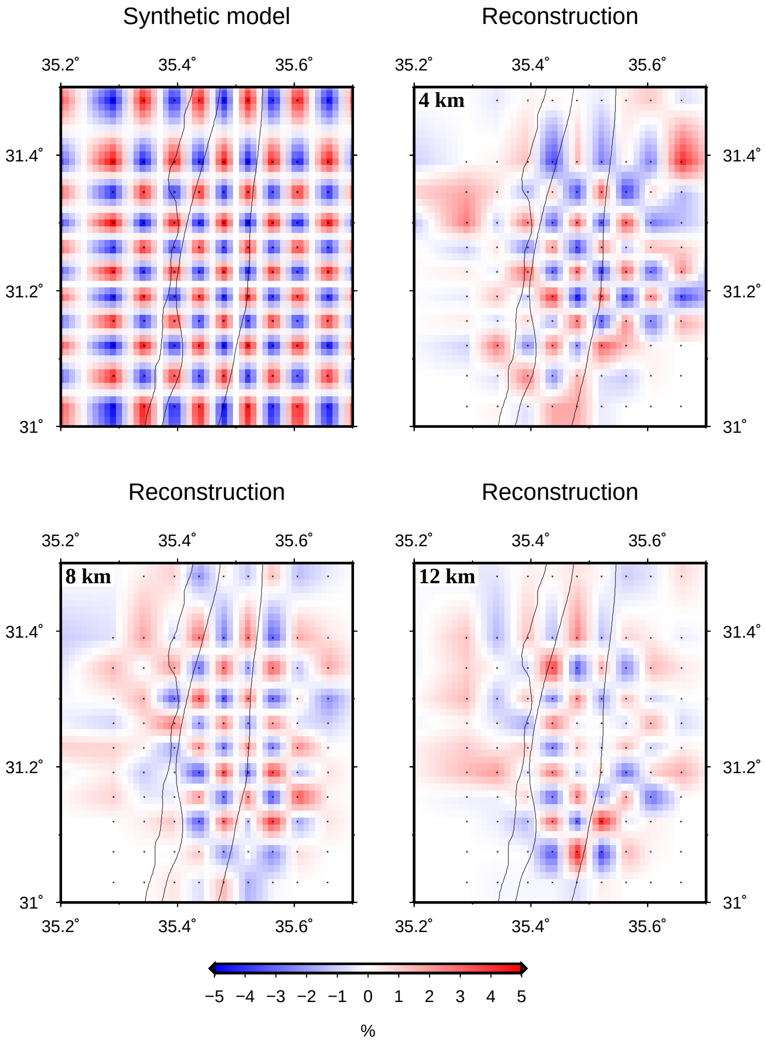

Figure 6.7: Map view of the reconstruction of the one node checkerboard model for v_P at different depth. Fine black lines indicate the main boundary faults.

6.1.2 Model recovery Tests

An important disadvantage of checkerboard tests is that the unrealistic velocity structure of the checkers is likely to result in ray paths different from the ray paths in the real model. Therefore, synthetic model recovery tests are applied where synthetic models, preferably close to the real model, are used for the forward calculation. A synthetic structure, close to the observed one, lies in the same local mathematical minimum of the solution space [Husen et al., 2000]. In the same way as for the checkerboard tests, the calculated traveltimes are disturbed with noise and again inverted using the original experimental setup.

In Figure 6.8 the recovery tests for different simple 2-D synthetic models are presented. While the structure of the basin near to the surface is known, its deeper structure (symmetric or asymmetric) and its depth is unclear. Thus, symmetric and asymmetric basin models with depth of 8, 12 and 16 km are tested for the P velocity model (Figure 6.8). All six different recovery models are clearly distinguishable, thus the station and earthquake distribution of the investigation area seems to be able to model the principal structure of the basin. In the same way the model of v_P/v_S ratios was perturbated with higher values in the centre (sedimentary basin in Figure 6.9) compared to the background model which holds v_P/v_S values slightly below the average value deduced from the Wadati diagram analysis (Figure 5.1 auf Seite 48). As for the checkerboard tests of the models of v_P/v_S ratios, the resulting travel times of the forward modeling were perturbed by random noise with a higher standard deviation than for the P velocity model. Also here, the recovery of the different symmetric and asymmetric structures of different depths is satisfying, indicating a good resolution also for the models of v_P/v_S ratio. This is of special importance as the contrast in the v_P/v_S ratio between fluid containing sediments and ”dry” rocks, as e.g. the crystalline basement, is expected to be significant. Furthermore, the high number and quality of the S onsets in the dataset should lead to a consistent model of v_P/v_S ratios.

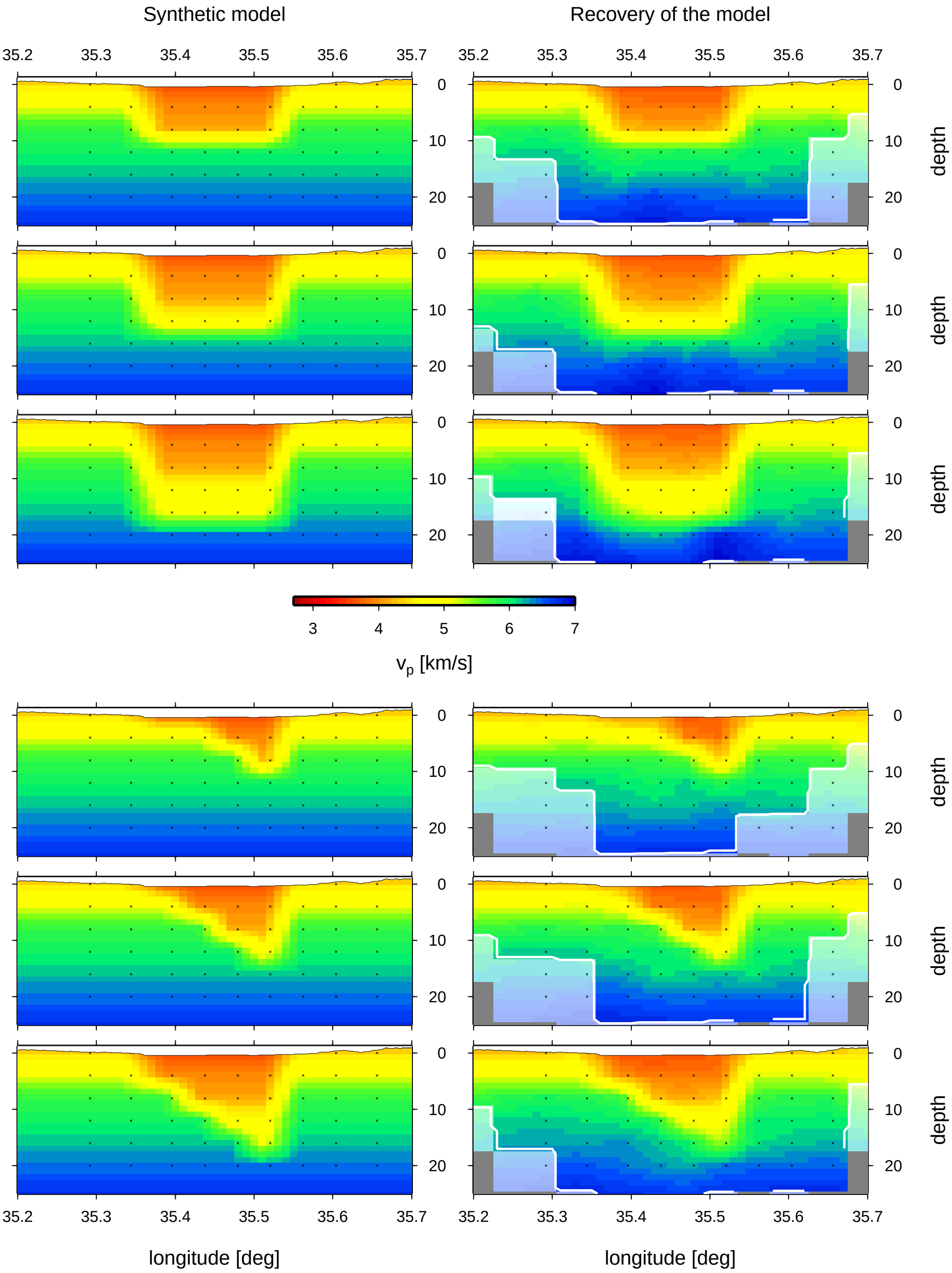

Figure 6.8: Assessment of the resolution for the expected sedimentary basin characterized by lower P velocities. Longitude - depth sections of synthetic model recovery tests with original model on the left and recovered model on the right. Regions with lower resolution are faded, whereas unresolved regions are coloured in grey. The white contour encloses regions of good resolution defined by the spread value in combination with the checkerboard test. Model nodes are indicated by crosses. VE: 1.4

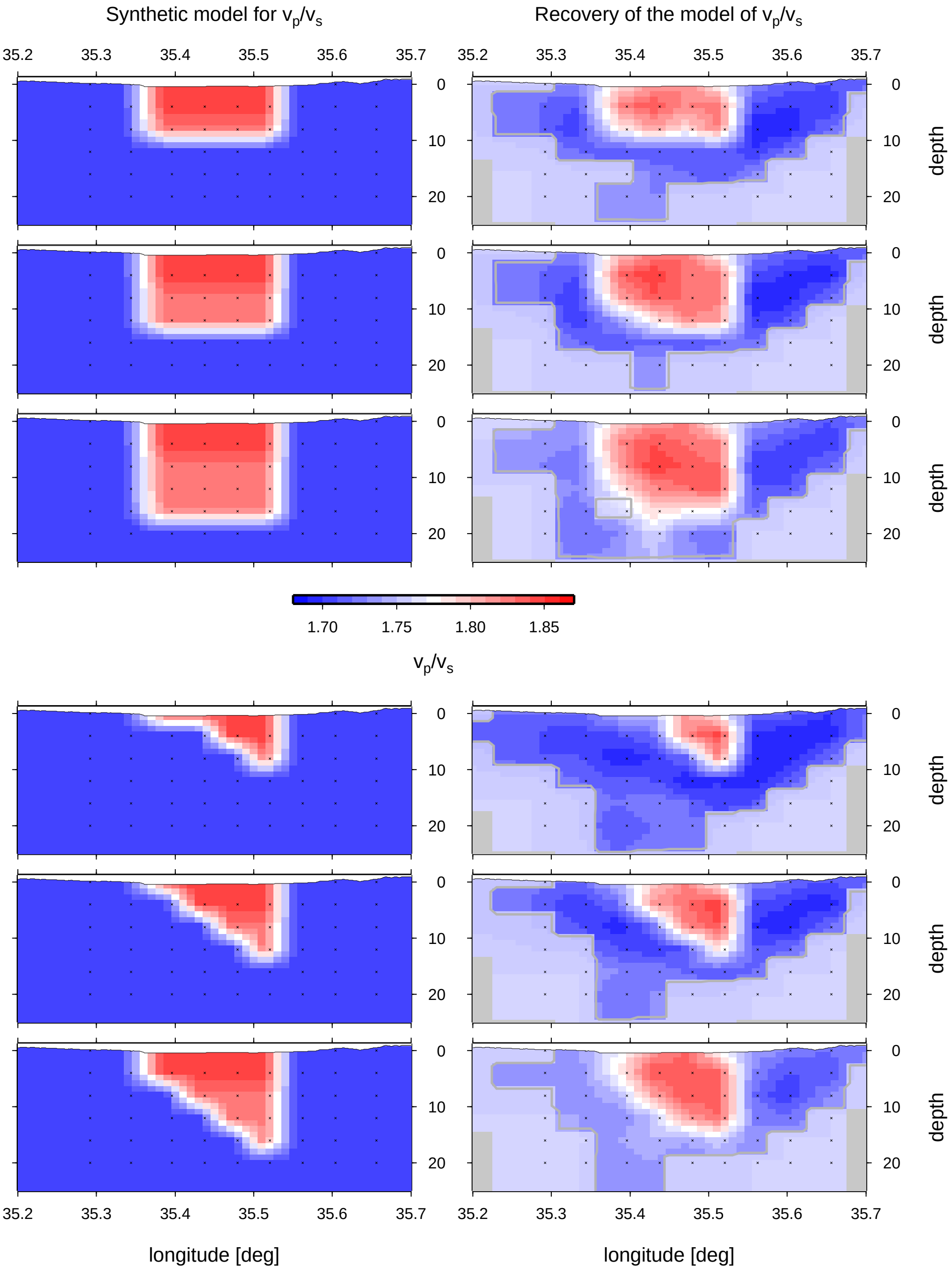

Figure 6.9: Assessment of the resolution for the expected sedimentary basin characterized by higher v_P/v_S ratios. Longitude - depth sections of synthetic model recovery tests with original model on the left and recovered model on the right. Regions with lower resolution are faded, whereas unresolved regions are coloured in grey. The white contour encloses regions of good resolution defined by the spread value in combination with the checkerboard test. Model nodes are indicated by crosses.VE: 1.4

6.2 Results

6.2.1 2-D Model

As already discussed, the expected main feature of the tomographic models is two dimensional, the sedimentary basin. The presented models for the v_P model and the model of the v_P/v_S ratios are rotated 8° clockwise to align approximately with the main boundary faults trending NEW-SWS (see Figure 6.10 in Section 2.2). The v_P model is represented by absolute values, by velocity - depth functions, as well as by deviations of the 1-D initial model presented in Chapter 5 (Figure 6.10). The v_P model is characterized by a similar velocity pattern west of 35.35°E and east of 35.55°E. From 3.5-4 km/s at the surface the velocity is increasing to about 5.5 km/s at about 8 km depth. This is reflecting the thin layer of sediments overlaying the basement at the basin shoulders. The basin between 35.43°E and 35.52°E exhibits lower velocities at the surface (3-3.5 km/s) and a lower velocity gradient, resulting in velocities of only about 4 - 4.5 km/s at 8 km depth. At 16 km depth, velocities of about 5 km/s are observed, indicating a velocity reduction compared to the regions east and west of the basin. The eastern boundary of this low velocity zone is vertical from 5 to 17 km depth. The western boundary shows an inclination to the east from the surface to the lower border at about 17 km depth.

The P velocity is furthermore presented as velocity - depth (v-d) functions at three different longitudes (Figure 6.10). The v-d function at 35.39°E, representing the western shoulder, shows a constant increase of the velocity between the surface and 8 km depth from 3.5 km/s to 5.6 km/s, followed by a very low velocity gradient down to 20 km depth where a velocity of 5.8 km/s is reached. The v-d function at 35.48°E, representing the basin, displays a low velocity gradient from the surface, where $v_P = 3.8$ km/s to 16 km depth, where $v_P = 4.8$ km/s. From 16 to 20 km depth the velocity is increasing to 5.6 km/s, showing a high velocity gradient. This high gradient can be assigned to the lower boundary of the low velocity body of the sedimentary basin.

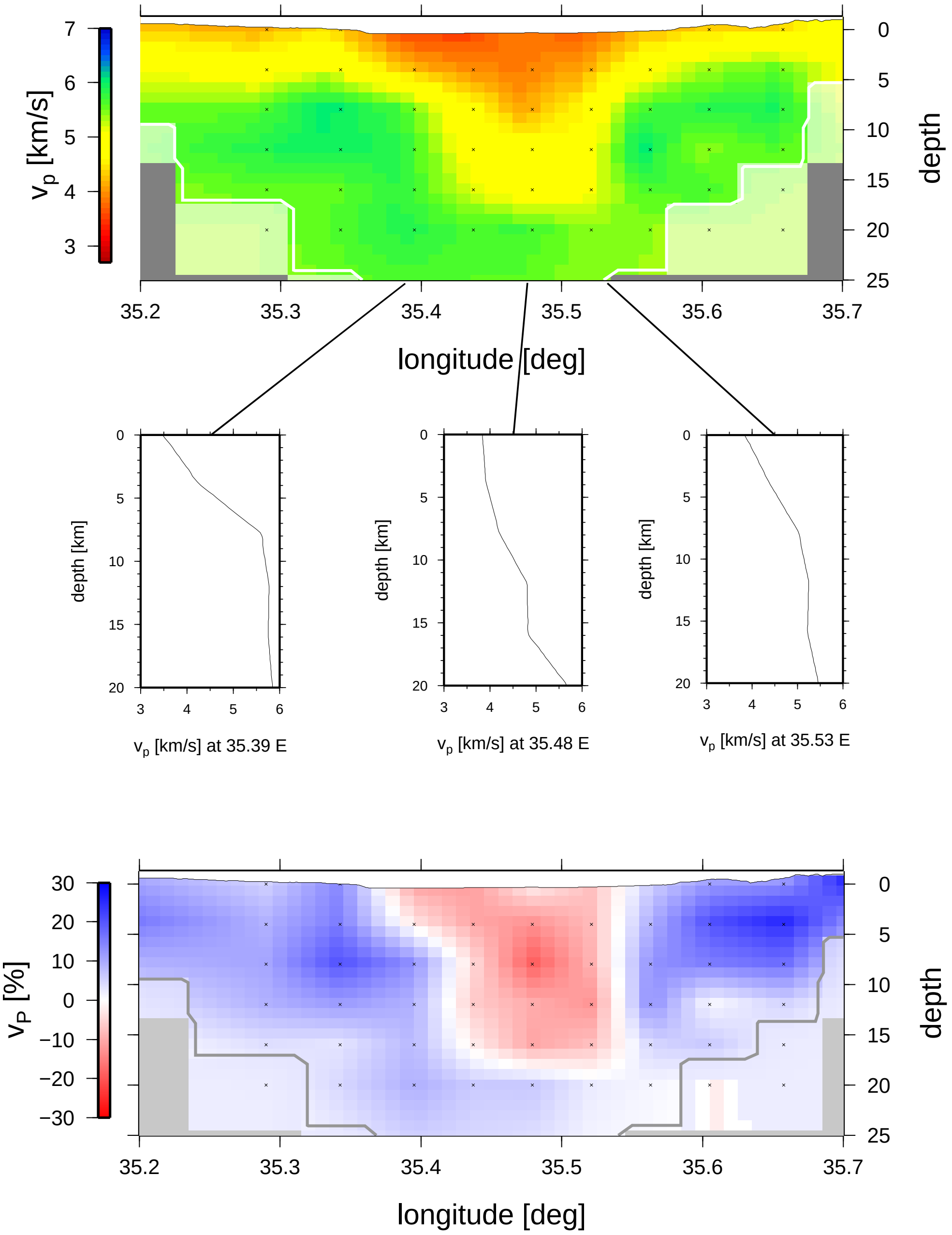

Figure 6.10: 2-D tomographic P velocity model for the southern part of the Dead Sea basin (top: v_P, middle: v_P - depth functions, bottom: deviations of v_P from the background model). Unresolved regions are coloured in grey. The grey contour encloses regions of good resolution defined by the spread value in combination with the checkerboard test. Model nodes are indicated by crosses. VE: 1.4

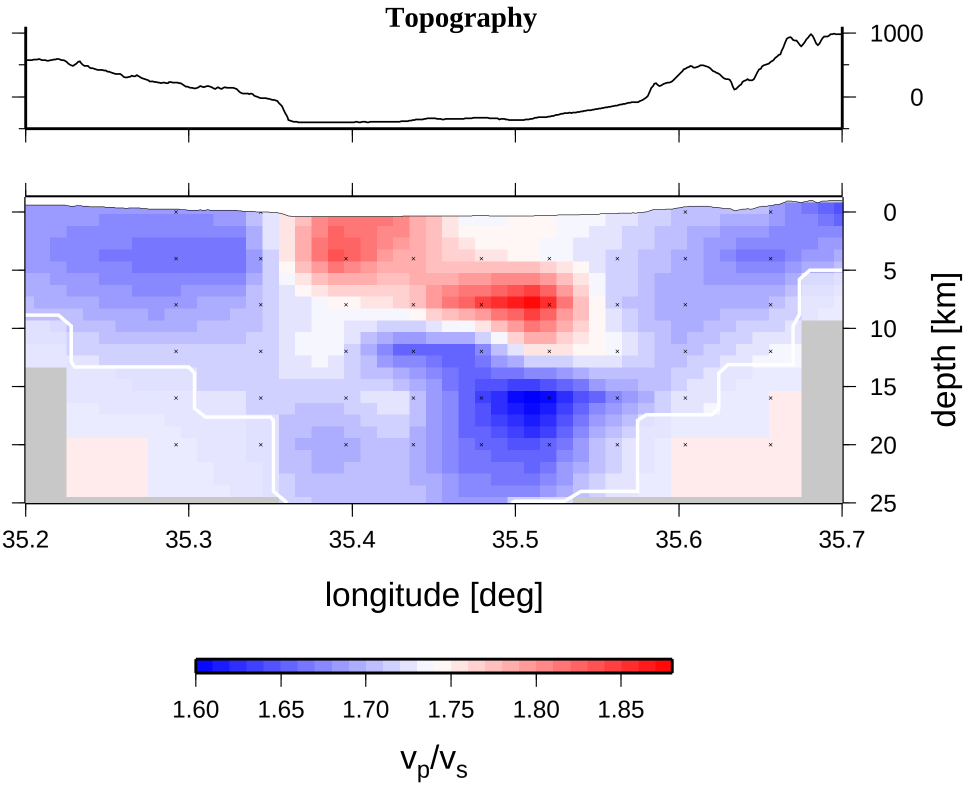

Figure 6.11: Topographic profile (top, VE: 6) and 2-D tomographic model of v_P/v_S ratios (bottom) for the southern part of the Dead Sea basin. Unresolved regions are coloured in grey. The grey contour encloses regions of good resolution defined by the spread value in combination with the checkerboard test. Model nodes are indicated by crosses. VE: 1.4

The eastern shoulder, represented by the v-d function at 35.53°E, displays a constant velocity increase from 3.8 km/s at the surface to 5 km/s at 8 km depth, followed by a lower velocity gradient between 8 and 20 km depth where a velocity of 5.5 km/s is reached.

The difference between the basin and the shoulders is revealed even more clearly when the v_P model is displayed as deviations from the background model (Figure 6.10 bottom). Between 35.35°E and 35.55°E the sedimentary basin is represented by P velocities of up to 25 % slower than in the background model. Similarly large differences to the background model are found in other sedimentary basins, e.g. the Erzincan basin in eastern Turkey [Kaypak, 2008]. The lower boundary of the relatively low velocities is reached at about 17 km depth. The eastern boundary of this low velocity zone is vertical from the surface down to the lower boundary. The western boundary is inclined to the east, especially in the uppermost 7 km. From the combination of the absolute v_P model (Figure 6.10 top), the consideration of the velocity gradient in the velocity - depth functions (Figure 6.10 center) and the relative v_P model (Figure 6.10 bottom), a lower boundary of the low velocity and thus of the basin is assumed to be at about 17 km depth.

Sedimentary rocks are characterized by Poisson's ratios μ ranging from 0.25 to 0.45, mostly depending on its fluid content, while for crystalline "dry" (low fluid content) rocks, μ is usually about 0.25 [Sharma, 1997]. Poisson's ratio is directly related to the ratio of P and S velocity (see equation 4.7 in Chapter 4). Thus the v_P/v_S ratio should be sensitive to changes from fluid containing (sedimentary) rocks to the basement or other "dry" rocks. The model of the v_P/v_S ratios in Figure 6.11 is characterized by distinct areas of high ($>$1.74) and low ($<$1.74) ratios. West of 35.35°E and east of 35.55°E low values are observed from surface to depth. In between, the basin is characterized by high values from the surface to about 7 km depth. At the western boundary below this depth the ratios change to average values of 1.74 and below, indicating a change in fluid content. The high values at the eastern boundary reach about 12 km depth. The shallow structure is thus similar in the v_P model and in the model of the v_P/v_S ratios with a vertical eastern boundary and an inclined western boundary, while the lower boundary is about 17 km for the v_P model but only 12 km for the model of the v_P/v_S ratios.

In the upper 4 km around 35.5°E v_P/v_S ratios of about 1.74 are observed. In the next section it will be shown, that this is an effect of the three dimensional structure of the model of v_P/v_S ratios in this region.

6.2.2 3-D Model

The results of the 3-D tomography are given in W-E cross sections, N-S cross sections and in map view (Figure 6.12-6.20). Well resolved regions, as defined in Section 6.1, are enclosed by spread contour lines, whereas regions of lower resolution appears in faded colours. In regard to the fact that all models recovered from inversion procedures are non-unique, results of all three different approaches (a), (b) and (c) are presented in Figure 6.12 (v_P) and 6.13 (v_P/v_S). All three sections of the P velocity model for all three approaches show common features (Figure 6.12): In the centre, between 35.4°E and and 35.55°E the velocity increases slowly from 3 km/s at the surface to about 5 km/s at 10 - 15 km depth. However, east and west of this centre part the velocity is higher at the surface (mostly about 4 km/s, at some places over 5 km/s) and above 5.5 km/s at 10 km depth.

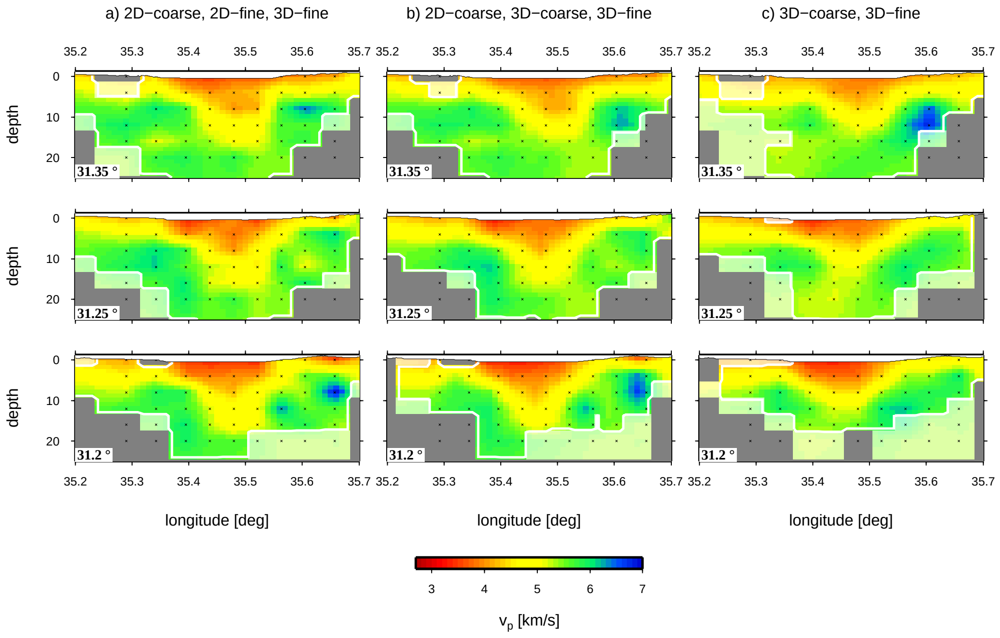

Figure 6.12: West-east depth sections through the 3-D v_P model for different latitudes. The results for the three different approaches a, b and c are presented. For explanation see text. Regions with lower resolution are faded, whereas unresolved regions are coloured in grey. The white contour encloses regions of good resolution defined by the spread value in combination with the checkerboard test. Model nodes are indicated by crosses. VE = 1.4.

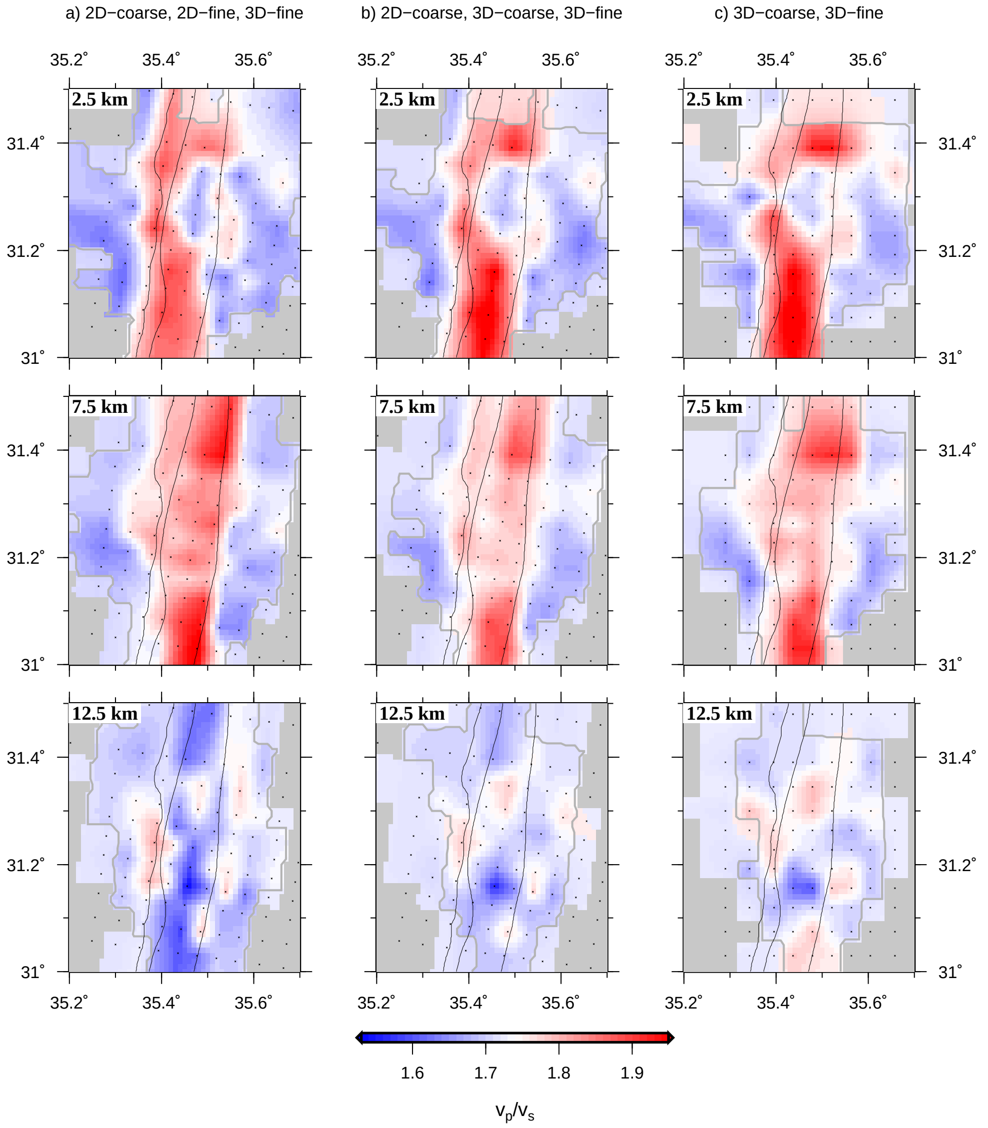

Figure 6.13: Depth maps of the 3-D model of v_P/v_S ratios. Depths are indicated in the upper left corner. Regions with lower resolution are faded, whereas unresolved regions are coloured in grey. The grey contour encloses regions of good resolution defined by the spread value in combination with the checkerboard test. Model nodes are indicated by crosses, fine black lines indicate the main boundary faults.

In most of the sections the eastern boundary of this low velocity body in the centre is only slightly inclined or vertical, while the western boundary of the low velocity body is in all sections inclined to the east. The differences are very small between models (a) and (b) in Figure 6.12 while in model (c) the low velocity part in the centre is generally shallower and the different inclination of the eastern and western boundary is not recovered.

The model of v_P/v_S ratios is shown in map view for different depth in Figure 6.13. The centre of all three models is characterized by high ratios (> 1.8) and the eastern and western edges are characterized by lower ratios (< 1.74) down to 7.5 km depth. At 2.5 km depth a region around 31.5°N/35.44°E show lower values below 1.7 in all three models. At 12.5 km depth, low, mean and high values, changing within small distances, are observed, indicating a change compared to the clear structure above.

For a final consideration, the results of approach (b) are discussed in detail. As mentioned before, a more stable solution is expected from a gradual approach (e.g. Eberhart-Phillips et al. [1995], Husen et al. [2000], Haberland et al. [2009]). No features in the models, which are not revealed through both approaches (a) and (b), will be discussed. Results are presented on W-E and N-S cross sections and in map view (Figure 6.14-6.20).

The principal P velocity structure is represented as deviations of the 1-D initial model of Chapter 5 in Figure 6.14 and Figure 6.15. The principal pattern of the P velocity remains stable from 31.35°N to 31.15°N (Figure 6.14). The shoulders of the basin west of about 35.35°E and east of about 35.55°E are imaged through high velocities, between 5 and 30 % above the background model. The basin displays low velocities, 5 - 25 % higher than the background model from the surface down to 16-18 km depth. The eastern boundary between low and high values image a vertical line from the surface down to the lower border. The western boundary of the low velocity body is inclined to the east with slightly different angles at different latitudes. The lower boundary of the low velocity body is reached at about 16 km depth at 31.35°N and at about 17 km depth from 31.3°N to 31.25°N. From 31.2°N to 31.15°N the well resoluted area is limited to 17 km depth were low velocities are displayed, hence the low velocity body reaches at least 17 km from 31.2°N to 31.15°N.

The eastern shoulder is generally characterized by higher deviations from the background model than the western shoulder. Furthermore the highest positive deviations (up to 30 %) from the background model are found in the upper 10 km at the eastern shoulder east of 35.5°E and south of 31.35°N (Figure 6.14/6.15). Large part of the seismicity can be assigned to the eastern and western boundary (section at 31.25°N and 31.3°N in Figure 6.14). However, no seismicity occurs at the lower boundary of the low velocity body (Figure 6.14). Instead, many events occur between 9 and 13 km depth within the low velocity body (depth maps at 10 and 12.5 km depth in Figure 6.15). Furthermore, there is activity west of the basin at about 15 km at 31.35°N, which does not seem directly related to the basin.

Absolute P velocities are presented in Figure 6.16 and Figure 6.17. West of about 35.35°E and east of about 35.55°E velocities of 4-4.5 km/s at the surface are observed, increasing to at least 5.5 km/s at 5 km depth. The basin displays velocities of about 3 km/s at the surface, increasing slowly to 4.5-5 km/s in 10-15 km depth. The contrast between the eastern shoulder and the basin appears to be abrupt at 31.35°N, 31.3°N and 31.15°N where at 8 km depth the velocity is decreasing from 5.5 km/s to 4.5 km/s within about 4 km from east to west. From 31.2°N to 31.25°N the velocity decrease is more gentle, forming an eastern boundary of the low velocity body inclined to the west. The western boundary of the basin shows gentler decrease of the velocity for all sections from west to east, thus the western boundary is inclined to the east. In the section at 31.2°N it is noticeable that at about 36.63°E a high velocity depth gradient arises. From the surface to 6 km depth the velocity is increasing from 4 km/s to 6.5 km/s. Velocity values of 6.5 km/s at only 6 km depth are very unlikely. As it is limited to only two grid nodes and appears in a region where small anomalies are not well resolved (see Figure 6.7), it is most likely an artefact of the inversion.

In map view (Figure 6.17), the basin is clearly identifiable by lower velocities compared to its shoulders in all depth maps until 12.5 km depth. Its position fits well with the main boundary faults observed at the surface which are indicated in Figure 6.17 as well. At depth of 12.5 and 15 km the lower velocities appear not at the western faults, indicating an asymmetric form of the basin.

Strong contrasts are observable in the model of v_P/v_S ratios (Figure 6.18 -

6.20). High ratios (>1.8) are characterizing the basin down to a depth of 10 km. However, around 31.3°N/35.5°E average values of 1.74 and lower appear at 2.5 and 5 km depth. This is most likely representing the Lisan salt diapir, as salt cannot contain significant amount of fluids which would dissolve it. Thus, salt is characterized by v_P/v_S ratios similar to crystalline "dry" rocks (1.73 and below). The highest v_P/v_S ratios (up to 2) are found between 2.5 and 5 km depth south of 31.2N and north of 31.35N (Figure 6.19). Below the salt diapir around 31.3°N/35.5°E in 7.5 km depth values slightly above the average value of 1.74 are revealed (Figure 6.18). A very strong contrast between high (>1.9) and low (<1.65) v_P/v_S ratios is found at 31.15°N between 5 and 10 km depth.

The seismicity can be mostly assigned to the boundary between high and low v_P/v_S ratios. Thus the events in the centre of the basin at depth between 9 and 12 km are representing the lower boundary of the fluid containing sediments (e.g. section at 31.2/31.25/31.3°N in Figure 6.18) and not the lower boundary of the basin fill represented by the change in the P velocities (Figure 6.14).

In Figure 6.20 a north - south profile at 35.48°E clearly displays a contrast in the v_P/v_S ratio representing the lower limit of the fluid containing sediments. It is between 10 and 14 km deep with minimum depth at 31.4°N and 31.16°N and maximum depth at 31.34°N and 30.7°N. The salt diapir, characterized by ratios of 1.7 and below, extends at 31.2°N from the surface to depth of about 6 km.

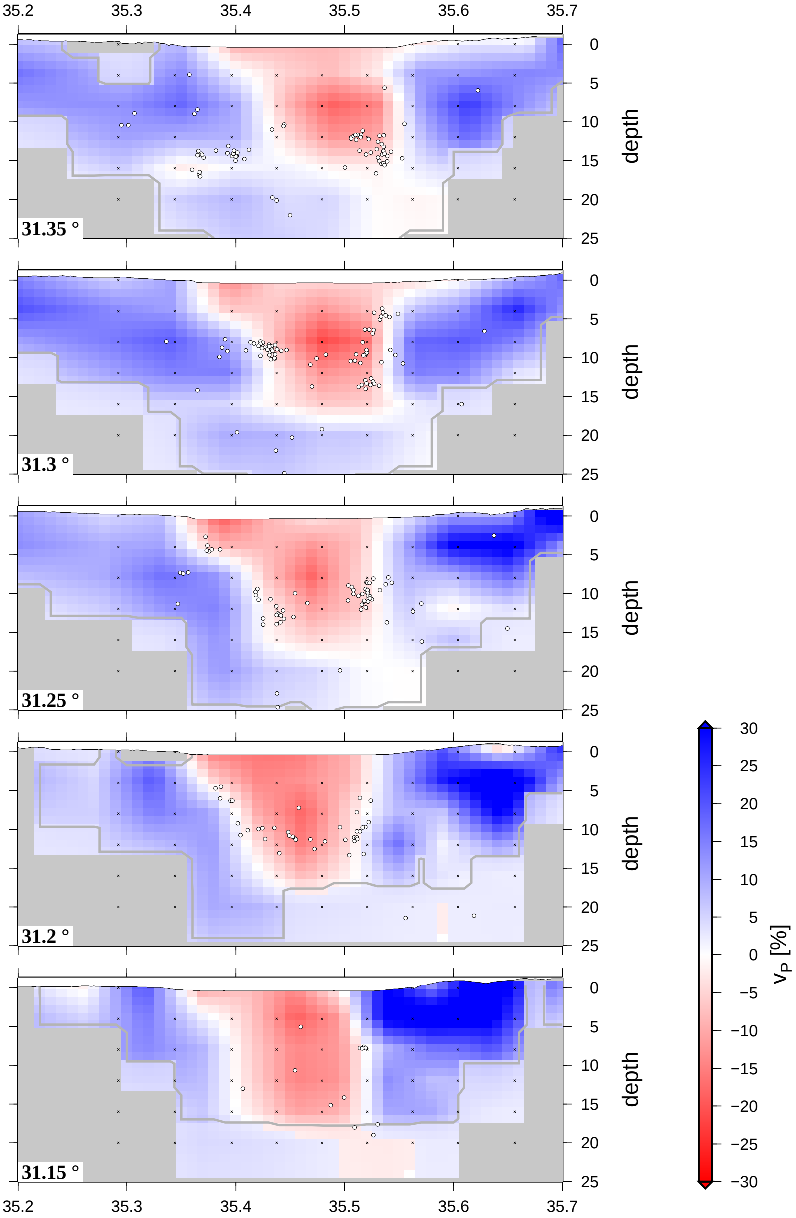

Figure 6.14: West-east depth sections through the 3-D v_P model, displayed as deviations from the 1D starting model, at different latitudes indicated in the lower left corner. Earthquakes within 5 km of the section are plotted as white dots while the model nodes are indicated by black crosses. Regions with lower resolution are faded, whereas unresolved regions are coloured in grey. The grey contour encloses regions of good resolution defined by the spread value in combination with the checkerboard test. VE: 1.4

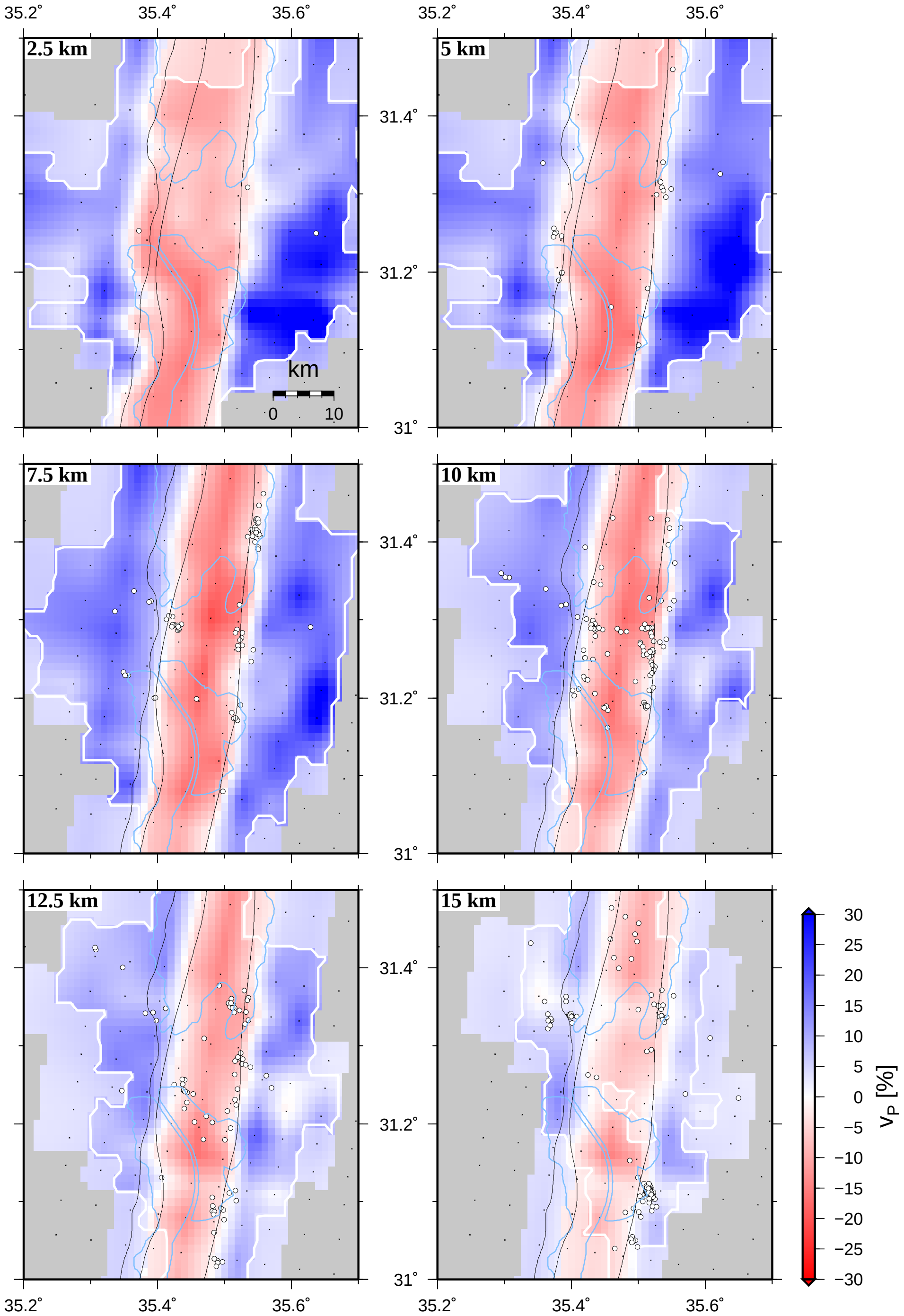

Figure 6.15: Depth maps of the 3-D v_P velocity model, displayed as deviations from the 1D starting model. Depths are indicated in the lower left corner. Earthquakes within 5 km of the layer are plotted as white dots while the model nodes are indicated by black crosses. Regions with lower resolution are faded, whereas unresolved regions are coloured in grey. The white contour encloses regions of good resolution defined by the spread value in combination with the checkerboard test. Fine black lines are indicating the boundary faults, light blue lines the coastline.

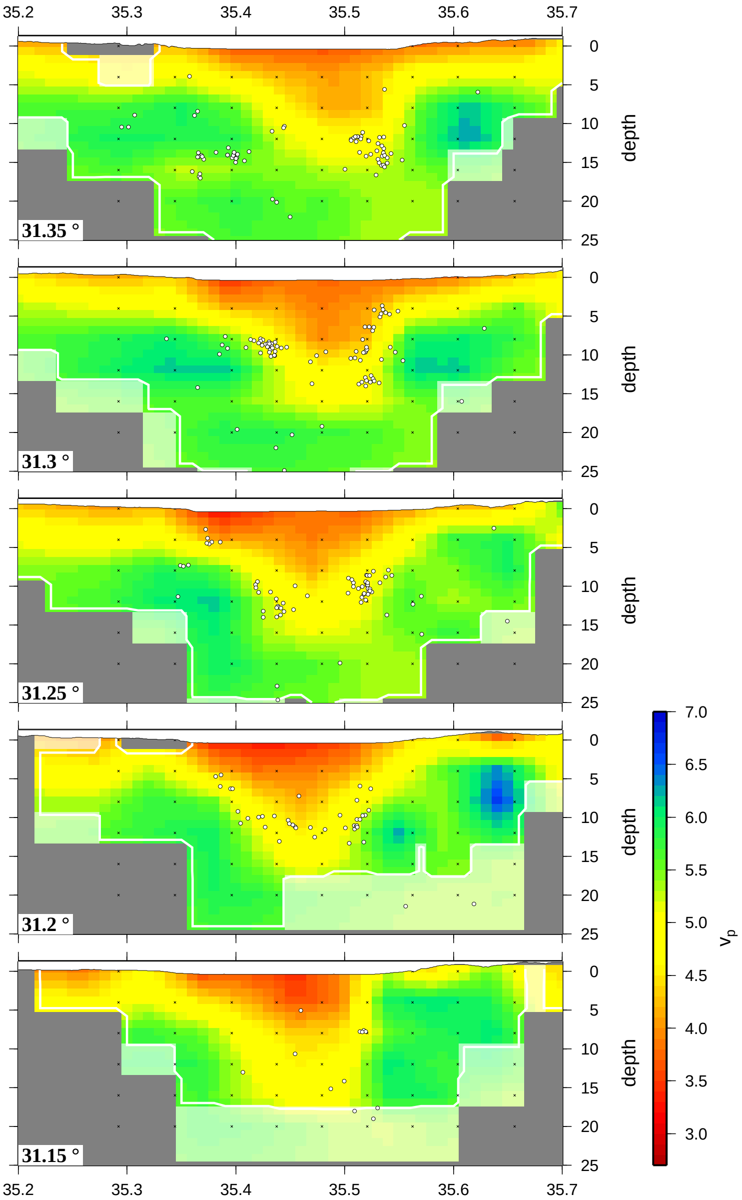

Figure 6.16: West-east depth sections through the 3-D v_P model at different latitudes indicated in the lower left corner. Earthquakes within 5 km of the section are plotted as white dots while the model nodes are indicated by black crosses. Regions with lower resolution are faded, whereas unresolved regions are coloured in grey. The white contour encloses regions of good resolution defined by the spread value in combination with the checkerboard test. VE: 1.4

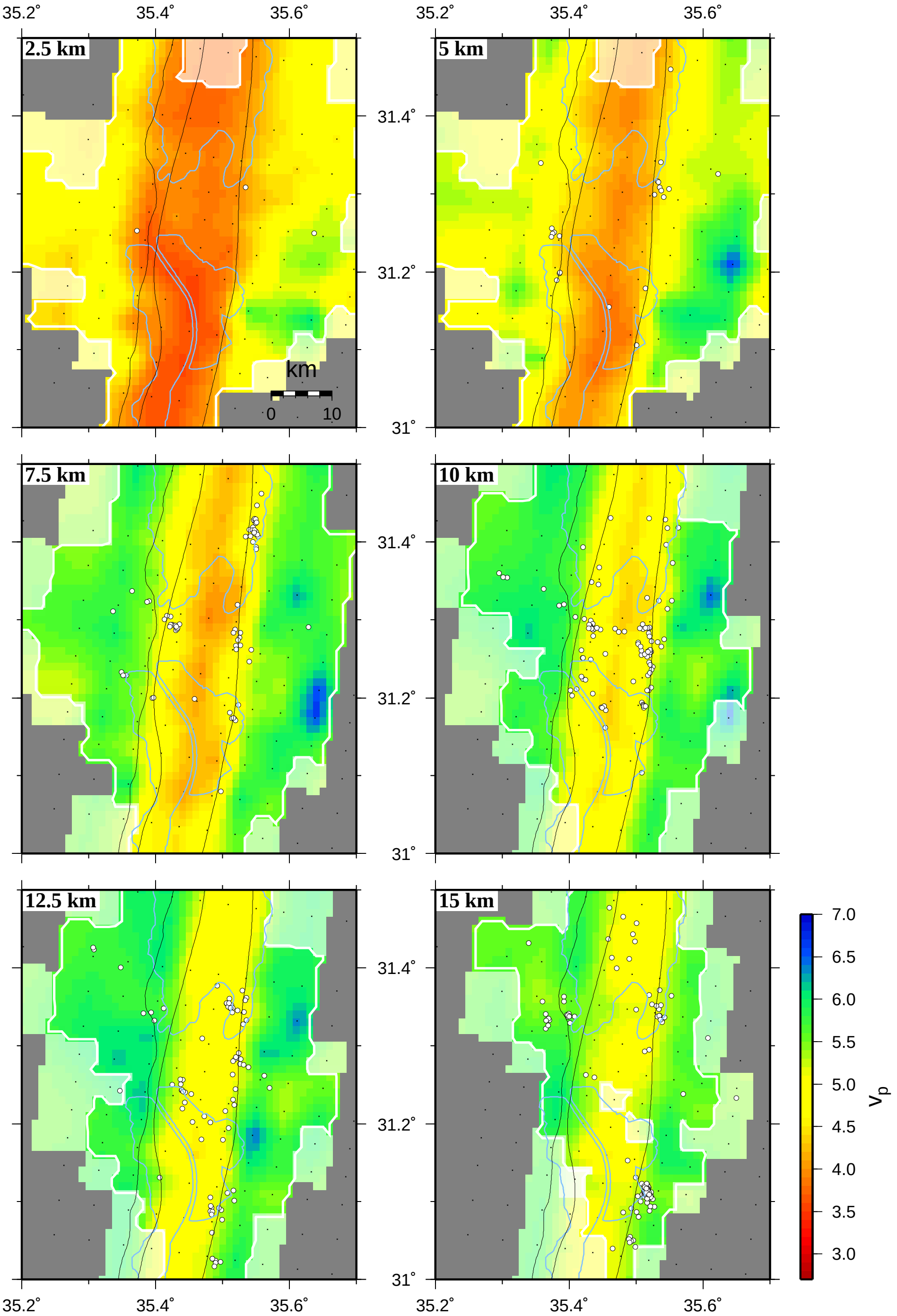

Figure 6.17: Depth maps of the 3-D v_P velocity model. Depths are indicated in the lower left corner. Earthquakes within 5 km of the layer are plotted as white dots while the model nodes are indicated by black crosses. Regions with lower resolution are faded, whereas unresolved regions are coloured in grey. The white contour encloses regions of good resolution defined by the spread value in combination with the checkerboard test. Fine black lines are indicating the main faults, light blue lines the coastline.

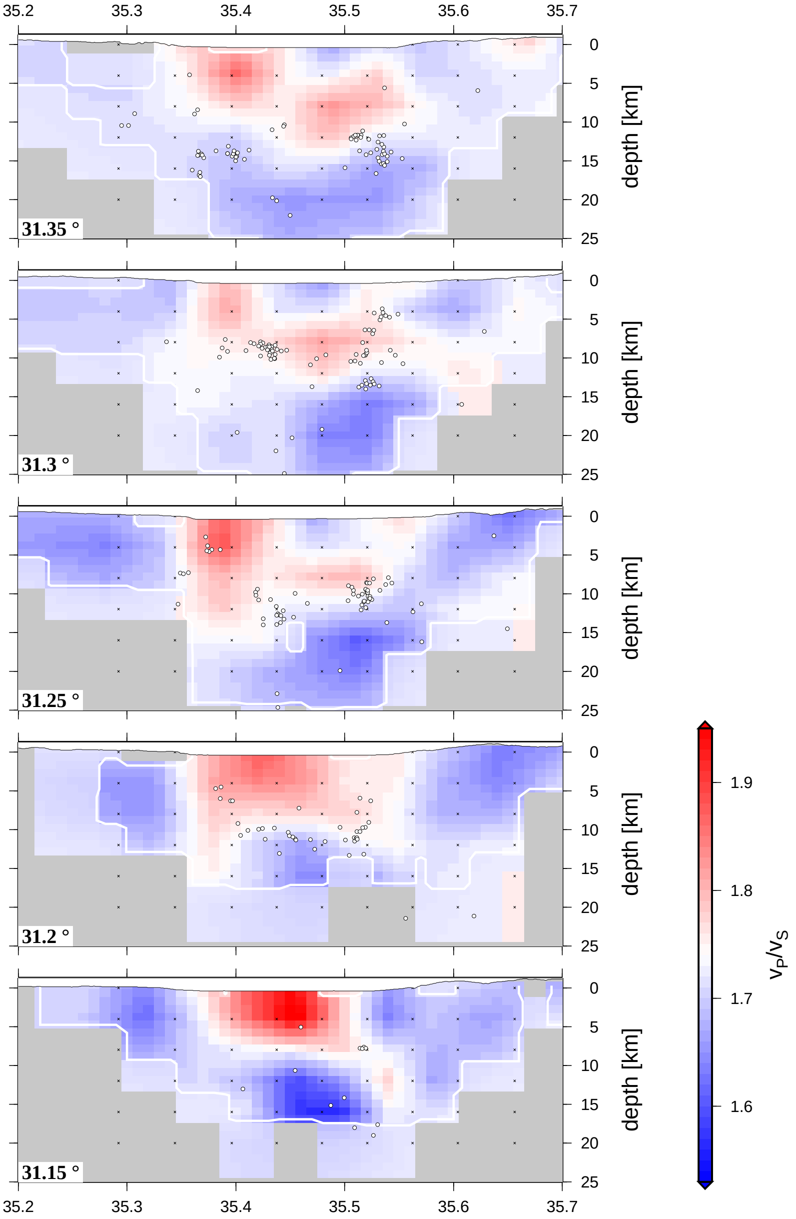

Figure 6.18: West-east depth sections through the 3-D model of v_P/v_S ratios at different latitudes indicated in the lower left corner. Earthquakes within 5 km of the section are plotted as white dots while the model nodes are indicated by black crosses. Regions with lower resolution are faded, whereas unresolved regions are coloured in grey. The white contour encloses regions of good resolution defined by the spread value in combination with the checkerboard test. VE: 1.4

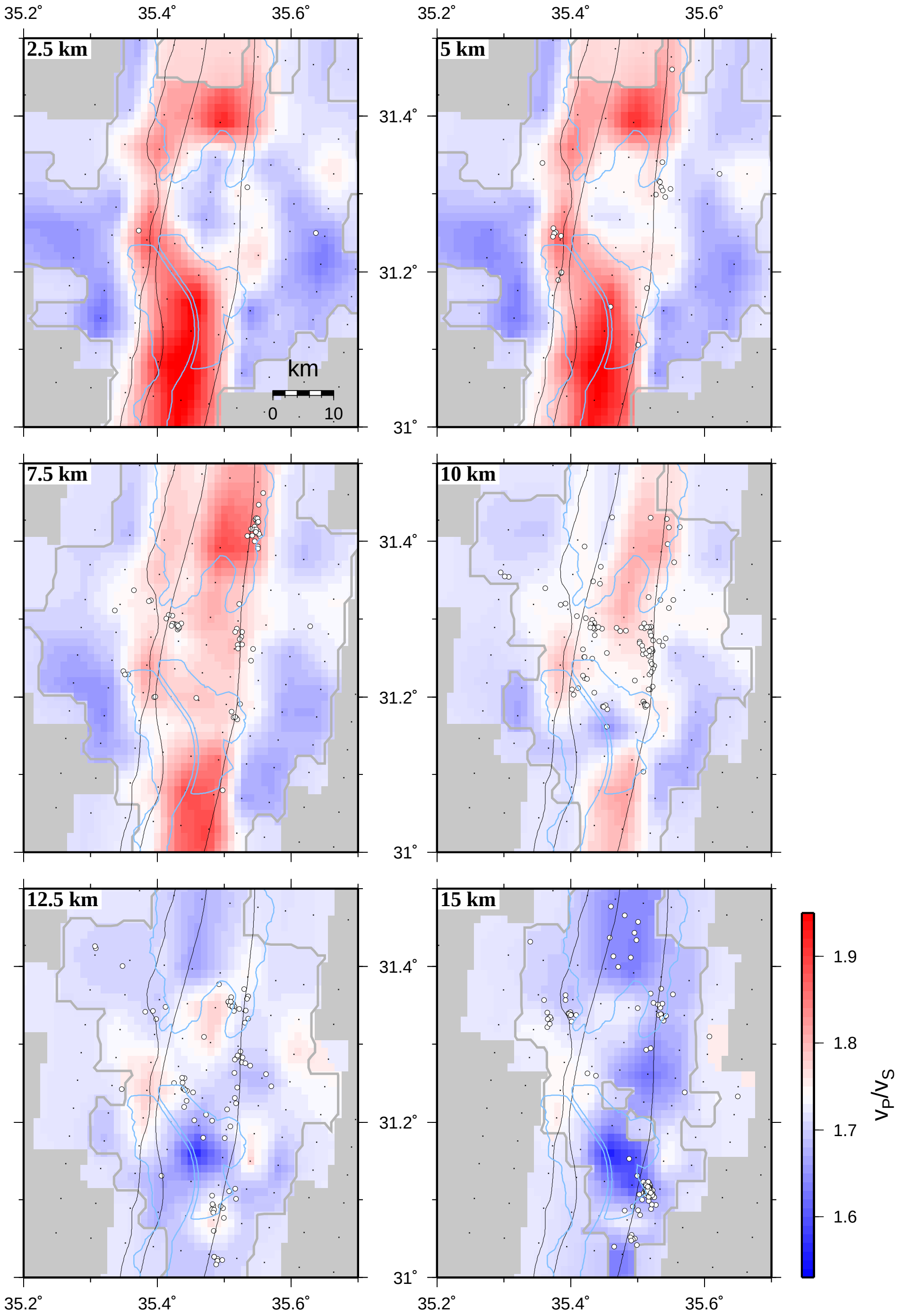

Figure 6.19: Depth maps of the 3-D model of v_P/v_S ratios. Depths are indicated in the lower left corner. Earthquakes within 2.5 km of the layer are plotted as white dots while the model nodes are indicated by black crosses. Regions with lower resolution are faded, whereas unresolved regions are coloured in grey. The grey contour encloses regions of good resolution defined by the spread value in combination with the checkerboard test. Fine black lines indicate the boundary faults, light blue lines the coastline.

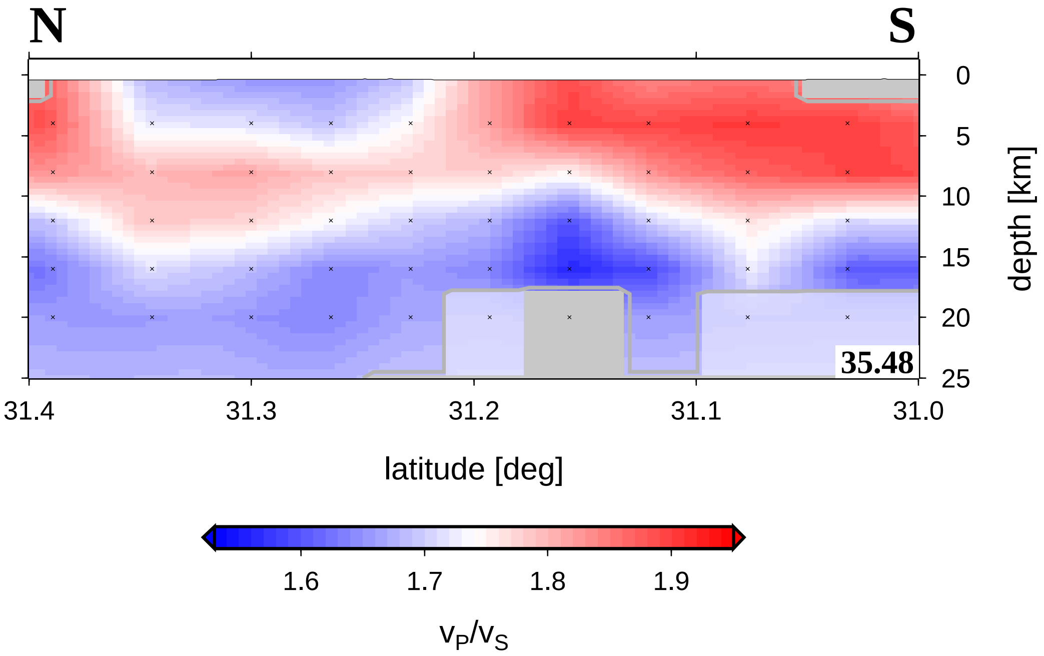

Figure 6.20: North - south depth section through the 3-D model of v_P/v_S ratios at 35.48°E. The model nodes are indicated by black crosses. Regions with lower resolution are faded, whereas unresolved regions are coloured in grey. The grey contour encloses regions of good resolution defined by the spread value in combination with the checkerboard test. VE: 1.4

Chapter 7

Seismicity

7.1 Distribution of the Seismicity

To compare the magnitude values of this study with values from the regional network database it is essential to use the same magnitude scale. The Geophysical Institute of Israel (GII), who is running the regional network in the Dead Sea area, is using the duration or coda magnitude M_d. Originally introduced by Bisztricsany [1958] for surface waves, it employs the fact that the total length of the seismic wavetrain reflects the size of the event. The GII is using the total duration of the wavetrain as proposed by Solov'yev [1965]. Unfortunately, for our dataset it was difficult to determine the length of the wavetrain coherently over several stations (mainly for the smaller events) due to very different noise conditions at different stations. In contrast, the maximum amplitude of the S wave was well definable for a large number of stations, even for smaller events. Hence, a local magnitude $M_L = logA - logA_0$, using the zero-to-peak amplitude A of the S waves, was determined. The term $-logA_0$ corrects for the different epicentral distances. It is scaled so that for an earthquake of $M_L = 3$, at a distance of 100 km, the zero-to-peak amplitude A becomes 1 mm when measured with a Wood-Anderson seismograph [Richter, 1958]. For central California Bakun and Joyner [1984] established the relation for M_L:

$$M_L = logA - logA_0 = logA + [nlog(R/100) + K(R - 100) + 3] \qquad (7.1)$$

where R (in km) is the hypocentral distance, K is an attenuation coefficient and n is the geometrical spreading factor. To establish a local magnitude scale it would be necessary to determine the coefficients n and K for the region by using local seismicity data, but the size of the local database is insufficient. Instead, M_L was determined using $n = 1$ and $K = 0.00301$ from Bakun and Joyner [1984]. For a subset of larger events M_d was determined. Using M_d and M_L values for the same events, a linear relationship between both was established to convert the determined local magnitude values of the local dataset to the duration magnitude values of the regional database:

$$M_L = 0.9938M_d + 0.8405 \qquad (7.2)$$

Thus, the magnitude values determined are comparable to those reported from the GII.
For 621 events the magnitude determination was possible. In Figure 7.1 their size distribution is indicated. Only thirty events in the whole dataset show magnitudes above two while the largest events show magnitudes below M=5. The magnitude of completness M_C, defined as the lowest magnitude at which 100% of the events in a space-time volume are detected [Rydelek and Sacks, 1989], is 0.4.

The distribution of the microseismicity in the southern Dead Sea basin can be presented with high accuracy (Figure 7.2). Seismicity occurs from a depth of 2 km down to depth of 29 km, which agrees with Aldersons et al. [2003]. The activity is concentrated in the area between 7 and 17 km depth. Three distinct depth segments of high rate of seismicity can be identified in the depth distribution histogram (Figure 7.2d). Large part of the seismicity occurred north of 31.15°N at shallow depth between 8 and 11 km. The second peak in the depth distribution histogram around 15 km depth is mainly a result of activity south of 31.13°N where a spatial and temporal

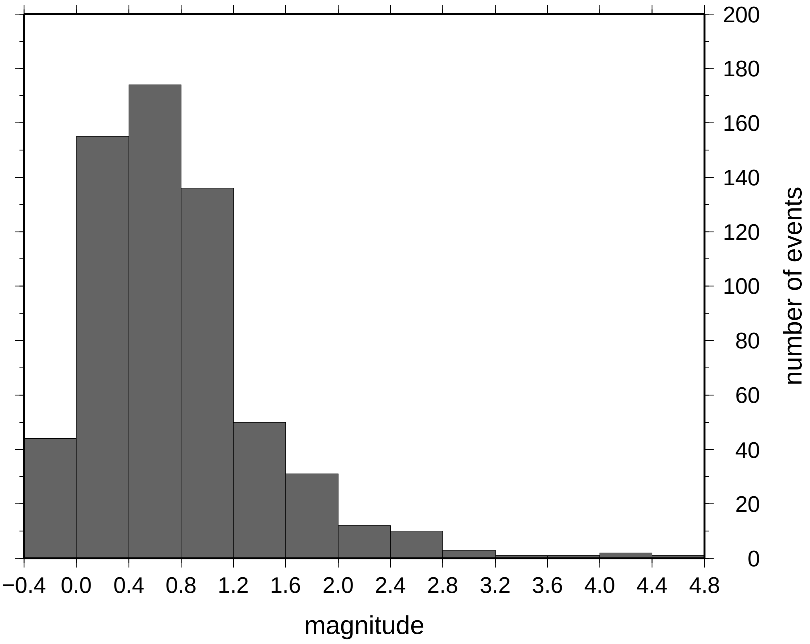

Figure 7.1: Histogram for number of events for different magnitudes.

cluster occurred in February 2007 - this will be discussed in Section 7.2. Furthermore, some activity is observed in the lower crust around 26 km depth, north of 31.25°N. It does not appear to be related to the faults within the upper crust.

The eastern boundary fault (EBF) is the most active fault of the southern DSB area. Its seismic activity extends over the whole study area from south to north with a small gap between 31.13°N and 31.17°N. It is furthermore traceable as a mainly vertical line from 4 to 19 km depth in the longitude - depth section in Figure 7.3. At 35.5°E/31.1°N a temporal and spatial cluster of 116 events occurred in February 2007 (see Section 7.2).

The activity at the western faults (WF) is mapped from about 3 km depth down to 20 km depth (Figure 7.4). The upper limit of the activity at the WF is inclined to the east by about 45°. It is interesting to note that between 31.15°N and 31.4°N the behaviour of both faults looks similar in the depth - latitude section in Figure 7.3 and 7.4: At 31.2°N seismicity occurs between 4 and 12 km depth. Northwards the lower boundary is increasing continuously

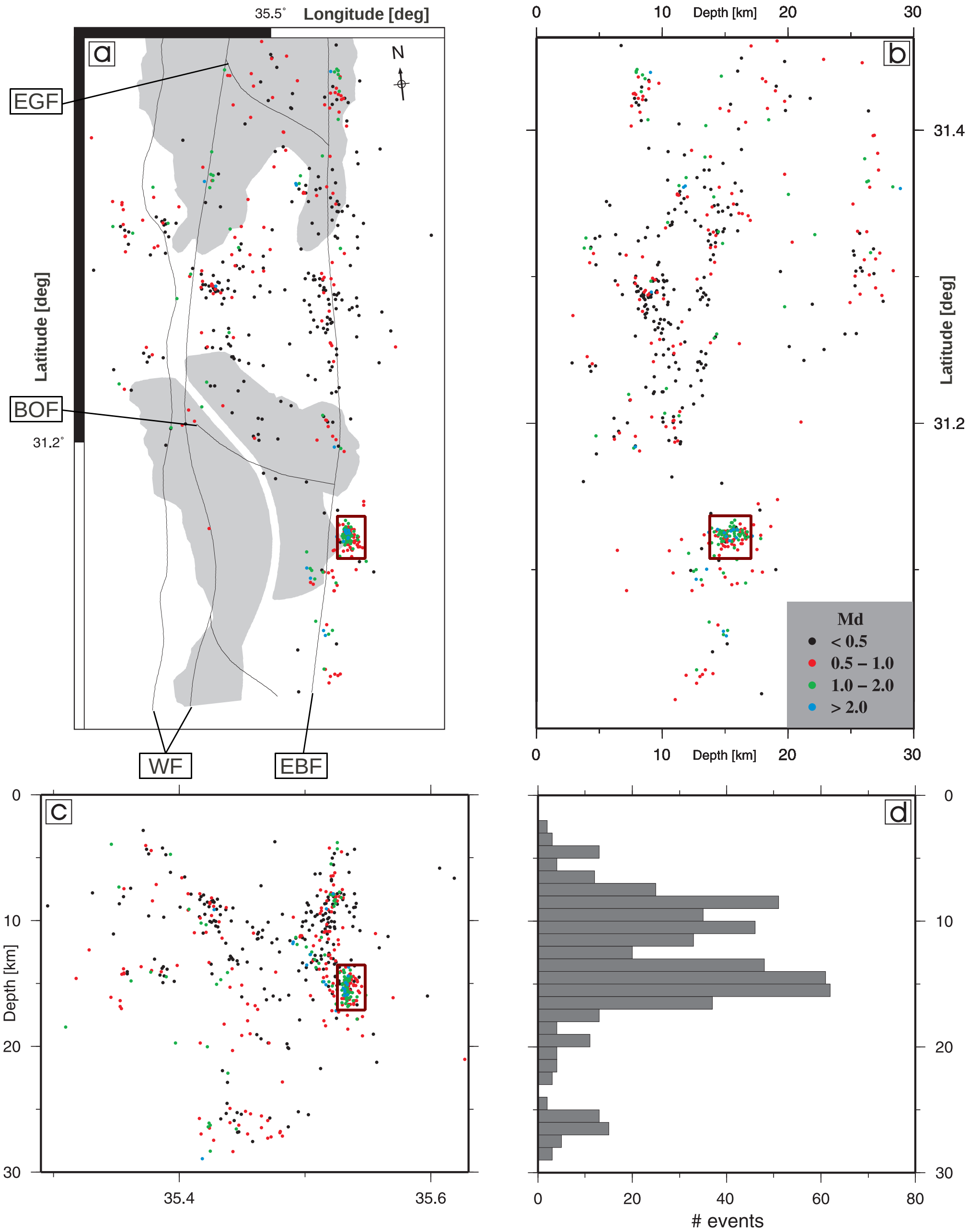

Figure 7.2: To align approximately with the direction of the main boundary faults, the map is rotated 8° ccw (a). The events are marked as dots in different colours, scaled by its magnitude. The main faults are indicated as thin black lines. EBF: Eastern boundary fault, WF: Western faults, BOF: Boqeq fault, EGF: Ein Gedi fault. Projected hypocenters on a vertical cross-section along the main axis of the DSB (b). Projected hypocenters on a vertical cross-section along the transverse axis of the DSB (c). Due to the projection the latitude and longitude values differ slightly from the original values. The red squares in (a), (b) and (c) mark the location of the cluster discussed in Section 7.2. Histogram of events per depth kilometer (d).

to 17 km depth at around 31.4°N for both faults. Thus, it is most likely that the driving forces of the seismicity are the same for the eastern and western boundary faults between 31.15°N and 31.4°N. Meanwhile, south of 31.15°N, only the EBF fault is active, indicating a different seismic regime.

While the seismicity can be clearly assigned to the EBF and the WF, activity concentrated at one of the transverse faults was not found within the recording time (Figure 7.2). However, the transverse Boqeq fault forms the border between the two regions of different seismic regimes (BOF in Figure 7.2). North of 31.4°N, towards the end of the study area, the seismicity at the EBF is concentrated around 8 km depth, while at the WF events occur between 13 and 20 km depth. Thus, the behaviour seems to again be different at each boundary north of 31.4°N. This change in the seismic behaviour is probably related to the transverse Ein Gedi fault (EGF in 7.2).

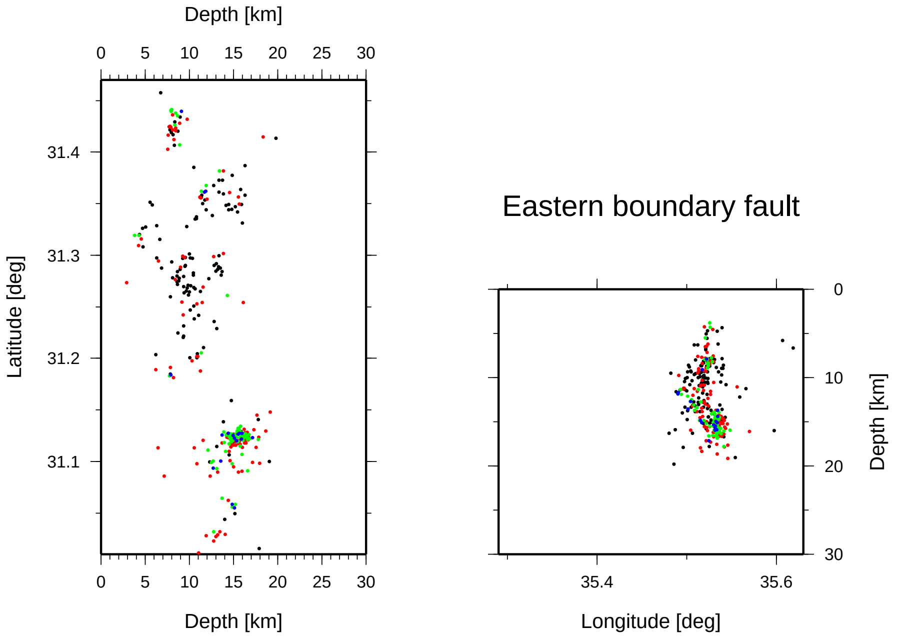

Figure 7.3: Seismicity at the eastern boundary fault. Depth vs. latitude (left). Longitude vs. depth (right). Colour code for magnitude size like in Figure 7.2.

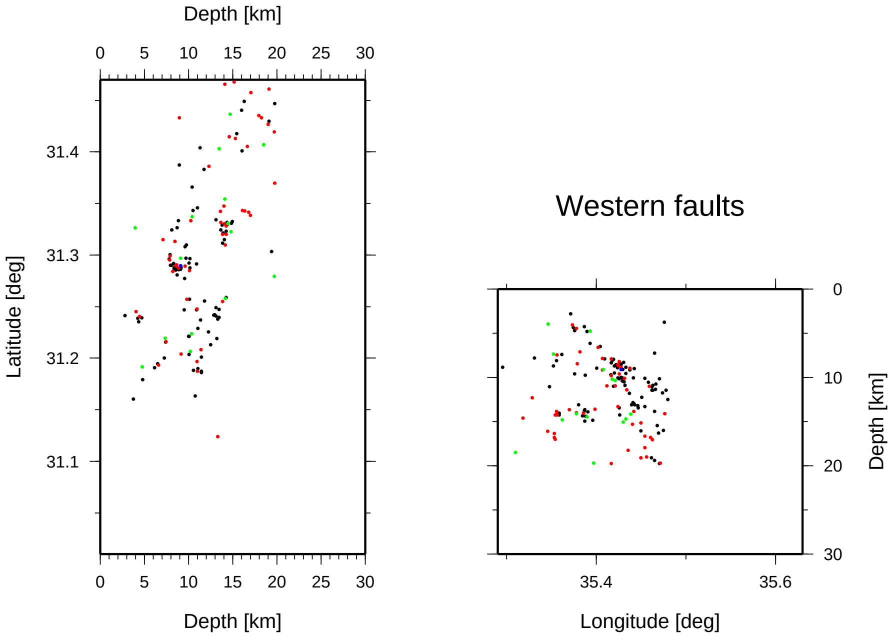

Figure 7.4: Seismicity at the western faults. Depth vs. latitude (left). Longitude vs. depth (right). Colour code for magnitude size like in Figure 7.2.

7.2 Cluster Relocation

Between February, 9th 2007 and March, 4th 2007, 112 events occurred in a very small area in the southeast of the basin between 12 and 16 km depth (red square in Figure 7.2). While the entire earthquake sequence related to that cluster lasted 24 days, within the first 7 hours half of the events occurred (Figure 7.5).

The first and the third events were among the largest of all events during the recording period (M_d of 4.0 and 4.4, respectively). Most of the events show magnitudes between 0.5 and 2.0 while four events, beside the two mainshocks, display magnitudes larger than 2.5 (Figure 7.6).

In addition to the obvious spatial and temporal concentration many of the events in the cluster show similar waveforms, indicating similar source mechanism. Thus, the relative relocation procedure HypoDD (see Section 4.3, Waldhauser [2001]) was applied to reveal a detailed image of the internal structure of the cluster. This processing represents an advance to previous

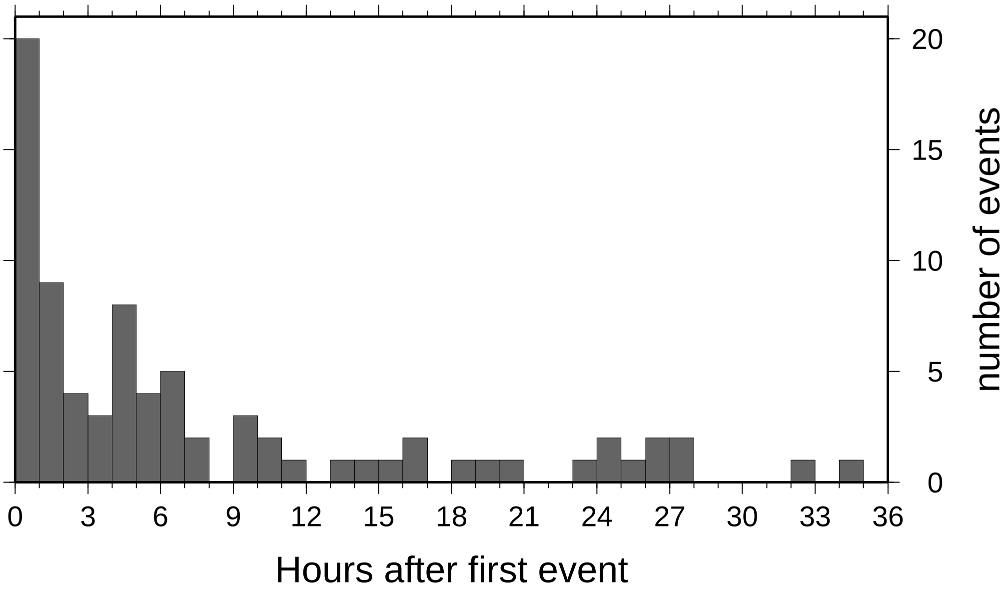

Figure 7.5: Number of events per hour after the first event of the cluster.

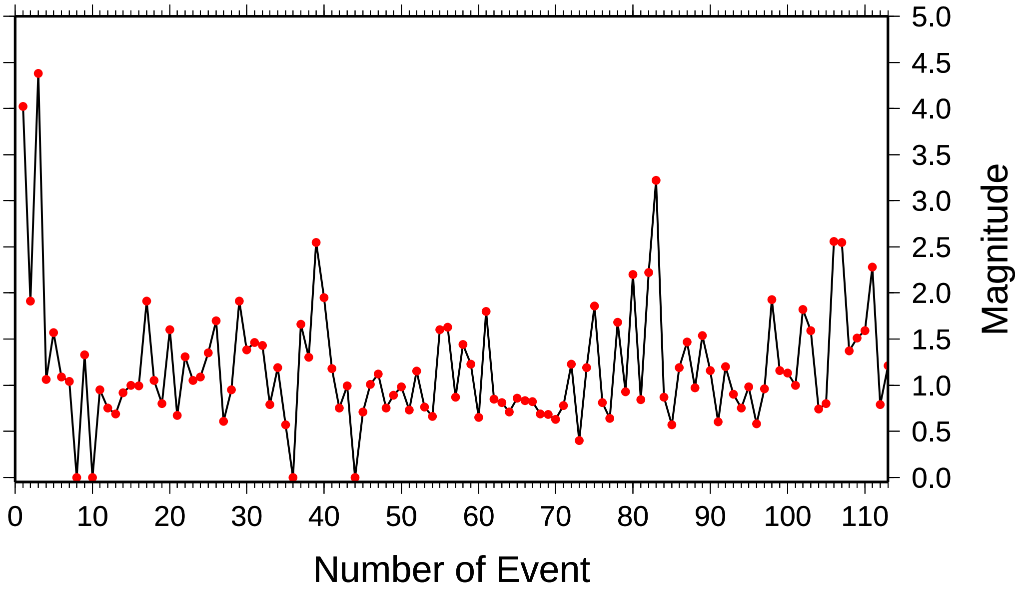

Figure 7.6: Magnitude of the events in the cluster in chronological order.

relative relocation procedures as e.g. Poupinet et al. [1984]. In HypoDD every event belonging to the cluster is treated as a master event and a consistent master-slave relationship for a complete catalog in terms of relative hypocentre locations is sought. HypoDD is incorporating classical absolute travel-time measurements, relative travel-time measurements for two different events at one station and cross-correlation differential travel-time measurements, all for P and S waves. An extensive description of the operation of the HypoDD procedure is given in Waldhauser [2001], while here, only a short overview will be given. HypoDD calculates travel times in a layered velocity model for the current hypocenters at the station where the phase was recorded. The double-difference residuals for event pairs at each station are minimized by weighted least squares using the method of singular value decomposition (SVD, Section 4.3) or the conjugate gradient method (LSQR, Paige and Saunders [1982]). The solution is found by iteratively adjusting the vector difference between nearby hypocentral stations while the locations and partial derivatives are updated after each iteration. While the LSQR option is efficient for large dataset, SVD has the advantage of direct access to location errors.

The relocation of HypoDD is a two-step process. The first step, realized by the program *ph2dt*, searches catalog P- and S-phase data for event pairs with travel time information at common stations and subsamples these data in order to optimize the quality of the phase pairs and the connectivity between the events. The goal is to seek a network of links between events so that there exist a chain of pairwise connected events from any one event to any other event, with the distance being as small as possible between connected events. In *ph2dt* the parameter `MAXNGH` defines the maximum of neighboring events linked to a certain event to build the ”network” within a search radius defined by `MAXSEP`. The search radius should be small compared to event - station distance and the scale length of the velocity heterogeneities. ”Strong” neighbors are considered those which are linked with more than `MINLINK` phase pairs. Only strong neighbors are used to build the network within the cluster. To have at least one observation for each degree of freedom `MINLINK` is typically eight. To find neighboring events the nearest neighbor approach is used. Furthermore, the minimum (`MINOBS`) and maximum (`MAXOBS`) number of observations for each event pair can be defined. This is important in case of a large dataset to limit computing time which is irrelevant in our case, due to the comparable small amount of data. The minimum pick weight for which picks are still included is defined by `MINWGHT`. *ph2dt* removes observations that are defined as outliers. Outliers are considered as delay times that are larger than the maximum expected delay time for a given event pair. These maximum expected delay times are defined as the time for a P- or S- wave to travel between two events and is calculated from the initial event locations and a P- and S- velocity in the focal area of 4 and 2.3 km/s, respectively. To account for uncertainty in the initial locations 0.5 seconds are added to the cutoff.

The chosen parameters for *ph2dt* were:

`MINWGHT`	0.2
`MAXSEP [km]`	2
`MAXNGH`	15
`MINLINK`	8
`MINOBS`	1
`MAXOBS`	116

With these parameters *ph2dt* found 31698 P-phase pairs and 28111 S-phase pairs, while 4 % of the differential times are found to be outliers. Over one thousand strongly linked event pairs with average links per pair of 56 and an average offset between strongly linked events of 0.63 km were detected. In Figure 7.7 the number of differential times, calculated by *ph2dt* for each station for all events, is illustrated.

As cross-correlation delay time measurements are about an order of magnitude more precise than ordinary first-motion picks, the possibility of incorporation of cross-correlation differential travel-time measurements in HypoDD will increase the accuracy of the results significantly. The cross correlation function of two signals $x(t)$ and $y(t)$ is defined as:

$$C(\tau) = \int_{-\infty}^{\infty} x(t)y(t+\tau)dt \tag{7.3}$$

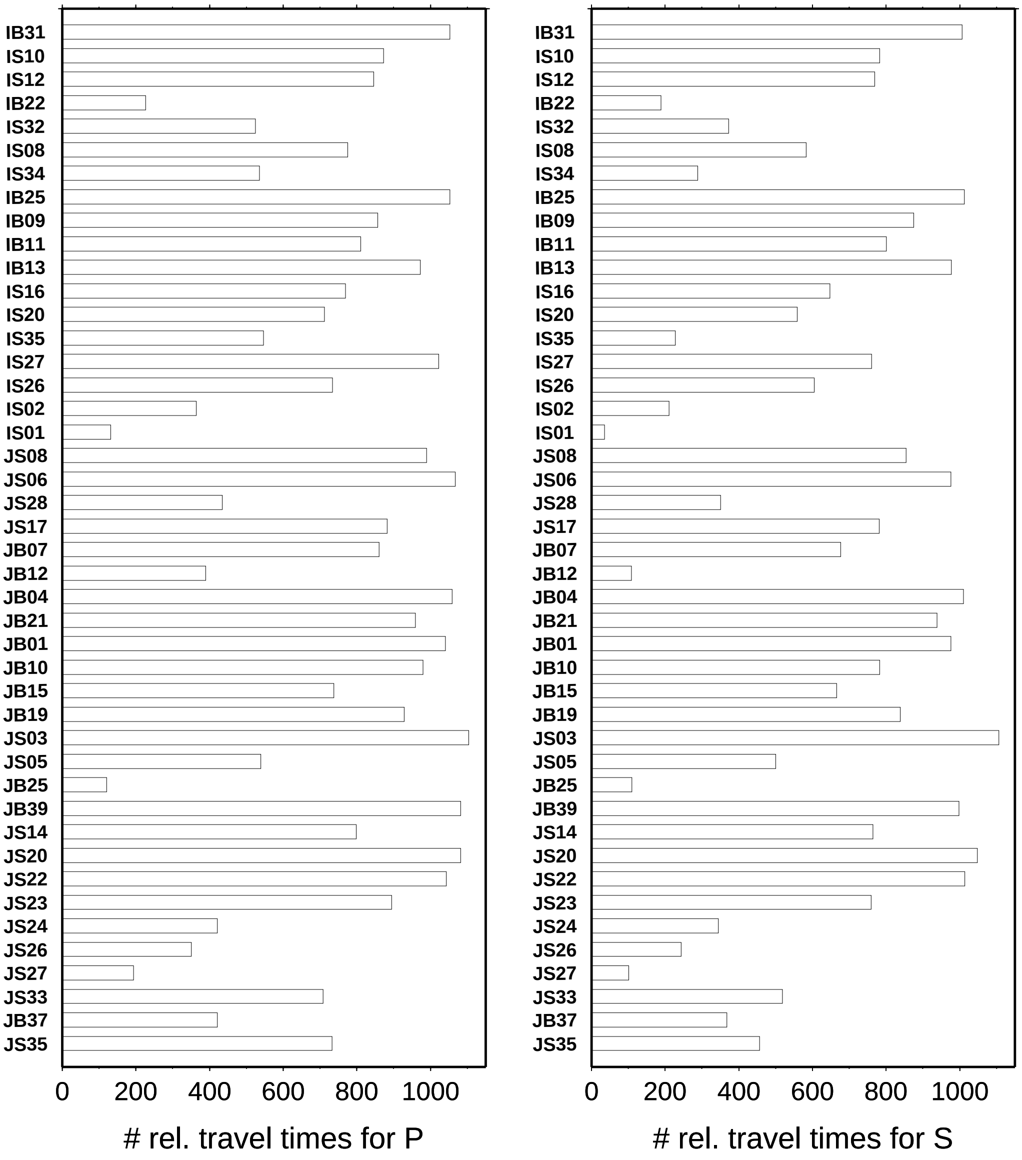

Figure 7.7: Number of differential P (left) and S (right) travel-times for each station for all events.

The maximum of $C(\tau)$ is achieved when τ is equivalent to the time delay between the two signals.

The cross correlation was done independently for P- and S-wave onsets. The dominating frequencies of the P- and the S-waves were 10 Hz and 8 Hz, respectively. Thus, the waveforms were bandpass filtered from 5 to 15 Hz for the P-wave onsets and from 3 to 13 Hz for the S-wave onsets. 3 sec of the waveforms were cut out from 1 sec before the manually picked P onsets. For the S onsets 4 sec were cut out, beginning 1 sec before the manually picked S onset (Figure 7.8). For each event pair and phase the cross correlation function was calculated from waveform samples recorded at a common station. The peak amplitude and time offset of the peak of the cross correlation function were determined (Figure 7.8). In the second step of HypoDD the time offsets of the cross correlation functions are added to the differential times determined by *ph2dt* while the peak amplitude is used as a weight of this cross correlation differential travel-time measurements. Cross-correlation times were retained only if the peak value of the cross correlation function was above 0.6 and 0.7 for the P onsets and the S onsets, respectively. In Figure 7.9 the distance of the event pairs is plotted versus the peak value of the cross correlation function (cc-value) for P onsets and S onsets, respectively. Apart from very few outliers, the maximum of the cc-values becomes smaller with increasing distance of event pairs and the number of achieved cc-values above the defined limits is also decreasing with increasing distance. To illustrate the cc-values of all events for a certain station "cross correlation matrixes" are prepared (Figure 7.10). The cc-value (if it is above the limit) is indicated as a dot whose size depends on the size of the cc-value. This illustration is normally used to depict event families (=clusters), characterized by similar source mechanism resulting in high peak amplitudes of the cross correlation function (e.g. Massa [2005]). Here, for stations with high quality data (e.g. JS20) for nearly all event pairs the cc-value exceeds the defined limit as all events belong to one cluster (Figure 7.10). Cross-correlation data quality of the S onsets is notably good, at some stations even better than the quality of the P onsets due to much larger amplitudes of the S waves compared to the P waves.

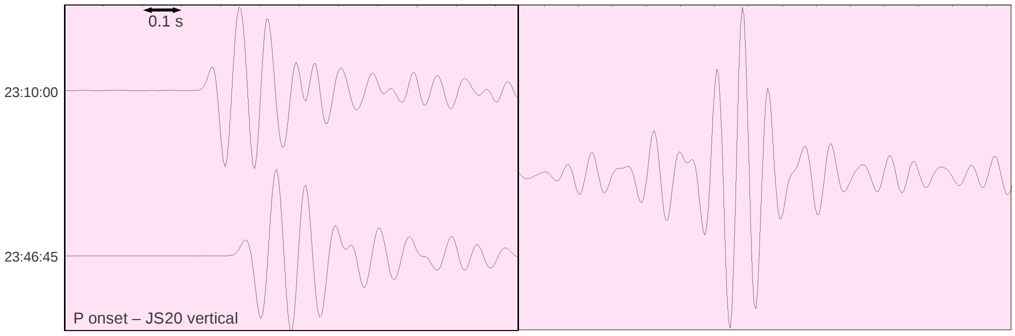

Figure 7.8: An illustration of waveform cross correlation of P onsets for two events on the 02/11/2007. The P onsets recorded on the vertical component at station JS20 are shown on the left. The cross-correlation function of the waveform pair is shown on the right. The time delay, determined by the cross correlation, is 0.095 sec.

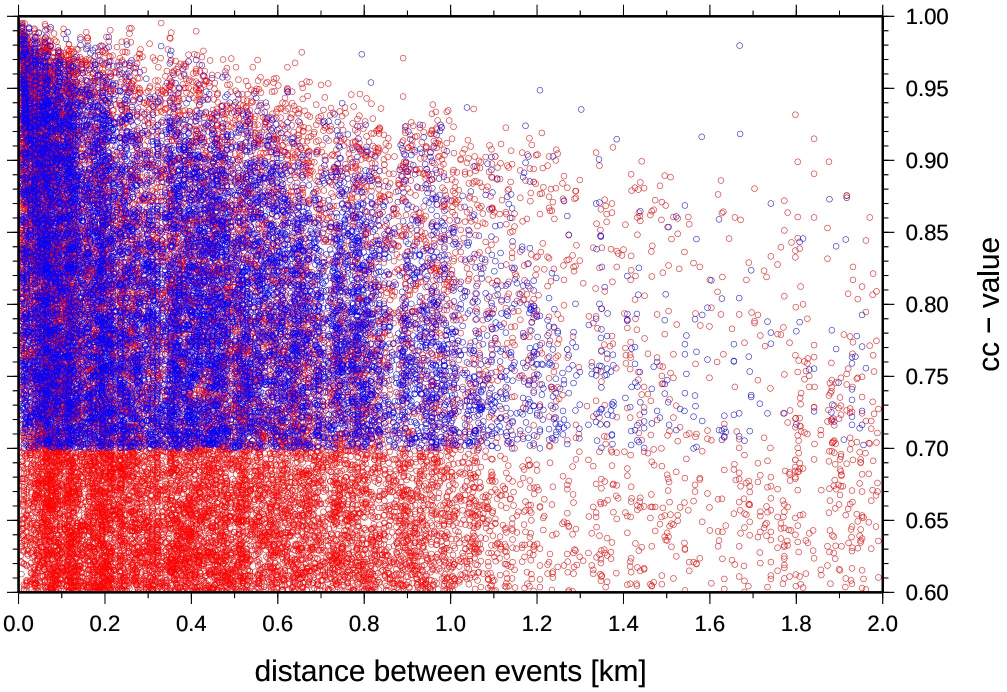

Figure 7.9: The distance of event pairs is plotted versus the peak values of the cross-correlation function. Red circles are indicating the values for the cross correlation of P onsets, blue circles are indicating the values for the cross correlation of the S onsets.

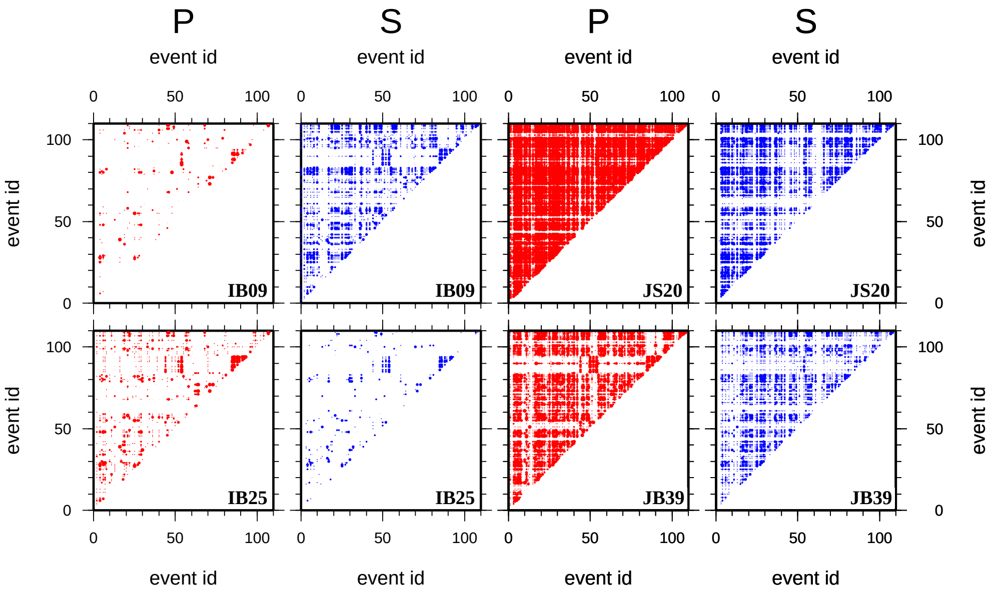

Figure 7.10: "Cross correlation matrixes" for different stations of P (red) and S (blue) onsets. For all event pairs the cc-value is indicated as a dot (whose size depends on the size of the cc-value) if the cc-value exceeds 0.6 or 0.7 for P or S onsets, respectively.

The differential times prepared by *ph2dt*, the selected events from *ph2dt* and the cc-values and time offsets of the cross correlation measurements are forming the input of the second step of HypoDD, realized by the program *hypoDD*. The crucial part of the relocation in *hypoDD* is the weighting and re-weighting of the data for the different iterations. The following parameters are therefore important to define.

`NITER`	Number of iterations.
`WTCCP,WTCCS`	Weight for cross correlation P-wave, S-wave data.
`WTCTP,WTCTS`	Weight for catalog P-wave, S-wave data.
`WRCC,WRCT`	Cutoff threshold for outliers located on the tail of the cc, catalog data. $0 - 1$ = absolute threshold in sec (static cutoff). ≥ 1 = factor to multiply standard deviation
`WDCC,WDCT`	Maximum event separation distance [km] for cc data, catalog data.

To control the interaction of these different parameters a weighting scheme is defined in the input file of *hypoDD* (Table 7.1). Waldhauser [2001] proposed that in the first iterations cross correlation data should be down-weighted in order to allow the catalog data to restore the large scale picture. In the next iterations weighting between catalog and cross-correlation data are kept fixed while cutoff thresholds for outliers and event separation are introduced in order to remove or down-weight outliers.

`NITER`	`WTCCP`	`WTCCS`	`WRCC`	`WDCC`	`WTCTP`	`WTCTS`	`WRCT`	`WDCT`
5	0.01	0.005	*	*	1.0	0.5	*	*
5	0.01	0.005	*	*	1.0	0.5	6	4
5	1.0	0.5	6	2	0.01	0.005	6	2
5	1.0	0.5	3	1	0.01	0.005	3	2
5	1.0	0.5	3	0.5	0.01	0.005	3	2

Table 7.1: Weighting scheme for the data used in hypoDD adopted from Waldhauser [2001]. For explanation see text.

In the following iterations the locations of events whose waveforms correlate by downweighting the catalog data relative to the cross-correlation data. The final iterations primarily use cross-correlation data of event pairs with little separation distance to resolve the small scale structure.

The result of the relocation leads to a mainly vertical structure of the cluster (Figure 7.11). 106 of the 112 events are relocated to a square of 1.1×1.1 km while the depth ranges from 12.9 to 15.9 km (Figure 7.12). A large part of the cluster is arranged in a vertical line from 13 to 15 km depth which is curved to the north (see depth - latitude section in Figure 7.11). To illustrate the relocation process in *hypoDD* Figure 7.13 show the location of four different events after each relocation step (Table 7.1). At each step the events are coming closer to their final location while the differences in-between the steps become smaller with each step (not always observable as only movements in two dimensions are visible). For two events the location after and before the last step are identical, certifying that the cross-correlation data of event pairs with little separation distance, used for the last step, resolves the small scale

structure.
The relatively small amount of data allows to use the SVD option in hypoDD, making direct access to the errors available. The largest RMS at one station is 397 msec for the last iteration of the last step of the inversion. The maximum average change in hypocentre location is found for the first iterations with 683 m while it is a few meters for the last iterations. The maximum absolute shift of the cluster centroid was 51 m. The complete logfile of *hypoDD* with all error values for each iteration is shown in Appendix C.
To test the reliability of the hypocentres determined by *hypoDD* jackknife tests were performed (Figure 7.14), i.e. subsets of different amounts of stations are selected randomly and used for the relocation procedure of a subset of 24 events. For different amount of stations (10, 20, 30) the process is repeated 100 times and the cumulative results (100×24 samples) are presented in Figure 7.14 in map view and in WE - depth sections. Ellipses in Figure 7.14 contain 95 % of the points.

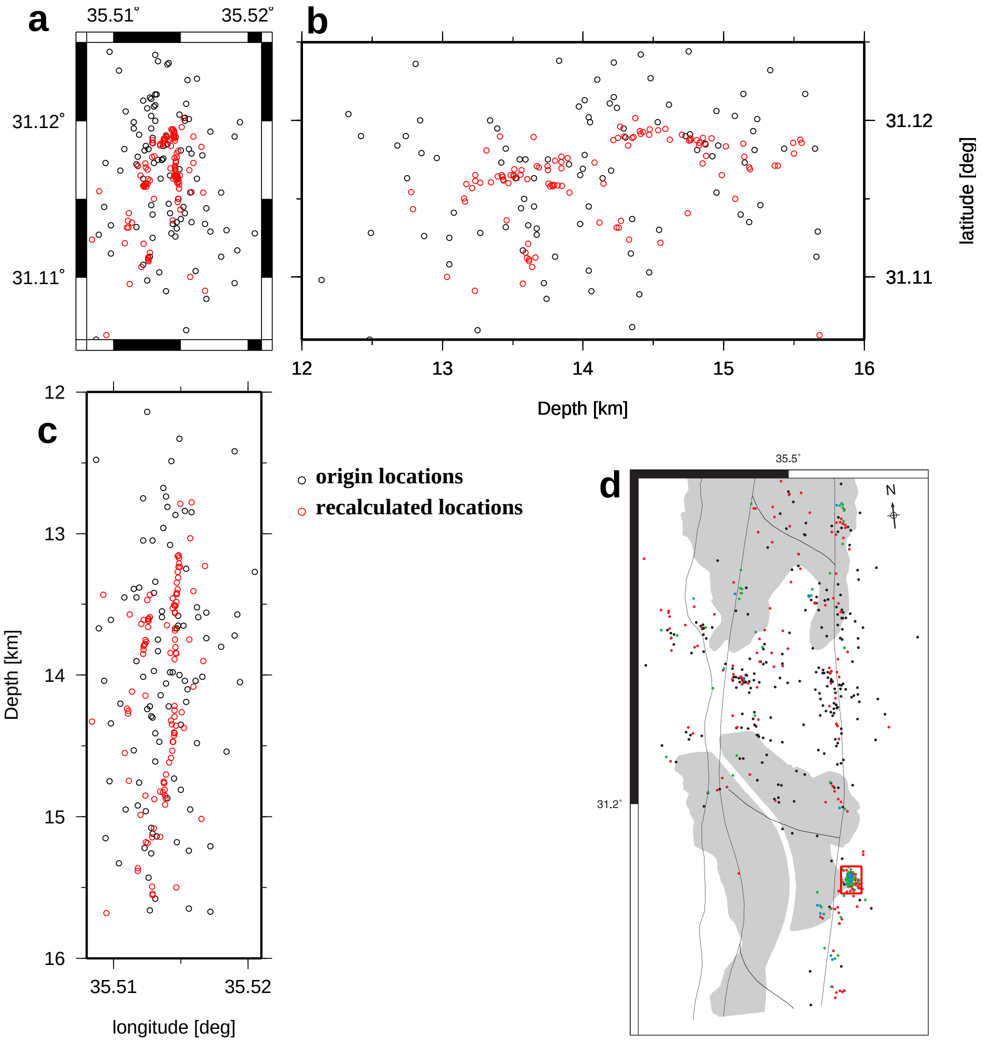

Figure 7.11: Original (black circles) and relocated (red circles) events in map view (a), depth - latitude (b) and longitude - depth (c). Map view of the whole study area from Figure 7.2 with the area of the cluster marked by a red square (d).

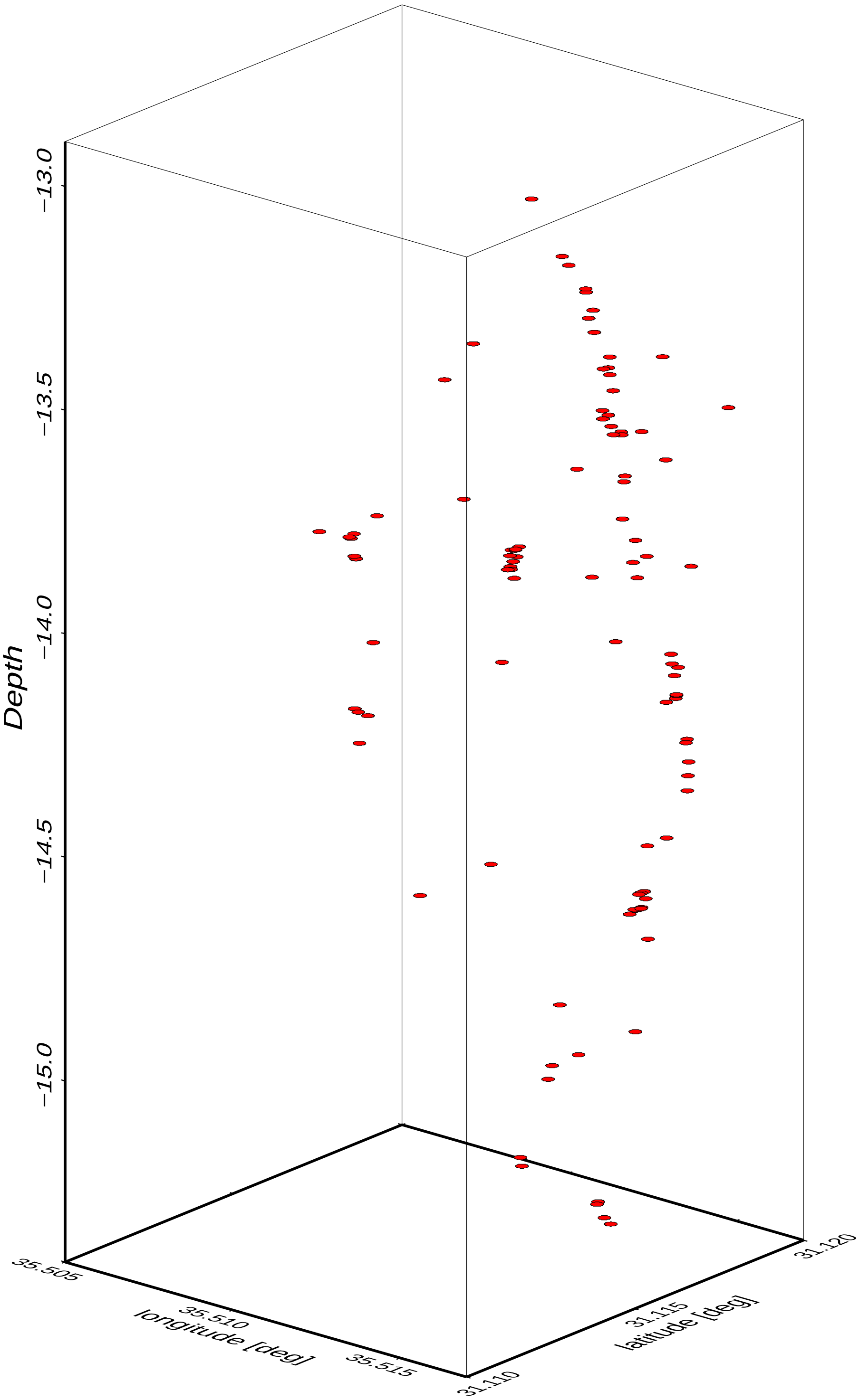

Figure 7.12: Three dimensional image of the cluster with events indicated as red dots.

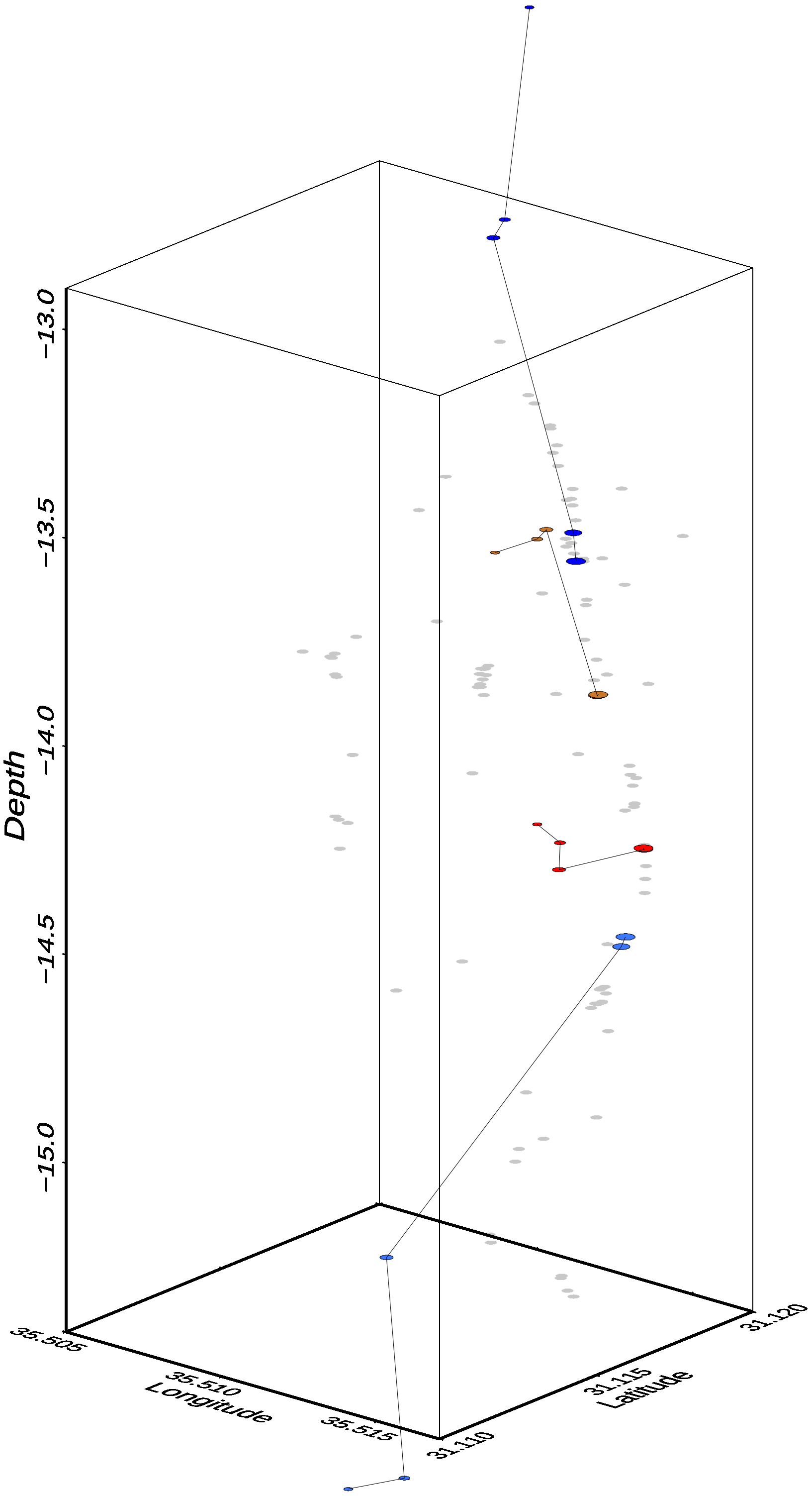

Figure 7.13: The location of 4 events (different colours) after each of the 5 steps of the *hypoDD* inversion (Table 7.1) indicated by coloured dots in different sizes (smallest = first step; biggest = last step). All relocated events indicated as grey are dots.

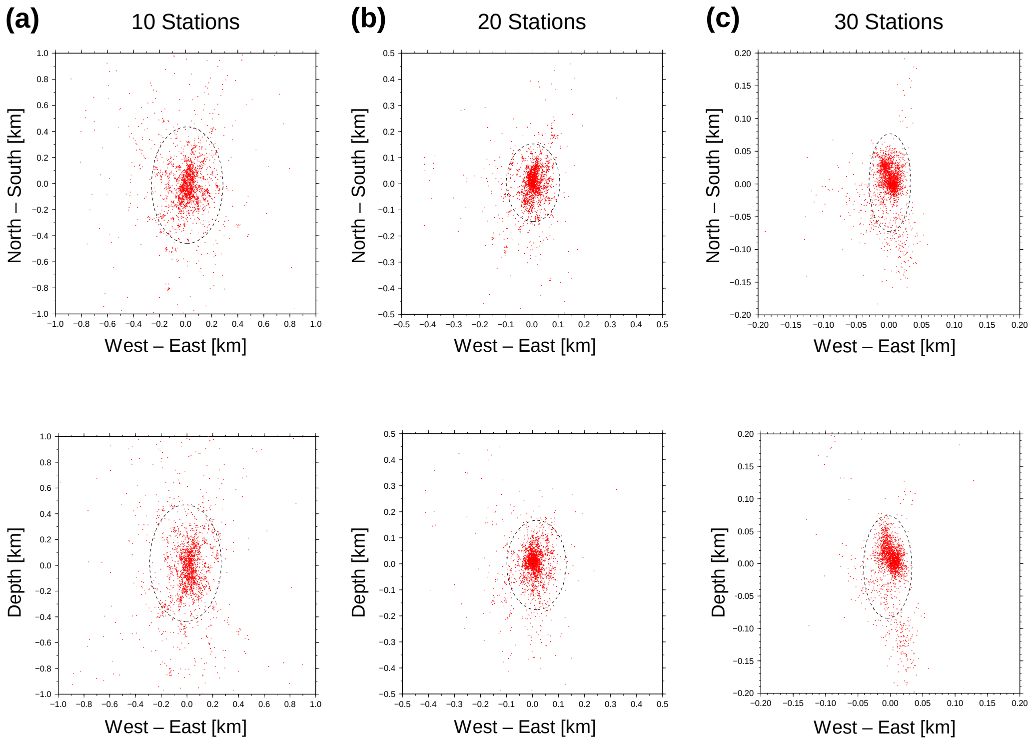

Figure 7.14: Misfit between original hypocentres and hypocentres determined with a subset of randomly chosen stations (10 (a), 20 (b), 30 (c)). In map view (top) and in WE - depth sections (bottom). The dashed ellipses contain 95 % of the relocations.

For the relocation with 10 stations the errors are typically less than about 400 m in depth and in NS direction while in WE direction it is typically less than 200 m. For the relocation with 30 stations the errors are typically less than about 50 m in depth and in NS direction while in WE direction it is typically less than 30 m. In average, onsets from 36 different stations are available for each event of the cluster. Thus, errors less than 50 m in depth and in NS direction and less than 30 m in WE direction are to be expected for the relocation.

An approach to verify that the cluster has a first order vertical structure is presented in Figure 7.15. For some high quality events in different depth, the waveforms are aligned to the P onsets. The waveforms are then displayed at their depth determined by HypoDD. With increasing depth the distance

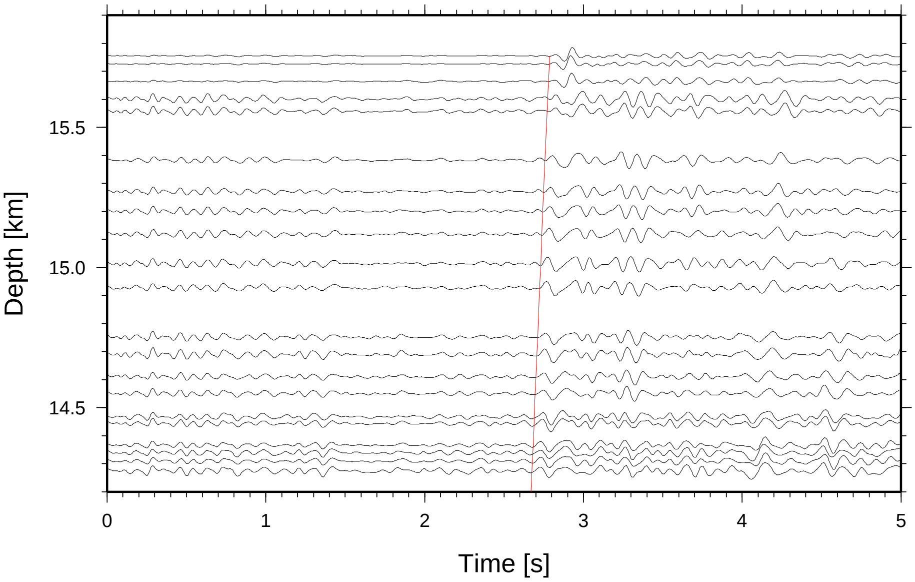

Figure 7.15: For station JS20 some high quality waveforms of different events, aligned to the P onset, are plotted versus depth. The red line is indicating the calculated S onset. Depth increases along the y - axis.

between P and S onset is increasing. Thus, the depth distribution of the relocated events seems not to be an artefact of the relocation procedure. The cluster shows hence a vertical structure perpendicular to the direction of the movement on the main faults (horizontally NS). A potential dependency between origin time and depth, indicating fluid induced seismicity was tested, but could not be confirmed.

7.3 Focal Mechanism

Focal mechanisms for 31 events were determined from first motion polarities using the computer program `FPFIT` (Fault Plane FIT, Reasenberg and Oppenheimer [1985]). This classical method uses first motion polarities (up and down) of P onsets, which are compared with the far field radiation pattern of a point source. `FPFIT` search for the double-couple fault plane solution that best fits a given set of observed first-motion polarities for an event. The inversion requires the estimated ray azimuth (seen from the source) from north and its inclination above horizontal (take-off angle measured from the source) for each first-motion polarity of an event. The solution of the inversion is achieved through a two-stage grid search procedure that search for the source model minimizing a normalized, weighted sum of first motion polarity discrepancies [Reasenberg and Oppenheimer, 1985].

Only events with at least 20 unambiguous polarities were considered for the calculation of focal mechanisms. It is interesting to note that reliable results were not achieved after the 1-D inversion, e.g. when using hypocentres, azimuth values and inclination values derived from the 1-D model. Only when the input parameters derived from the 3-D tomography model are incorporated, the resulting focal mechanisms are consistent and the inversion results are stable. The focal mechanism with the corresponding first-motion polarities are shown in Figure 7.16, 7.17 and 7.18.

22 of 31 events, where focal plane determination was possible, occurred at the eastern boundary fault (EBF, A and B in Figure 7.19). In the southeast of the study area, the largest events occurred and almost all events are showing strike-slip mechanism (A in Figure 7.19) with fault planes oriented WE and NS, reflecting the regional stress regime (see Section 2). In the northeast (B in Figure 7.19) some smaller events occurred showing strike-slip mechanisms, WE oriented normal faulting character, or a mixture of both. Most of the events at the WF (C in Figure 7.19) exhibit normal fault solutions while also strike slip and thrust type characteristics are observed.

All but one event south of 31.15°N show clear strike slip mechanisms with fault planes oriented WE and NS, reflecting the regional stress regime (Figure 7.20). In contrast, north of 31.15°N different mechanisms are observed, irrespective whether they are in the upper crust (B) or in the lower crust (C). Most of these events show normal faulting, mainly oriented WE, but strike slip mechanisms are also observed. Furthermore, the highest magnitudes archived by events in the north is one magnitude smaller than the largest events south of 31.15°N. Thus, the events north 31.15°N are perhaps related to secondary faults as the majority is not reflecting the regional stress regime.

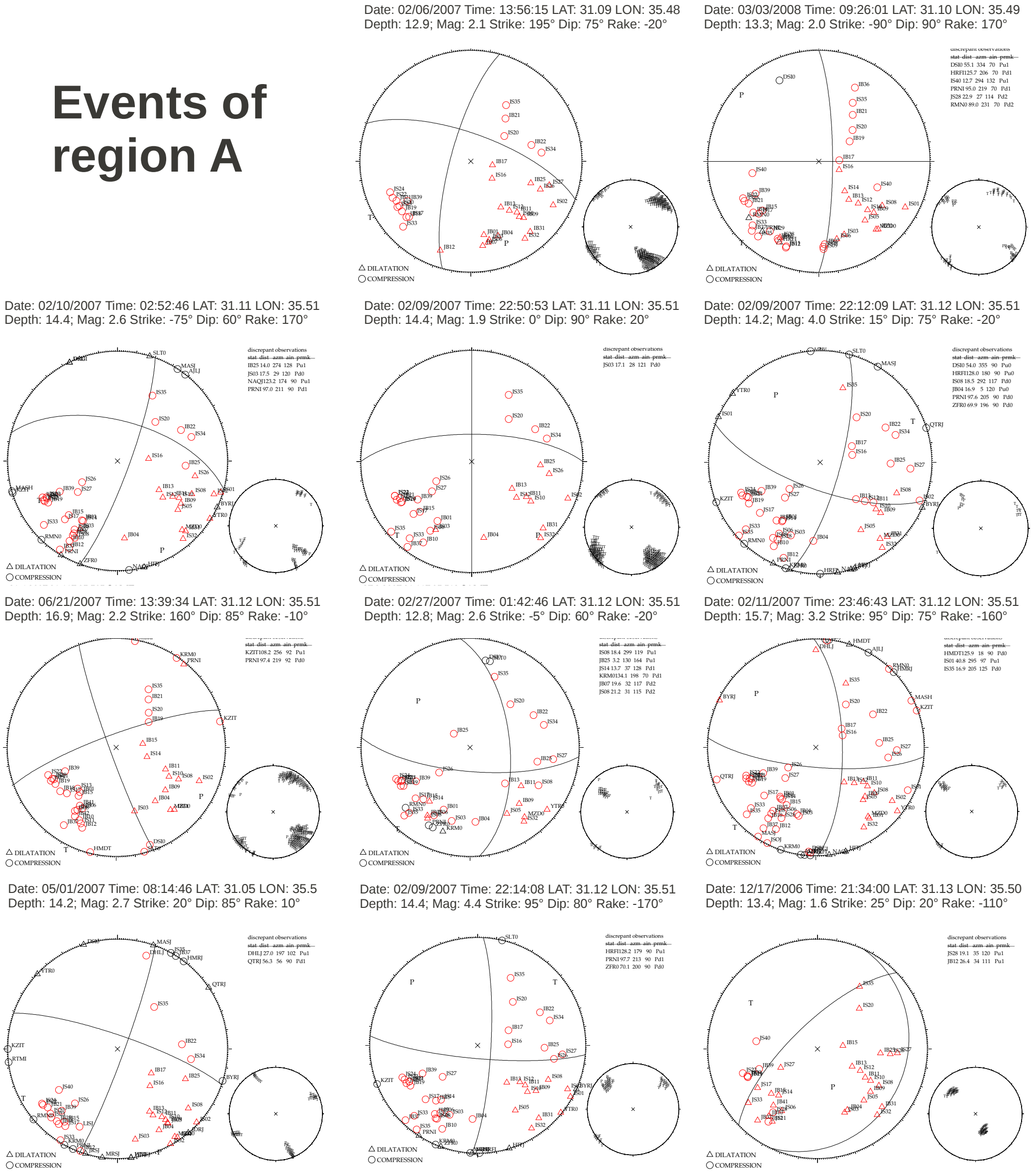

Date: 02/06/2007 Time: 13:56:15 LAT: 31.09 LON: 35.48
Depth: 12.9; Mag: 2.1 Strike: 195° Dip: 75° Rake: -20°

Date: 03/03/2008 Time: 09:26:01 LAT: 31.10 LON: 35.49
Depth: 13.3; Mag: 2.0 Strike: -90° Dip: 90° Rake: 170°

Date: 02/10/2007 Time: 02:52:46 LAT: 31.11 LON: 35.51
Depth: 14.4; Mag: 2.6 Strike: -75° Dip: 60° Rake: 170°

Date: 02/09/2007 Time: 22:50:53 LAT: 31.11 LON: 35.51
Depth: 14.4; Mag: 1.9 Strike: 0° Dip: 90° Rake: 20°

Date: 02/09/2007 Time: 22:12:09 LAT: 31.12 LON: 35.51
Depth: 14.2; Mag: 4.0 Strike: 15° Dip: 75° Rake: -20°

Date: 06/21/2007 Time: 13:39:34 LAT: 31.12 LON: 35.51
Depth: 16.9; Mag: 2.2 Strike: 160° Dip: 85° Rake: -10°

Date: 02/27/2007 Time: 01:42:46 LAT: 31.12 LON: 35.51
Depth: 12.8; Mag: 2.6 Strike: -5° Dip: 60° Rake: -20°

Date: 02/11/2007 Time: 23:46:43 LAT: 31.12 LON: 35.51
Depth: 15.7; Mag: 3.2 Strike: 95° Dip: 75° Rake: -160°

Date: 05/01/2007 Time: 08:14:46 LAT: 31.05 LON: 35.5
Depth: 14.2; Mag: 2.7 Strike: 20° Dip: 85° Rake: 10°

Date: 02/09/2007 Time: 22:14:08 LAT: 31.12 LON: 35.51
Depth: 14.4; Mag: 4.4 Strike: 95° Dip: 80° Rake: -170°

Date: 12/17/2006 Time: 21:34:00 LAT: 31.13 LON: 35.50
Depth: 13.4; Mag: 1.6 Strike: 25° Dip: 20° Rake: -110°

Figure 7.16: Fault plane solutions for region A in Figure 7.19 and Figure 7.20 labeled with date, time, latitude, longitude, depth, magnitude, strike, dip, rake. Stations with discrepant observation are specified, never exceeding 15 % of all observations.

Events of region A

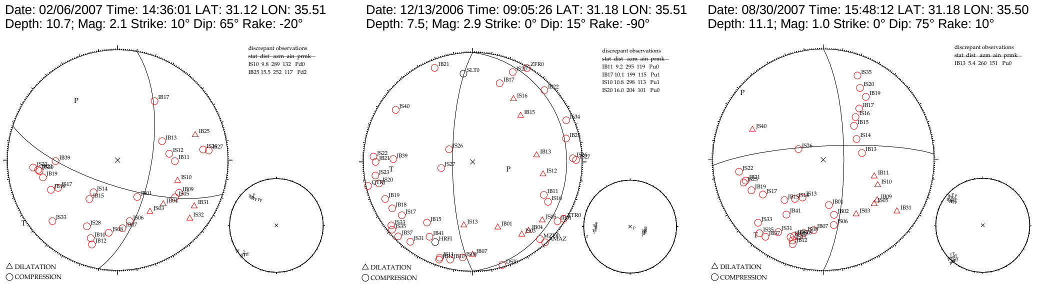

Date: 02/06/2007 Time: 14:36:01 LAT: 31.12 LON: 35.51
Depth: 10.7; Mag: 2.1 Strike: 10° Dip: 65° Rake: -20°

discrepant observations

stat	dist	azm	ain	prmk
IS10	9.8	289	132	Pd0
IB25	15.5	252	117	Pd2

Date: 12/13/2006 Time: 09:05:26 LAT: 31.18 LON: 35.51
Depth: 7.5; Mag: 2.9 Strike: 0° Dip: 15° Rake: -90°

discrepant observations

stat	dist	azm	ain	prmk
IB11	9.2	295	119	Pu0
IB17	10.1	199	115	Pu1
IS10	10.8	298	113	Pu1
IS20	16.0	204	101	Pu0

Date: 08/30/2007 Time: 15:48:12 LAT: 31.18 LON: 35.50
Depth: 11.1; Mag: 1.0 Strike: 0° Dip: 75° Rake: 10°

discrepant observations

stat	dist	azm	ain	prmk
IB13	5.4	260	151	Pu0

Events of region B

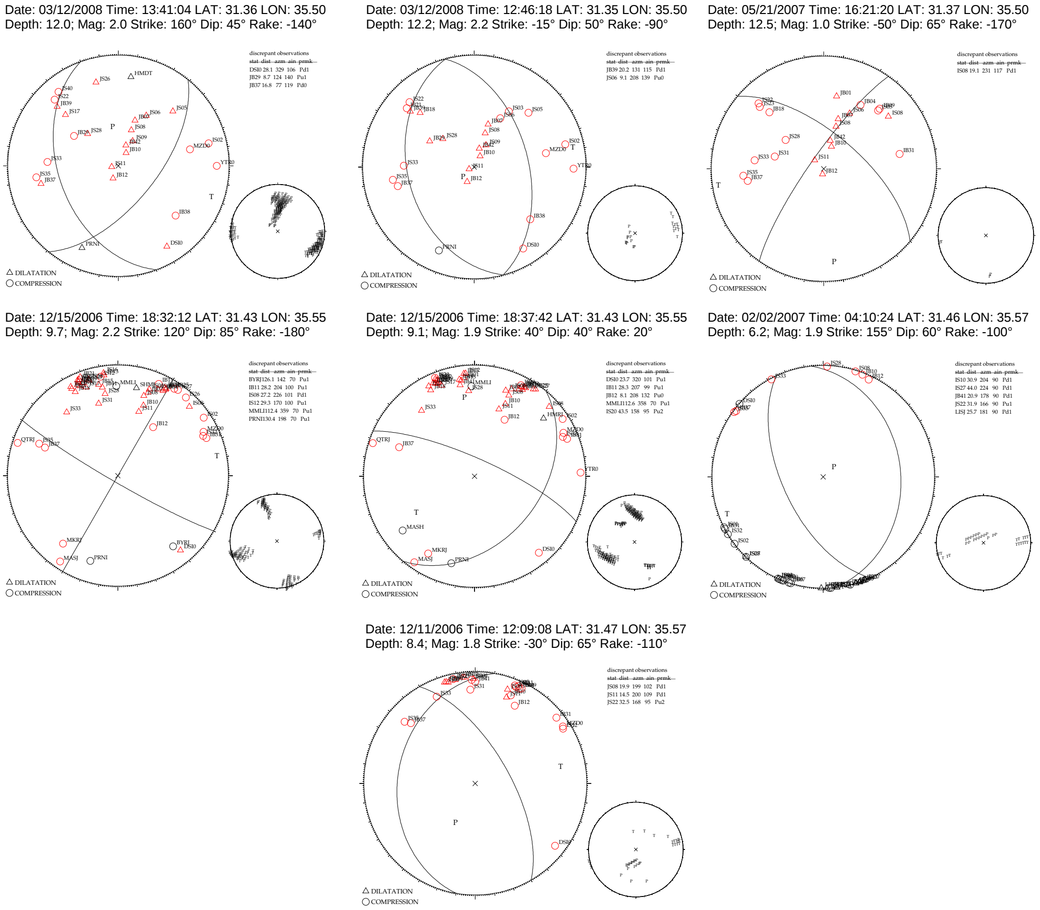

Date: 03/12/2008 Time: 13:41:04 LAT: 31.36 LON: 35.50
Depth: 12.0; Mag: 2.0 Strike: 160° Dip: 45° Rake: -140°

discrepant observations

stat	dist	azm	ain	prmk
DSI0	28.1	329	106	Pd1
JB29	8.7	124	140	Pu1
JB37	16.8	77	119	Pd0

Date: 03/12/2008 Time: 12:46:18 LAT: 31.35 LON: 35.50
Depth: 12.2; Mag: 2.2 Strike: -15° Dip: 50° Rake: -90°

discrepant observations

stat	dist	azm	ain	prmk
JB39	20.2	131	115	Pd1
JS06	9.1	208	139	Pu0

Date: 05/21/2007 Time: 16:21:20 LAT: 31.37 LON: 35.50
Depth: 12.5; Mag: 1.0 Strike: -50° Dip: 65° Rake: -170°

discrepant observations

stat	dist	azm	ain	prmk
IS08	19.1	231	117	Pd1

Date: 12/15/2006 Time: 18:32:12 LAT: 31.43 LON: 35.55
Depth: 9.7; Mag: 2.2 Strike: 120° Dip: 85° Rake: -180°

discrepant observations

stat	dist	azm	ain	prmk
BYRJ	126.1	142	70	Pu1
IB11	28.2	204	100	Pu1
IS08	27.2	226	101	Pd1
IS12	29.3	170	100	Pu1
MMLI	112.4	359	70	Pu1
PRNI	130.4	198	70	Pu1

Date: 12/15/2006 Time: 18:37:42 LAT: 31.43 LON: 35.55
Depth: 9.1; Mag: 1.9 Strike: 40° Dip: 40° Rake: 20°

discrepant observations

stat	dist	azm	ain	prmk
DSI0	23.7	320	101	Pu1
IB11	28.3	207	99	Pu1
JB12	8.1	208	132	Pu0
MMLI	112.6	358	70	Pu1
IS20	43.5	158	95	Pu2

Date: 02/02/2007 Time: 04:10:24 LAT: 31.46 LON: 35.57
Depth: 6.2; Mag: 1.9 Strike: 155° Dip: 60° Rake: -100°

discrepant observations

stat	dist	azm	ain	prmk
IS10	30.9	204	90	Pd1
IS27	44.0	224	90	Pd1
JB41	20.9	178	90	Pd1
JS22	31.9	166	90	Pu1
LISJ	25.7	181	90	Pd1

Date: 12/11/2006 Time: 12:09:08 LAT: 31.47 LON: 35.57
Depth: 8.4; Mag: 1.8 Strike: -30° Dip: 65° Rake: -110°

discrepant observations

stat	dist	azm	ain	prmk
JS08	19.9	199	102	Pd1
JS11	14.5	200	109	Pd1
JS22	32.5	168	95	Pu2

Figure 7.17: Fault plane solutions for region A and B in Figure 7.19 and Figure 7.20 labeled with date, time, latitude, longitude, depth, magnitude, strike, dip, rake. Stations with discrepant observation are specified, never exceeding 15 % of all observations.

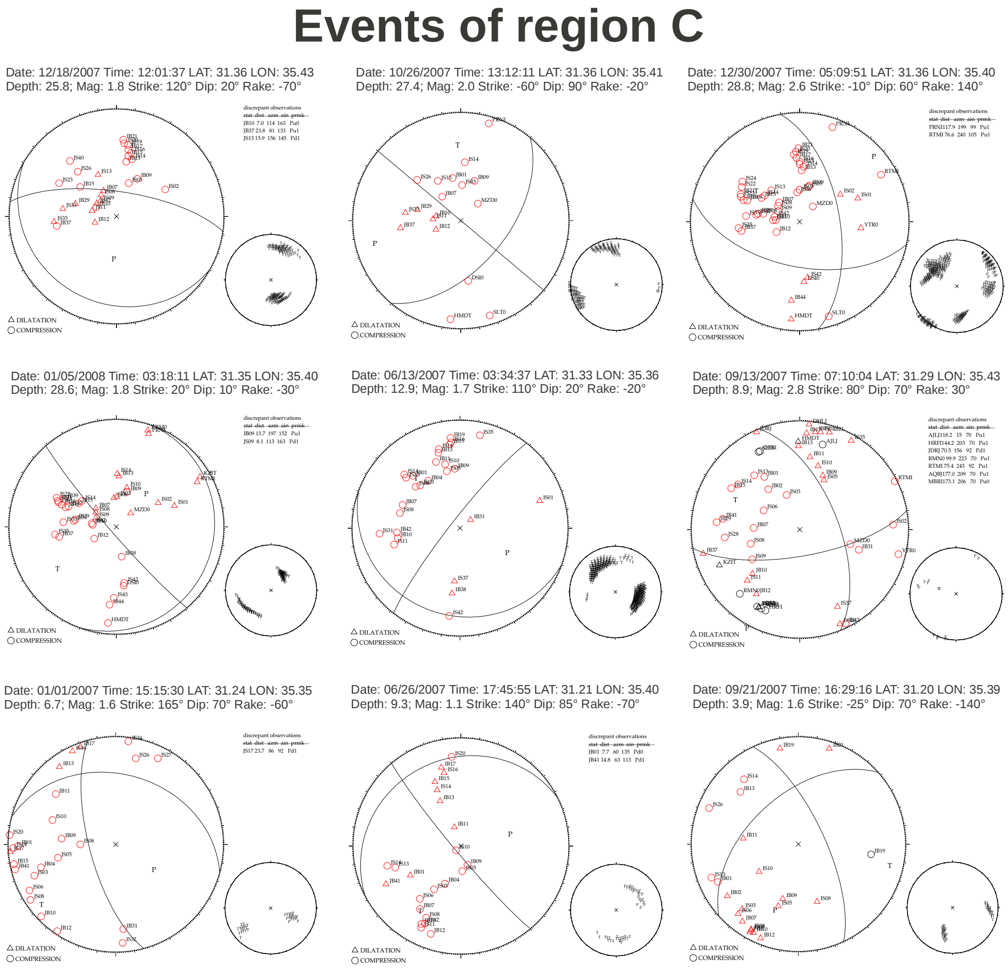

Figure 7.18: Fault plane solutions for region C in Figure 7.19 and Figure 7.20 labeled with date, time, latitude, longitude, depth, magnitude, strike, dip, rake. Stations with discrepant observation are specified, never exceeding 15 % of all observations.

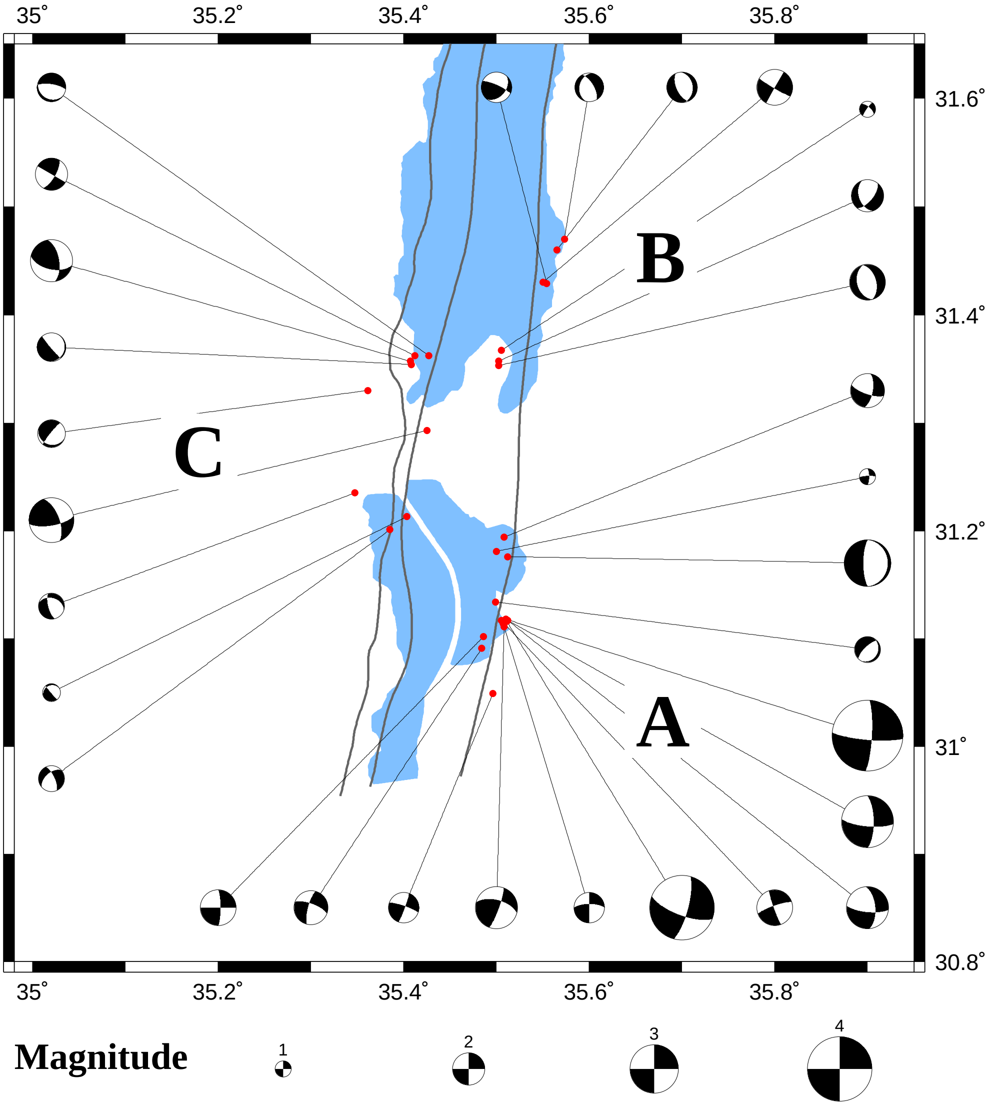

Figure 7.19: Location of fault plane solutions indicated as red dots. Grey lines are mapping the main faults. The areas which are covered with water recently are marked in blue. A: Events at the southern part of the EBF. B: Events at the northern part of the EBF. C: Events at the WF.

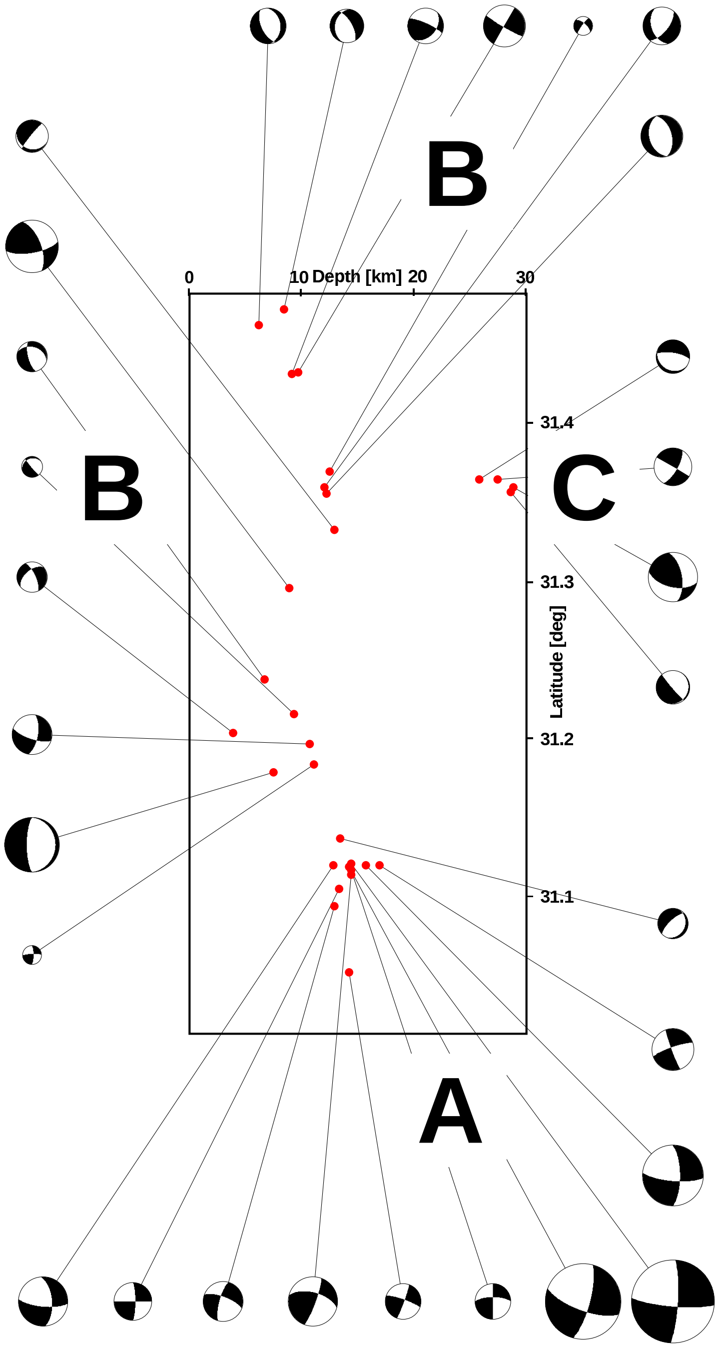

Figure 7.20: Location of fault plane solutions indicated as red dots in a depth - latitude section. Magnitude scaling of the symbols like in Figure 7.19. A: Events south of 31.15°N. B: Events in the upper crust north of 31.15°N. C: Events in the lower crust north of 31.5°N.

Chapter 8

Discussion

8.1 Seismicity

Seismicity occurs from 2 km depth down to depth of 29 km, confirming results of Aldersons et al. [2003]. Thus, an approximately 30 km thick brittle layer can be approved which agrees furthermore with the Moho depth of about 32 km revealed from e.g. wide-angle seismic data [Mechie et al., 2009].

Figure 8.1 shows the hypocentre location results of the minimum 1-D model compared to the locations for the 2-D and the 3-D tomography. The difference between the velocities in the 1-D model and the tomographic models of up to +/- 30 % results in relatively large location discrepancy (up to 6 km, Figure 8.1) between the 1-D relocation and the tomographic inversion relocation. However, the location differences between the 2-D and the 3-D inversion are significantly smaller (mostly below 1 km, Figure 8.1). Reliable results for the determination of the focal mechanisms were only obtained after including the hypocentre locations of a tomographic model. Thus, it can be concluded that for accurate determination of hypocenters and/or focal mechanisms in the study area, event locations revealed through a tomographic inversion (2-D or 3-D) are necessary.

The distribution of the seismicity is presented in detail in Figure 8.2, including a classification in three regions of different seismic activity (A, B, C). In the south of the investigation area (south of 31.13°N, A in Figure 8.2)

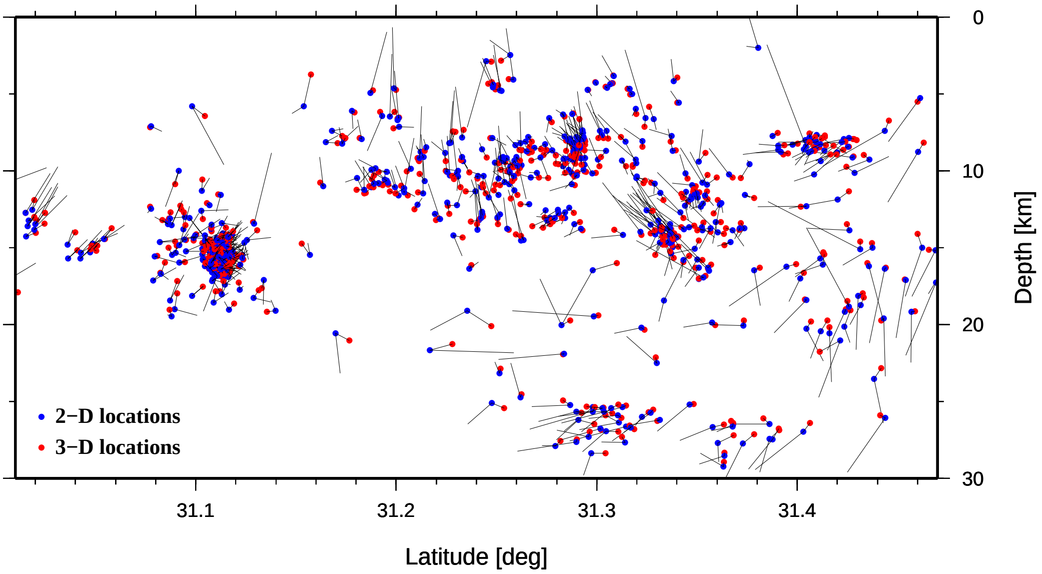

Figure 8.1: Latitude - depth section with vectors indicating the shift in hypocentre location after the tomographic v_P and v_P/v_S inversions (indicated by circles) relative to hypocentre location obtained with the 1D model.

the seismic activity is solely related to the eastern boundary fault (EBF). These events, including the largest events in the area during the time of the investigation, occur mainly between 13 and 17 km depth. The spatial and temporal cluster from February 2007 occurred right at the transition to a seismically inactive region (GAP in Figure 8.2) north of 31.13°N. The vertical extension of the cluster is probably related to the locking of the region north of it, while the focal mechanisms of its largest events represent the general NS transform motion as well as the focal mechanisms of other events south of 31.13°N (A in Figure 8.2). Thus, the events in the south reflect the ongoing movement of the Arabian plate to the north. This is verified by GPS measurements on different locations on the Arabian plate [Klotz, personal comm.]. The western faults (WF) show no seismicity in the south during the time of the investigation, which confirms the stable position of the African plate relative to the Arabian plate close to the study area [Klotz, personal comm.].

The seismically inactive region extends from 31.13°N to 31.17°N where shallow activity (5-12 km depth) starts on both boundaries (B in Figure

8.2). This change in the seismic behaviour can be associated with the transverse Boqeq fault (BOF in Figure 8.2). The lower boundary of the seismic activity in the upper crust (above 20 km depth after Mechie et al. [2009]) decreases between 31.17°N and 31.4°N from 12 to 17 km depth (Figure 8.2b). It is important to note that this pattern of the seismicity distribution between 31.17°N and 31.4°N is similar for both boundaries (EBF, WF). Furthermore, events at both boundaries show normal faulting, mainly WE extension and strike slip characteristics, indicating NS horizontal and WE extensional motion (B in Figure 8.2). Farther north the depth ranges of seismic activity are again different at each boundary fault (EBF: 7-10 km; WF: 13-20 km). This change in the seismic behaviour can be associated with the transverse Ein Gedi fault (EGF in Figure 8.2).

A similar seismicity distribution pattern was found by van Eck and Hofstetter [1989] for a 20 month period of investigation between 1986 and 1988: Strong activity around 31.12°N only at the EBF (including a cluster) with strike-slip mechanisms, a gap of seismicity farther north, and activity on both boundary faults north of 31.16°N. Thus, this pattern can be assumed to be constant over a longer period. An important change in the seismic behaviour of the boundary faults in the study area can thus be stated between the region south of 31.13°N and the region north of 31.17°N, divided by the transverse Boqeq fault. In the south mid-crustal strike-slip events related to the eastern boundary fault are representing the general transform motion along the Dead Sea transform fault. This motion is locked north of 31.13°N until 31.17°N. The region north of 31.17°N represents the expected transfer of the motion in pull-apart basins from the eastern border to the western border, indicated by similar activity on the boundary faults.

The seismic activity in the lower crust is limited to the region north of 31.25°N between 25 and 29 km depth (C in Figure 8.2). These events seem not to be related to the fault system of the sedimentary basin. This is consistent with the assumption of Mechie et al. [2009] that the boundary between the upper and the lower crust at 20 km depth act as a decoupling zone. While activity at this depth is known also from Aldersons et al. [2003], the limited activity does not allow further interpretations.

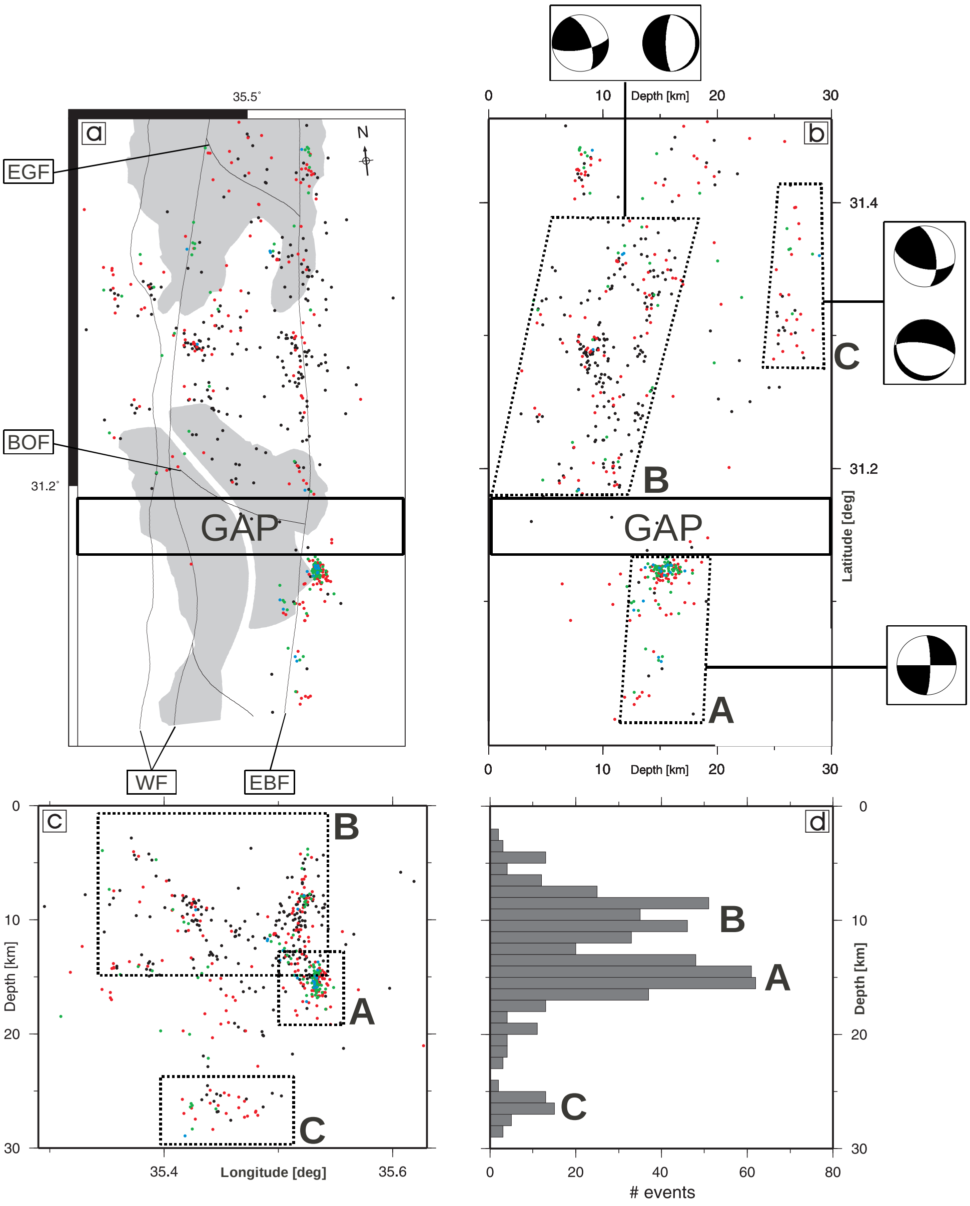

Figure 8.2: Map view of the study area with the events, marked as dots in different colours, scaled by its magnitude like in Figure 7.2 (a). The main faults are indicated as thin black lines. EBF: Eastern boundary fault, WF: Western faults, BOF: Boqeq fault, EGF: Ein Gedi fault. The three main regions of different seismic activity A, B and C marked in a depth - latitude section (b), a longitude - depth section (c) and a depth histogram (d). For each different seismic region one or two characteristic focal mechanism are indicated. For explanation see text.

8.2 Tomography

Certain features of the v_P model and the model of v_P/v_S ratios are similar, though some important differences between them exist. Both 2-D models show a similar structure for the uppermost 8 km (Figure 8.3) and also the WE - depth sections of the 3-D model is similar for both models (WE1, WE2 in Figure 8.4). The sedimentary basin is clearly imaged through low P velocities and high v_P/v_S ratios. The eastern boundary of the sedimentary body is vertical while the western boundary is inclined to the east. Thus, an asymmetric structure of the sedimentary basin is revealed through both models, confirming former investigations [Neev and Hall, 1979, Zak and Freund, 1981, ten Brink et al., 1993, Garfunkel and Ben-Avraham, 1996, Garfunkel, 1997].

The Lisan salt diapir below the Lisan peninsula is imaged through v_P/v_S ratios below the average of 1.74 (Figure 8.5) while the v_P model show no features in this area. In magnetotelluric measurements the salt body is characterized by very high resistivity, indicating the absence of fluids necessary for electric conductivity [Meqbel, 2009]. The diapir extends from the eastern boundary about 12 km to the west. The Pleistocene sediments farther west of the diapir contain significant amount of fluids indicated by very low resistivity [Meqbel, 2009] and high v_P/v_S ratios (Figure 8.5). The maximal NS elongation of the diapir is estimated to about 17 km while the lower limit of the salt body is reached at depths between 5 and 6 km (NS1 in Figure 8.4). These values are in good agreement with estimations based on gravity measurements from Choi et al. [2011] who suggested a size of 10×20 km and a depth of about 6 km while Al-Zoubi and ten Brink [2001] revealed from seismic reflection data a size of 10×13 km and a depth of 7 km. Choi et al. [2011] suggested another prominent salt body north of the Lisan diapir which is not imaged through the model of v_P/v_S ratios (Figure 8.5). The Sedom diapir below the Mount Sedom in the southwest of the study area could not be identified (Figure 8.5). Probable reasons for this are its small size (width 1 - 1.5 km, depth $\sim$2 km from Al-Zoubi et al. [2002]) and the lack of resolution due to the absence of seismic activity in the southwest of

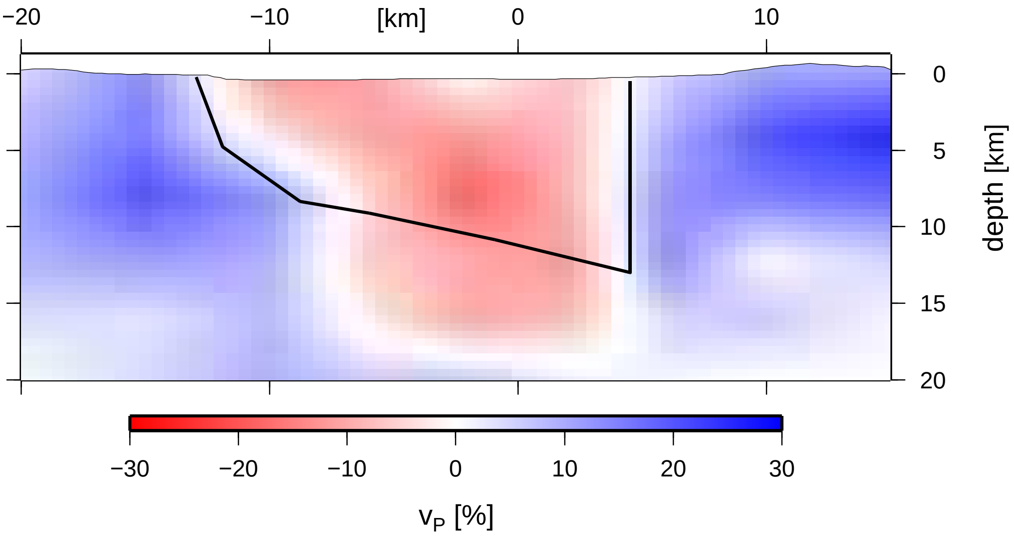

Figure 8.3: 2-D tomographic v_P model perpendicular to the main boundary faults displayed as deviations from the 1-D starting model. The transition between low and high v_P/v_S ratios is indicated by the black contour line representing the average value of $v_P/v_S = 1.74$.

the study area and its location close to the surface.

A significant difference between the v_P model and the model of v_P/v_S ratios appears in the lower part of the sedimentary basin (depth > 8 km, Figure 8.3 and 8.4). The low v_P body forms a nearly horizontal lower boundary of about 10 km width (also assumed from modelling of gravity data by ten Brink et al. [1993]) and extends to a depth of about 17 km (Figure 8.3). While ten Brink et al. [1993] estimated a maximum thickness of 16 km from gravity modelling, later studies based on gravity data proposed 14 km of maximum thickness of the basin [Ben-Avraham and Lazar, 2006, Choi et al., 2011]. A wide angle reflection/refraction profile crossing the basin approximately from north to south revealed about 8 km depth for the northern basin and about 14 km below the Lisan peninsula with an abrupt change in-between (GB97 in Figure 8.4 from Ginzburg and Ben-Avraham [1997]).

The region of high v_P/v_S ratios extends to depth between 10 and 14 km (NS1, NS2 in Figure 8.4). Thus, the lower part of the sediment fill contains few to no fluids, resulting in v_P/v_S ratios not discernible from crystalline basement rocks (1.73 and below). The sediments deposited during the basin subsidence (younger than ∼17 Ma) are of fluviatile, lacustrine and marine origin [Garfunkel, 1997, Garfunkel and Ben-Avraham, 2001]. Except for salt, these sediments are thus expected to have a significant fluid content. Hence, the lowest sediment layer characterized by low P velocities but low v_P/v_S ratios is most probably made of Cretaceous and pre-Cretaceous sediments deposited before the formation of the DSB (e.g. Ben-Avraham and Schubert [2006]). From studies based on gravity data the thickness of these pre-basin sediments is assumed to be 7 km [ten Brink et al., 1993], 3 km [Al-Zoubi et al., 2002], 4 km [Ben-Avraham and Schubert, 2006] or 5 km Choi et al. [2011]. From a WE trending WRR profile only about 2 km thickness are revealed [Mechie et al., 2009], taking into account the thickness of the same units outside the basin and the stretching of the crust within the basin. A possibility to explain these varying results are significant changes of the pre-basin sediment thicknesses in different regions (NS1 and NS2 in Figure 8.4). While the lower boundary of the low v_P body is at ∼17 km depth within the entire study area, the depth of the lower boundary of the fluid containing basin sediments varies between about 10 and 14 km from profile km -15 to km 5 in the profile NS1 in Figure 8.4. Thus, the region of low v_P/v_S ratios and low P velocities varies between 7 and 3 km. As the pre-basin sediments outside the DSB are only maximum 3 km thick (e.g. Garfunkel [1997], Mechie et al. [2009]) this layer cannot be solely explained by pre-basin sediments. More likely, the pre-basin sediments are about 3 km thick on average, while below it, the P velocity of the crust is most likely reduced due to mechanical reworking during the stretching process of the crust (Figure 8.4, [Sobolev, Garfunkel personal comm.]).

The division of the upper crustal earthquakes in events south of 31.13°N and events north of 31.17°N due to the differences in their mechanisms and their distribution at the boundary faults (Section 7.1/8.1) is in good agreement with the tomography results (Figure 8.4). South of the 31.13°N the earthquakes occur at the eastern boundary of the low v_P body. However, these events are located below the limit of the region of high v_P/v_S ratios, thus significant fluid content is not necessary for their presence. This furthermore explains the lack of fluid activity related to the cluster which occurred in February 2007 (discussed in Section 7.2). In contrast, the upper crustal events north of 31.17°N occur in areas of high v_P/v_S ratios and especially at the boundary between high and low v_P/v_S ratios (Figure 8.4). Thus, the events north of 31.17°N occur preferably in fluid containing environments. The increasing depth of the lower boundary of the upper crustal activity from 12 km at 31.17°N to about 17 km at 31.4°N (Figure 8.2) can be assigned to the change in v_P/v_S ratios from profile km -15 to km 5 in the profiles NS1 and NS2 in Figure 8.4. In profile NS2 in Figure 8.4 the lower boundary of the basin and the boundary between pre-basin and basin sediments seems to roughly fit with the same boundaries in the WRR profile of Ginzburg and Ben-Avraham [1997] (GB97 in Figure 8.4). However, the apruptly decreasing depth of the lower boundary of the basin towards the north in the WRR profile cannot be confirmed by the tomographic results (NS2, GB97 in Figure 8.4).

Figure 8.6 shows two schemes where the tomographic results are brought together with results from previous studies (e.g. Garfunkel [1997], Al-Zoubi et al. [2002], Ben-Avraham and Schubert [2006], Mechie et al. [2009], Choi et al. [2011]). The transverse Boqeq and Ein Gedi faults are not influencing the lower boundary of the basin. Both faults are bordering regions of different seismic regime (Figure 8.2): South of the Boqeq fault and north of the Ein Gedi fault the character of the seismicity at each boundary is different. Between the Boqeq and the Ein Gedi faults the seismic behaviour is similar at the boundary faults (WF and EBF in Figure 8.6). While both transverse faults are south facing normal faults, they show different amounts of faulting, resulting in a tilted lower boundary of the basin sediments (Miocene to recent) mapped by the v_P/v_S ratio distribution and the seismic events (NS1 and NS2 in Figure 8.4). The WE profile (Figure 8.6b) shows the inclined western boundary and the vertical eastern boundary of the basin, thus the Dead Sea basin is an asymmetric basin, at least in the study area.

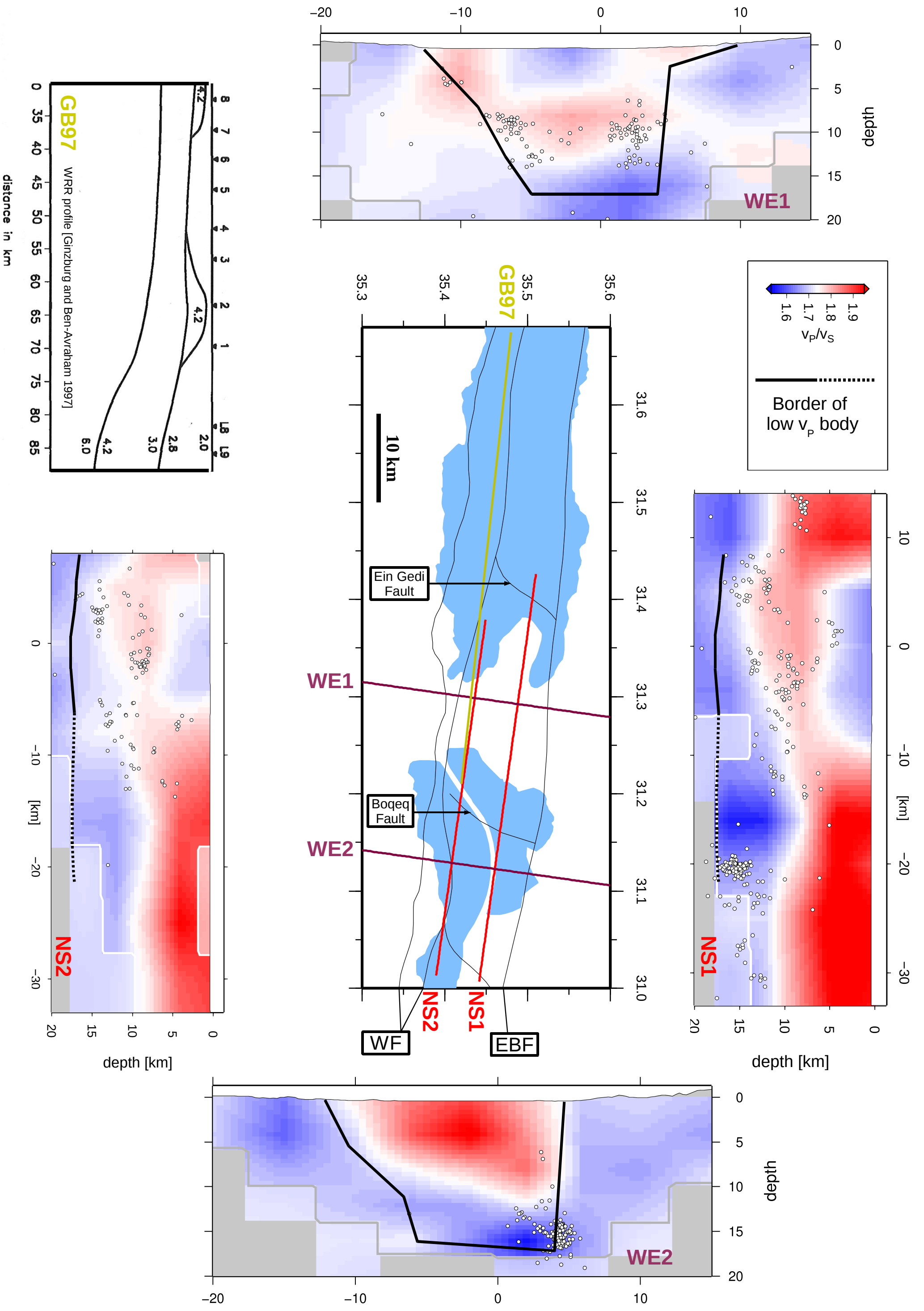

Figure 8.4: Summary of the 3-D tomography results through two WE profiles (WE1, WE2) and two NS profiles (NS1, NS2) compared to the NS wide angle reflection/refraction (WRR) profile of [Ginzburg and Ben-Avraham, 1997] (GB97). All profiles are indicated on the map in the center where the main faults are denoted as thin black lines. EBF: Eastern boundary fault, WF: Western faults.

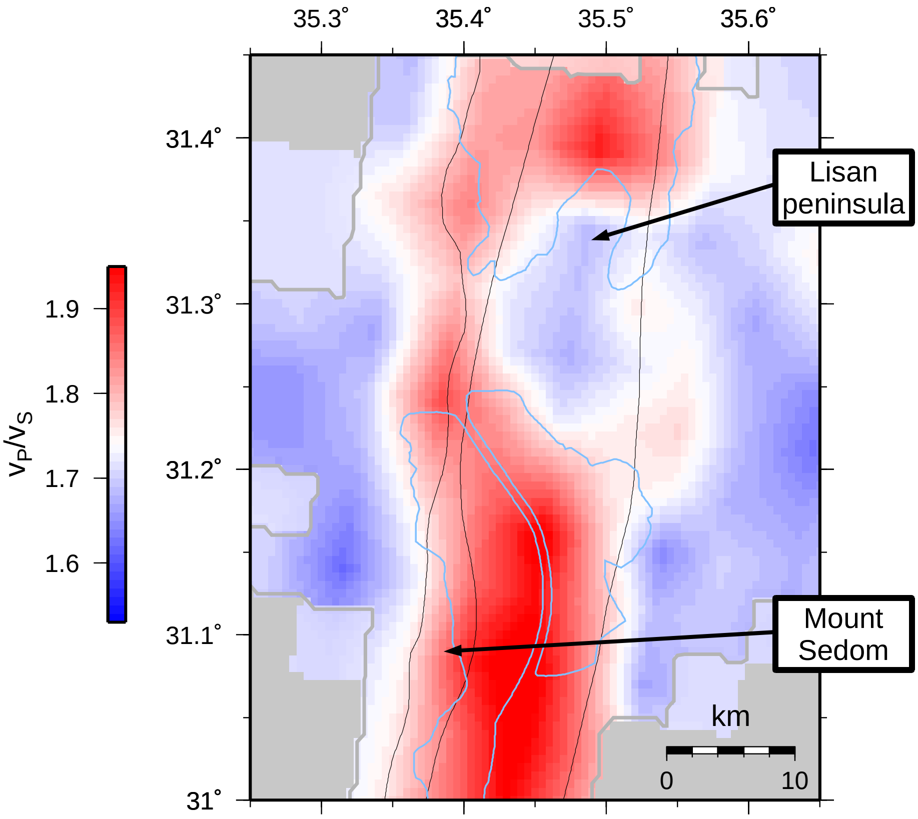

Figure 8.5: Map view of the model of v_P/v_S ratios in 2.5 km depth. The Lisan diapir is imaged through v_P/v_S ratios below the average. It extends from the eastern boundary about 12 km to the west where it is bordered on fluid containing sediments. Its maximal NS elongation is estimated to about 17 km.

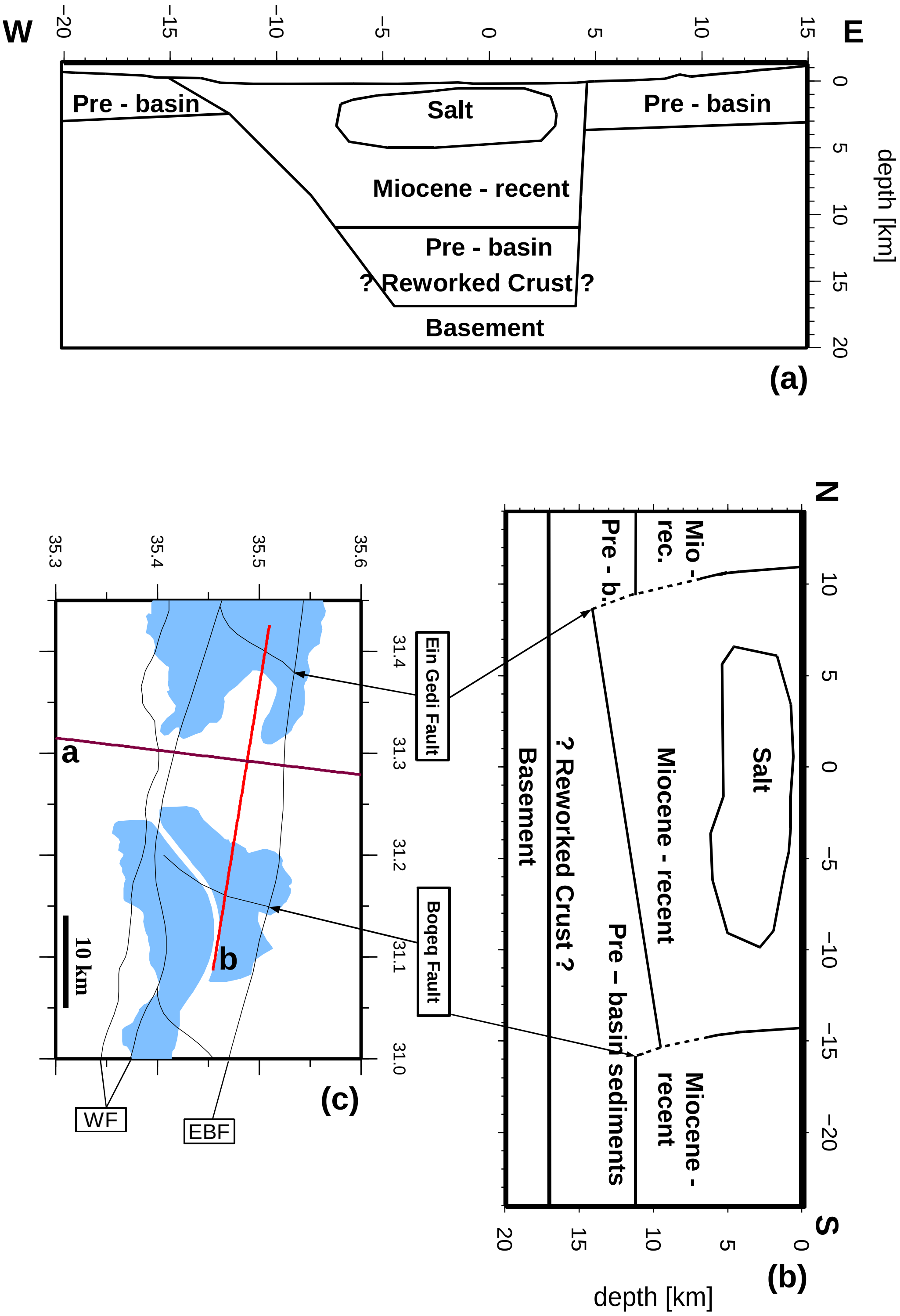

Figure 8.6: Interpretational sketch of the WE - depth section WE1 in Figure 8.4, (a). Interpretational sketch of the NS - depth profile NS1 in Figure 8.4, (b). Map with the location of the two profiles a and b and the main faults indicated as thin black lines. See text for details.

Chapter 9

Conclusions and Outlook

In this thesis local earthquake data from a temporary seismological network in the southern Dead Sea area have been analyzed within the project DESIRE. The first precise image of the micro seismicity distribution in the area is presented. Furthermore, local earthquakes are used for a v_P and v_P/v_S tomography to derive the structure of the sedimentary basin.

The comparison of the event location results from the 1-D inversion and the tomography reveals that for accurate determination of hypocentres and/or focal mechanisms in the study area, tomographic inversion (2-D or 3-D) is necessary.

Crustal earthquakes occur from 2 to 29 km depth, while large part of the seismicity is concentrated in the upper crust down to 20 km depth. The eastern boundary fault (EBF) of the Dead Sea Basin (DSB) is active over the entire study area except for a small gap related to the transverse Boqeq fault. The transverse faults are acting as barriers between different seismic regimes. South of the Boqeq fault the western boundary is inactive while the entire seismicity occurs at the eastern lower boundary of the sedimentary body. The largest events occurred here, their focal mechanisms represent the northwards transform motion of the Arabian plate along the Dead Sea Transform.

North of the Boqeq fault similar seismic activity occurs at both boundaries, displaying mainly small events with strike-slip mechanism and normal faulting in EW direction. These earthquakes, mostly related to the border between fluid containing sediments and "dry" rocks, represent the expected transfer of the motion in pull-apart basins from the eastern to the western boundary. Another change in the seismic regime seems to occur at the transverse Ein Gedi fault at the northern edge of the study area.

The tomography revealed an asymmetric basin with a vertical eastern boundary and an inclined western boundary for both v_P and v_P/v_S models resulting in width of 16 km at the surface and 10 km at the bottom. The basin is imaged through P velocity deviations from the starting model of up to 30 %. Its lower boundary, represented by a strong increase of the P velocities, was found at about 17 km depth for the entire study area. Through the model of v_P/v_S ratios more detailed features are imaged. The fluid containing sediments, deposited during the formation of the DSB, exhibit a thickness between 10 and 15 km. These sediments are displayed through high v_P/v_S ratios, except for the "dry" salt of the Lisan diapir. Thus, the Lisan salt diapir below the Lisan peninsula can be clearly identified through its low v_P/v_S ratios. The pre-basin sediments show low v_P/v_S ratios, indicating a lack of fluid content. Between the Boqeq and the Ein Gedi faults the boundary between pre-basin and younger sediments is inclined to the north, indicating different amount of faulting at the transverse normal faults.

The determination of focal mechanisms by classical methods using first motion polarities is limited due to the generally small size of the events. Thus, moment tensor inversion techniques need to be applied to improve the picture of the local stress regime.

The sedimentary basin is expected to show significant attenuation effects. Hence, the expansion of the tomography on attenuation should enlarge the image to more details.

Bibliography

A. Al-Zoubi and U. S. ten Brink. Salt diapirs in the Dead Sea basin and their relationship to Quaternary extensional tectonics. *Marine and Petroleum Geology*, 18:779–797, 2001.

A. Al-Zoubi, H. Shulman, and Z. Ben-Avraham. Seismic reflection profiles across the southern Dead Sea basin. *Tectonophysics*, 346:61–69, 2002.

F. Aldersons, Z. Ben-Avraham, A. Hofstetter, E. Kissling, and T. Al-Yazjeen. Lower-crustal strength under the Dead Sea basin from local earthquake data and rheological modeling. *Earth Plan. Sci. Lett.*, 214:129–142, 2003.

R. Avni, D. Bowman, A. Shapira, and A. Nur. Erroneous interpretation of historical documents related to the epicenter of the 1927 Jericho earthquake in the Holy Land. *Journal of Seismology*, 6:469–476, 2002.

A. Aydin and A. Nur. Evolution of pull-apart basins and their scale independence. *Tectonics*, 1, No. 1:91–105, 1982.

W. H. Bakun and W. B. Joyner. The M_L scale in central California. *Bull. Seismol. Soc. Am.*, 75 (5):1.827–1.843, 1984.

Y. Bartov. *A structural and paleogeographic study of the central Sinai faults and domes.* PhD thesis, Hebrew University, Jerusalem, 1974. in Hebrew.

Y. Bartov. Geological Photomap of Israel & Adjacent Areas. *Geological Survey of Israel, Scale 1:750 000*, 1990.

Z. B. Begin and G. Steinitz. Temporal and spatial variations of microearthquake activity along the Dead Sea Fault, 1984-2004. *Israel Journal of Earth Sciences*, 54:1–14, 2005.

Z. B. Begin, D. M. Steinberg, G. A. Ichinose, and S. Marco. A 40,000 year unchanging seismic regime in the Dead Sea rift. *Geology*, 33 (4):257–260, 2005.

Z. Ben-Avraham. Structural framework of the Gulf of Elat (Aqaba), northern Red Sea. *J. Geophys. Res.*, 90:703–726, 1985.

Z. Ben-Avraham. Development of asymmetric basins along continental transform faults. *Tectonophysics*, 215:209–220, 1992.

Z. Ben-Avraham and M. Lazar. The structure and development of the Dead Sea basin: Recent studies. *Geological Society of America*, 401:1–13, 2006.

Z. Ben-Avraham and G. Schubert. Deep "’drop down"’ basin in the southern Dead Sea. *Earth Plan. Sci. Lett.*, 251:254–263, 2006.

Z. Ben-Avraham and U. Ten Brink. Transverse faults and segmentation of basins within the Dead Sea Rift. *Journal of African Earth Sciences*, 8: 603–616, 1989.

Z. Ben-Avraham and M. D. Zoback. Transform-normal extension and asymmetric basins: An alternative to pull-apart models. *Geology*, 20:423–426, 1992.

Z. Ben-Avraham, R. Haenel, and H. Villinger. Heat flow through the Dead Sea rift. *Marine Geology*, 28:253–269, 1978. doi:10.1016/0025-3227(78)90021-X.

Z. Ben-Avraham, Z. Garfunkel, and M. Lazar. Geology and Evolution of the Southern Dead Sea Fault with Emphasis on Subsurface Structure. *Annu. Rev. Earth Planet. Sci.*, 36:357–387, 2008. doi: 10.1146/annurev.earth.36.031207.124201.

A. Ben-Menahem. Four thousand years of seismicity along the Dead Sea Rift. *J. Geophys. Res.*, 96:20195–20216, 1991.

E. A. Bisztricsany. A new method for the determination of the magnitude of earthquakes. *Geofiz. Kozlemen.*, 7:69–96, 1958.

S. Choi, H.-J. Götze, U. Meyer, M. Weber, and DESIRE Group. 3D density modelling of underground structures and spatial distribution of salt diapirism in the Dead Sea Basin. *Geophys. J. Int.*, 184:1131–1146, 2011. doi: 10.1111/j.1365-246X.2011.04939.x.

I. Csato, C. G. St. C. Kendall, A. E. M. Nairn, and G. R. Baum. Sequence stratigraphic interpretations in the southern Dead Sea basin, Israel. *Geol. Soc. Am. Bull.*, 108(11):1485–1501, 1997.

T. Diehl. *3-D Seismic Velocity Models of the Alpine Crust from Local Earthquake Tomography.* PhD thesis, University of Karlsruhe, 2008.

D. Eberhart-Phillips. Three-dimensional structure in northern California coast ranges from inversion of local earthquake arrival times. *Bull. Seismol. Soc. Am.*, 76:1025–1052, 1986.

D. Eberhart-Phillips. Three-dimensional P and S velocity structure in the Coalinga region, California. *J. Geophys. Res.*, 95(B10):15343–15363, 1990.

D. Eberhart-Phillips and A. J. Michael. Three-dimensional velocity structure, seismicity and fault structure in the Parkfield region, central California. *J. Geophys. Res.*, 98:15.737–15.758, 1993.

D. Eberhart-Phillips, W. D. Stanley, B. D. Rodriguez, and W. J. Lutter. Surface seismic and electrical methods to detect fluids related to faulting. *J. Geophys. Res.*, 100(B7):12919–12936, 1995.

Z. H. El-Isa, J. Mechie, C. Prodehl, J. Makris, and R. Rihm. A crustal structure study of Jordan derived from seismic refraction data. *Tectonophysics*, 138:235–253, 1987.

J. R. Evans, D. Eberhart-Phillips, and C. H. Thurber. *User's Manual for SIMULPS12 for Imaging* V_P *and* V_P/V_S*: A derivative of the "Thurber" tomographic inversion SIMUL3 for local earthquakes and Explosions.* U. S. Geological Survey, 1994. Open File Report 94-431.

M. Eyal, Y. Eyal, Y. Bartov, and G. Steinitz. The tectonic development of the western margin of the Gulf of Elat (Aqaba) rift. *Tectonophysics*, 80: 39–66, 1981.

Marie-Jose Fremont and Stephen D. Malone. High Precision Relative Locations of Earthquakes at Mount St. Helens, Washington. *J. Geophys. Res.*, 92(B10):10.223–10.236, 1987.

R. Freund, Z. Garfunkel, I. Zak, M. Goldberg, T. Weissbrod, and B. Derin. The shear along the Dead Sea rift. *Philosophical Transactions of the Royal Society of London*, 267:107–130, 1970.

U. Frieslander and Z. Ben-Avraham. Magnetic field over the Dead Sea and vicinity. *Marine and Petroleum Geology*, 6:148–160, 1989.

M. Gardosh, E. Kashai, S. Salhov, H. Shulman, and E. Tannenbaum. Hydrocarbon exploration in the southern Dead Sea area. In T. M. Niemi, Z. Ben-Avraham, and J. R. Gat, editors, *The Dead Sea, The lake and its setting*, volume 36, pages 57–72. Oxford monographs on Geology and Geophysics, 1997.

Z. Garfunkel. Internal structure of the Dead Sea leaky transform (rift) in relation to plate kinematics. *Tectonophysics*, 80:81–108, 1981.

Z. Garfunkel. The history and formation of the Dead Sea basin. In T. M. Niemi, Z. Ben-Avraham, and J. R. Gat, editors, *The Dead Sea, The lake and its setting*, volume 36, pages 36–56. Oxford monographs on Geology and Geophysics, 1997.

Z. Garfunkel and Z. Ben-Avraham. The structure of the Dead Sea basin. *Tectonophysics*, 266:155–176, 1996.

Z. Garfunkel and Z. Ben-Avraham. Basins along the Dead Sea Transform. *Mem. Mus. natn. Hist. nat.*, 186:607–627, 2001.

Z. Garfunkel and M. Beyth. Constraints on the structural development of Afar imposed by the kinematics of the major surrounding plates. In G. Yirgu and C. J. Ebinger and P. K. H. Maguire, editor, *The Structure and Evolution of the East African Rift System in the Afar Volcanic Province*, volume 259, pages 25–44. Geological Society of London, Special Publications, 2006.

A. Gilat. Oversized U-shaped canyon development at the edge of rotating blocks due to wrench faulting on margins of the Dead Sea graben. *Terra Nova*, 3:638–647, 1991.

Y. Gilboa, H. Fligelman, B. Derin, N. H. Foster, and E. Beaumont. Zohar-Kidod-Haqanaim fields: Israel, eastern Mediterranean basin. In N. H. Foster and E. A. Beaumont, editors, *Treatise of Petroleum Geology Atlas of Oil and Gas Fields*, pages 129–152. Am. Assoc. of Pet. Geol., Tulsa, Oklahoma, 1993.

A. Ginzburg and Z. Ben-Avraham. A seismic refraction study of the north basin of the Dead Sea, Israel. *Geophys. Res. Lett.*, 24:2063–2066, 1997.

A. Ginzburg, J. Makris, K. Fuchs, C. Prodehl, W. Kaminski, and U. Amitai. A seismic study of the crust and upper mantle of the Jordan – Dead Sea Rift and their transition toward the Mediterranean Sea. *J. Geophys. Res.*, 84:1569–1582, 1979.

A. Ginzburg, M. Reshef, Z. Ben-Avraham, and U. Schattner. The style of transverse faulting in the Dead Sea basin from seismic reflection data: The Amazyahu fault. *Israel Journal of Earth Sciences*, 55:129–139, 2007.

R. W. Girdler. The Dead Sea transform fault system. *Tectonophysics*, 180: 1–13, 1990.

J. S. Gomberg, K. M. Shedlock, and S. W. Roecker. The effect of S-wave arrival times on the accuracy of hypocenter estimation. *BSSA*, 80:1605–1628, 1990.

F. Gomez, M. Meghraoui, A. N. Darkal, F. Hijazi, M. Mouty, Y. Suleiman, R. Sbeinati, R. Darawcheh, R. Al-Ghazzi, and M. Barazangi. Holocene faulting and earthquake recurrence along the Serghaya branch of the Dead Sea fault system in Syria and Lebanon. *Geophys. J. Int.*, 153:658–674, 2003.

C. Haberland, A. Rietbrock, D. Lange, K. Bataille, and T. Dahm. Structure of the seismogenic zone of the southcentral Chilean margin revealed by local earthquake traveltime tomography. *J. Geophys. Res.*, 114, 2009. doi:10.1029/2008JB005802.

Christian Haberland. *Die Verteilung der Absorption seismischer Wellen in den westlichen Zentralen Anden.* PhD thesis, Freie Universität Berlin, 1999. Berliner Geowissenschaftliche Abhandlungen, Reihe B, Band 35.

Y. Hamiel, R. Amit, Z. B. Begin, S. Marco, O. Katz, A. Salamon, E. Zilbermann, and N. Porat. The Seismicity along the Dead Sea Fault during the Last 60 000 Years. *Bull. Seismol. Soc. Am.*, 99:2020–2026, 2009. doi:10.1785/0120080218.

R. D. Hatcher, I. Zeiz, R. D. Reagan, and M. Abu-Ajameh. Sinistral strike-slip motion of the Dead Sea rift: confirmation from new magnetic data. *Geology*, 9:458–462, 1981.

A. Hofstetter, C. Dorbath, M. Rybakov, and V. Goldshmidt. Crustal and upper mantle structure across the Dead Sea rift and Israel from teleseismic P-wave tomography and gravity data. *Tectonophysics*, 327:37–59, 2000.

A. Hofstetter, H. K. Thio, and G. Shamir. Source mechanism of the 22/11/1995 Gulf of Aqaba earthquake and its aftershock sequence. *Journal of Seismology*, 7:99–114, 2003.

R. Hofstetter, Y. Klinger, A.-Q. Amrat, L. Rivera, and L. Dorbath. Stress tensor and focal mechanisms along the Dead Sea fault and related structural elements based on seismological data. *Tectonophysics*, 429:165–181, 2007.

R. Hofstetter, Y. Gitterman, V. Pinsky, N. Kraeva, and L. Feldman. Seismological observations of the northern Dead Sea basin earthquake on 11 February 2004 and its associated activity. *Israel Journal of Earth Sciences*, 57:101–124, 2008. doi: 10.1560/IJES.57.2.101.

A. Horowitz. Palynological evidence for the age and rate of sedimentation along the Dead Sea Rift, and structural implications. *Tectonophysics*, 141: 107–115, 1987.

S. Husen. *Local Earthquake Tomography of a Convergent Margin, North Chile*. PhD thesis, Mathematisch-Naturwissenschaftliche Fakultät, Universität Kiel, 1999.

S. Husen, E. Kissling, E. Flueh, and G. Asch. Accurate hypocentre determination in the seismogenic zone of the subducting Nazca Plate in northern Chile using a combined on-/offshore network. *Geophys. J. Int.*, 138:687–701, 1999.

S. Husen, E. Kissling, and E. R. Flueh. Local earthquake tomography of shallow subduction in north Chile: A combined onshore and offshore study. *JGR*, 105(B12):28183–28198, 2000.

S. Joffe and Z. Garfunkel. The plate kinematics of the circum Red Sea — A reevaluation. *Tectonophysics*, 141:5–22, 1987.

V. Karabacak, E. Altunel, M. Meghraoui, and H. S. Akyüz. Field evidences from northern Dead Sea Fault Zone (South Turkey): New findings for the initiation age and slip rate. *Tectonophysics*, 480:172–182, 2010.

E. L. Kashai and P. F. Croker. Structural geometry and evolution of the Dead Sea – Jordan rift system as deduced from new subsurface data. *Tectonophysics*, 141:33–60, 1987.

B. Kaypak. Three-dimensional Vp and Vp/Vs structure of the upper crust in the Erzincan basin (eastern Turkey). *J. Geophys. Res.*, 113:20pp, 2008. doi: 10.1029/2006JB004905.

P. Kearey and F. J. Vine. *Global Tectonics*. Blackwell Science, Oxford, 1995.

E. Kissling. Geotomography with local earthquake data. *Rev. of Geophys.*, 26 (4):659–698, 1988.

E. Kissling, W. L. Ellworth, D. Eberhardt-Phillips, and U. Kradolfer. Initial reference models in local earthquake tomography. *J. Geophys. Res.*, 99: 19352–19646, 1994.

E. Kissling, U. Kradolfer, and H. Maurer. VELEST User's Guide - Short Introduction. Technical report, ETH Zürich, 1995a.

E. Kissling, S. Solarino, and M. Cattaneo. Improved seismic velocity reference model from local earthquake data in Northwestern Italy. *Terra Nova*, 7: 528–534, 1995b.

E. Kissling, S. Husen, and F. Haslinger. Model parametrization in seismic tomography: a choice of consequence for the solution quality. *Phys. Earth Planet. Inter.*, 123:89–101, 2001.

Y. Klinger, L. Rivera, H. Haessler, and J.-C. Maurin. Active Faulting in the Gulf of Aqaba: New Knowledge from the M_w7.3 Earthquake of 22 November 1995. *Bull. Seismol. Soc. Am.*, 89 (4):1025–1036, 1999.

Y. Klinger, J. P. Avouac, N. Abou Karaki, L. Dorbath, D. Bourles, and J. L. Reyss. Slip rate on the Dead Sea transform fault in northern Araba valley, (Jordan). *Geophys. J. Int.*, 142(3):755–768, 2000a.

Y. Klinger, J.P. Avouac, L. Dorbath, N. Abou Karaki, and N. Tisnerat. Seismic behaviour of the Dead Sea fault along Araba valley, Jordan. *Geophys. J. Int.*, 142:769–782, 2000b.

Dietrich Lange. *The South Chilean Subduction Zone between* 41°- 43.5° *S: Seismicity, Structure and State of Stress*. PhD thesis, Universität Potsdam, Potsdam, Germany, 2008.

B. D. Larsen, Z. Ben-Avraham, and H. Shulman. Fault and salt tectonics in the southern Dead Sea basin. *Tectonophysics*, 346:71–90, 2002.

T. Lay and T. C. Wallace. *Modern Global Seismology*, volume 58 of *International Geophysics*. Academic Press, San Diego, 1995.

M. Lazar, Z. Ben-Avraham, and U. Schattner. Formation of sequential basins along a strike-slip fault-Geophysical observations from the Dead Sea basin. *Tectonophysics*, 421(5):53–69, 2006.

M. Le Beon, Y. Klinger, A. Q. Amrat, A. Agnon, L. Dorbath, G. Baer, J.-C. Ruegg, O. Charade, and O. Mayyas. Slip rate and locking depth from GPS profiles across the southern Dead Sea Transform. *J. Geophys. Res.*, 113: 1–19, 2008. doi: 10.1029/2007JB005280.

X. LePichon and J. M. Gaulier. The rotation of Arabia and the Levant fault system. *Tectonophysics*, 153:271–294, 1988.

Nils Maercklin. *Seismic structure of the Arava Fault, Dead Sea Transform*. PhD thesis, Universität Potsdam, Potsdam, Germany, 2004.

S. Marco, M. Stein, and A. Agnon. Long-term earthquake clustering: A 50,000-year paleoseismic record in the Dead Sea Graben. *J. Geophys. Res.*, 101:6179–6191, 1996.

M. Massa. *Waveforms analysis to improve earthquake location procedures: Theory and applications*. PhD thesis, University of Genoa, 2005.

D. P. McKenzie, D. Davies, and P. Molnar. Plate tectonics of the Red Sea and East Africa. *Nature*, 224:125–133, 1970.

J. Mechie, K. Abu-Ayyash, Z. Ben-Avraham, R. El-Kelani, I. Qabbani, M. Weber, and DESIRE Group. Crustal structure of the southern Dead

Sea basin derived from project DESIRE wide-angle seismic data. *Geophys. J. Int.*, 178, 2009. doi: 10.1111/j.1365-246X.2009.04161.x.

W. Menke. *Geophysical Data Analysis: Discrete Inverse Theory*. Academic Press, San Diego, 1989.

N. M. Meqbel. *The electrical conductivity structure of the Dead Sea Basin derived from 2D and 3D inversion of magnetotelluric data*. PhD thesis, Freie Universität Berlin, 2009.

D. Neev and J. K. Hall. Geophysical investigations in the Dead Sea. *Sediment. Geol.*, 23:209–238, 1979.

T. M. Niemi, Z. Ben-Avraham, and J. R. Gat. *The Dead Sea – The Lake and its Setting*, volume 36 of *Oxford Monographs on Geology and Geophysics*. Oxford University Press, Oxford, 1997.

C. C. Paige and M. A. Saunders. LSQR: An Algorithm for Sparse Linear Equations and Sparse Least Squares. In *ACM Transactions on Mathematical Software*, volume 8, pages 43–71. ACM Press, 1982.

M. Paschke. Erstellung eines P-Geschwindigkeitsmodells der oberen Kruste im Bereich des Toten Meeres mit tomographischen Methoden. Diplomarbeit, Universität Potsdam, Institut für Geowissenschaften, GFZ Potsdam, Geophysikalische Tiefensondierung, 2009.

M. Paschke, M. Stiller, T. Ryberg, M. Weber, and DESIRE Group. The shallow P-velocity structure of the southern Dead Sea basin derived from near-vertical incidence reflection seismic data in project DESIRE. *Geophys. J. Int.*, 2010. submitted.

G. L. Pavlis. Appraising earthquake hypocenter location errors: A complete, practical approach for single-event locations. *Bull. Seismol. Soc. Am.*, 76: 1699–1717, 1986.

G. L. Pavlis and J. R. Booker. A study of the importance on nonlinearity in the inversion of earthquake arrival time data for velocity structure. *J. Geophys. Res.*, 88 (B6):5047–5055, 1983.

A. G. Petrunin and S. V. Sobolev. Three-dimensional numerical models of the evolution of pull-apart basins. *Phys. Earth Planet. Inter.*, 171:387–399, 2008.

G. Poupinet, W.L. Ellsworth, and J. Frechet. Monitoring Velocity Variations in the Crust Using Earthquake Doublet: An Application to the Calveras Fault, California. *J. Geophys. Res.*, 89(B7):5.719–5.731, 1984.

A. M. Quennel. The structural and geomorphic evolution of the Dead Sea rift. *Q.J. Geol. Soc. London*, 114:2–24, 1958.

N. Rawlinson and M. Sambridge. SEISMIC TRAVELTIME TOMOGRAPHY OF THE CRUST AND LITHOSPHERE. *Advances in Geophysics*, 46:81–198, 2003.

P. A. Reasenberg and D. Oppenheimer. Fpfit, fpplot and fppage: Fortran computer programs for calculating and displaying earthquake fault-plane solutions. Open-file report, U. S. Geol. Survey, 1985.

R. Reilinger, S. McClusky, P. Vernant, S. Lawrence, S. Ergintav, R. Cakmak, H. Ozener, F. Kadirov, I. Guliev, R. Stepanyan, M. Nadariya, G. Hahubia, S. Mahmoud, K. Sakr, A. Ar-Rajehi, D. Paradissis, A. Al-Aydrus, M. Prilepin, T. Guseva, E. Evren, A. Dmitrotsa, S. V. Filikov, F. Gomez, R. Al-Ghazzi, and G. Karam. GPS constraints on continental deformation in the Africa-Arabia-Eurasia continental collision zone and implications for the dynamics of plate interactions. *J. Geophys. Res.*, 111:26 pp, 2006. doi:10.1029/2005JB004051.

C. F. Richter. *Elementary Seismology.* A Series of books in geology. Freeman and Co, San Francisco, 1958.

Y. Rotstein and E. Arieh. Tectonic implications of recent microearthquake data from Israel and adjacent areas. *Earth Plan. Sci. Lett.*, 78:237–244, 1986.

P. A. Rydelek and I. S. Sacks. Testing the completeness of earthquake catalogues and the hypothesis of self-similarity. *Nature*, 337:251–253, 1989.

A. Salamon. Patterns of seismic sequences in the Levant-interpretation of historical seismicity. *Journal of Seismology*, 14 (2):339–367, 2010.

A. Salamon, A. Hofstetter, Z. Garfunkel, and H. Ron. Seismicity of the eastern Mediterranean region: Perspective from the Sinai subplate. *Tectonophysics*, 263:293–305, 1996.

Bernd Schurr. *Seismic Structure of the Central Andean Subduction Zone from Local Earthquake Data*. PhD thesis, Freie Universität Berlin, Berlin, Germany, 2000.

G. Shamir. The active structure of the Dead Sea Depression. *Geological Society of America*, Special Paper 401:15–32, 2006.

A. Shapira and L. Feldmann. Microseismicity of three locations along the Jordan Rift. *Tectonophysics*, 141:89–94, 1987.

P. V Sharma. *Environmental and engineering geophysics*. Cambridge University Press, Cambridge, 1997.

J. Smit, J.-P. Brun, X. Fort, S. Cloetingh, and Z. Ben-Avraham. Salt tectonics in pull-apart basins with application to the Dead Sea Basin. *Tectonophysics*, 449:1–16, 2008.

J. Smit, J.-P. Brun, S. Cloetingh, and Z. Ben-Avraham. The rift-like structure and asymmetry of the Dead Sea Fault. *Earth Plan. Sci. Lett.*, 290:74–82, 2010.

S. L. Solov'yev. Seismicity of Sakhalin. *Bull. Earthquake Res. Inst. Tokyo Univ.*, 43:95–102, 1965.

U. S. ten Brink, Z. Ben-Avraham, R. E. Bell, M. Hassouneh, D. F. Coleman, G. Andreasen, G. Tibor, and B. Coakley. Structure of the Dead Sea Pull-Apart Basin From Gravity Analyses. *J. Geophys. Res.*, 98, No. B12:21877–21894, 1993.

C. H. Thurber. Earthquake locations and three-dimensional crustal structure in the Coyote Lake area, Central California. *J. Geophys. Res.*, 88:8.226–8.236, 1983.

C. H. Thurber. Nonlinear earthquake location: Theory and examples. *Bull. Seismol. Soc. Am.*, 75 (3):779–790, 1985.

C. H. Thurber. Hypocenter-velocity structure coupling in local earthquake tomography. *Physics of the Earth and Planetary Interiors*, 75:55–62, 1992.

C. H. Thurber. Local earthquake tomography: velocities and V_P/V_S-theory. In H. M. Iyer and K. Hirahara, editors, *Seismic Tomography: Theory and practice*, chapter 20. Chapman and Hall, London, 1993.

D. Toomey and G. Foulger. Tomographic inversion of local earthquake data from the Hengill-Grensdalur central volcano complex, Iceland. *J. Geophys. Res.*, 94:17497–17510, 1989.

J. Um and C. H. Thurber. A fast algorithm for two-point ray tracing. *Bull. Seismol. Soc. Am.*, 77:972–986, 1987.

T. van Eck and A. Hofstetter. Microearthquake activity in the Dead Sea region. *Geophys. J. Int.*, 99:605–620, 1989.

T. van Eck and A. Hofstetter. Fault geometry and spatial clustering of microearthquakes along the Dead Sea – Jordan rift fault zone. *Tectonophysics*, 180:15–27, 1990.

F. Waldhauser. *hypoDD – A Program to Compute Double-Difference Hypocenter Locations (hypoDD version 1.0 - 03/2001).* U.S. Geol. Survey, 2001.

Felix Waldhauser and William L. Ellsworth. A double - difference earthquake location algorithm: Method and application to the northern Hayward faults, California. *Bull. Seismol. Soc. Am.*, 90:1353–1368, 2000.

M. Weber and DESERT Group. Anatomy of the Dead Sea Transform from lithospheric to microscopic scale. *Rev. of Geophys.*, 47, 2009. doi:10.1029/2008RG000264.

S. G. Wesnousky. Seismicity as a function of cumulative geologic offset: Some observations from southern California. *Bull. Seismol. Soc. Am.*, 80: 1374–1381, 1990.

I. Zak. *The geology of Mt. Sedom.* PhD thesis, The Hebrew University, Jerusalem, 1967.

I Zak and R. Freund. Asymmetry and basin migration in the Dead Sea Rift. *Tectonophysics*, 80:27–38, 1981.

Appendix A

Station List

Table A.1: Station type (broadband (BB) or shortperiod (SP)) and positions with recording time and number of P- and S-Picks.

station	type	LAT [°N]	LON [°E]	elevation [m]	rec. time [month]	# Picks
Jordan						
JB01	BB	31.2371	35.4792	-331	18	896
JB02	BB	31.2519	35.4652	-336	18	118
JB04	BB	31.2501	35.4282	-382	18	765
JB07	BB	31.2916	35.4798	-330	18	1175
JB10	BB	31.3388	35.4946	-363	18	1199
JB12	BB	31.3724	35.5003	-399	18	895
JB15	BB	31.2474	35.5435	-211	18	573
JB18	BB	31.2515	35.6216	411	18	380
JB19	BB	31.2331	35.6456	546	18	658
JB21	BB	31.1989	35.6688	756	18	527
JB25	BB	31.0892	35.5207	-346	7	94
JB29	BB	31.3001	35.5657	-160	18	304
JB37	BB	31.3890	35.6746	808	18	575
JB39	BB	31.1947	35.6076	680	18	701

JB41	BB	31.2727	35.5425	-243	18	194
JB42	BB	31.3291	35.4958	-387	11	482
JS03	SP	31.2588	35.4438	-232	18	1122
JS05	SP	31.2378	35.4022	-389	18	628
JS06	SP	31.2753	35.4694	-318	18	1181
JS08	SP	31.3070	35.4858	-356	18	1164
JS09	SP	31.3234	35.4852	-352	18	495
JS11	SP	31.3513	35.5083	-403	18	709
JS13	SP	31.2349	35.5028	-334	18	223
JS14	SP	31.2404	35.5248	-288	18	441
JS17	SP	31.2509	35.5953	234	18	497
JS20	SP	31.2131	35.6625	642	18	511
JS22	SP	31.1945	35.6911	751	18	534
JS23	SP	31.2213	35.6733	665	18	593
JS24	SP	31.1813	35.7021	1034	18	241
JS26	SP	31.1718	35.5362	-361	18	297
JS27	SP	31.1917	35.5350	-361	18	193
JS28	SP	31.3030	35.5375	-338	18	401
JS31	SP	31.3307	35.5812	119	18	472
JS33	SP	31.3346	35.6422	991	18	659
JS35	SP	31.3791	35.6964	902	18	702
JS36	SP	31.4219	35.7389	871	18	10
JS40	SP	31.1165	35.6301	1096	18	217
Israel						
IB09	BB	31.2312	35.3966	-390	18	715
IB11	BB	31.2010	35.4202	-390	18	597
IB13	BB	31.1712	35.4440	-395	18	534
IB15	BB	31.1364	35.4553	-395	18	114
IB17	BB	31.1010	35.4523	-395	18	197
IB19	BB	31.0669	35.4358	-395	18	106
IB21	BB	31.0208	35.4205	-350	18	106

IB22	BB	31.0626	35.3647	-270	8	111
IB25	BB	31.1302	35.3636	-320	8	333
IB31	BB	31.3166	35.3474	-100	18	820
IB36	BB	30.9313	35.3896	-331	10	45
IB38	BB	31.4499	35.3809	-300	10	85
IB44	BB	31.7527	35.4626	-320	10	61
IS01	SP	31.2777	35.1261	533	18	177
IS02	SP	31.2605	35.2345	614	18	343
IS08	SP	31.2353	35.3763	-391	18	440
IS10	SP	31.2159	35.4086	-386	18	705
IS12	SP	31.1860	35.4321	-385	18	383
IS14	SP	31.1540	35.4522	-395	18	134
IS16	SP	31.1192	35.4555	-395	18	353
IS20	SP	31.0521	35.4261	-395	18	316
IS26	SP	31.1481	35.3272	36	5	293
IS27	SP	31.1452	35.2840	100	5	300
IS32	SP	31.3535	35.3540	-270	8	363
IS34	SP	31.0747	35.3327	0	8	179
IS35	SP	30.9909	35.4134	-374	18	239
IS37	SP	31.4162	35.3806	-390	10	110
IS40	SP	31.1507	35.3651	-363	10	59
IS41	SP	30.7671	35.2879	-150	10	20
IS42	SP	31.5732	35.3995	-250	10	193
IS43	SP	31.6782	35.4354	-313	10	69
Israel Network (ISN) Stations						
AMAZ	SP	31.5491	34.9123	151	18	18
DSI0	SP	31.5920	35.3930	15	18	142
MZD0	SP	31.3083	35.3628	-282	18	39
YTR0	SP	31.3626	35.1160	905	18	60
ZFRI	SP	30.5540	35.1782	-37	18	27

Jordan Network (JSO) Stations						
DHLJ	SP	30.8200	35.4020	-80	18	23
LISJ	SP	31.2400	35.4810	-327	18	17
QTRJ	SP	31.3000	36.0100	876	18	34
MKRJ	SP	31.5520	35.6410	815	18	16

Appendix B

Station corrections

Table B.1: Station corrections for the DESIRE stations from the 1-D inversion in Chapter 5. P delay of station IB31* was constraint to zero.

station name	P corr. [s]	S corr. [s]	station name	P corr. [s]	S corr. [s]
IB31*	0.0	-0.18	IS37	-0.07	0
IS10	0.49	1.11	IB38	-0.26	-0.73
IS12	0.48	1.12	IS40	0.14	0.01
IB22	0.16	0.34	IS41	-0.28	-0.35
IS32	-0.05	0.07	IS42	-0.75	-1.46
IS08	0.49	1.03	IB36	0.04	0.56
IS14	0.39	1.2	IS43	-1.01	-1.2
IS34	-0.19	-0.56	IB44	-1.08	-1.36
IB25	0.22	0.42	JS11	0.09	0.19
IB09	0.48	1.06	JS09	0.18	0.31
IB11	0.49	1.11	JS08	0.21	0.34
IB13	0.46	1.28	JS06	0.27	0.44
IB15	0.39	1.12	JS28	-0.13	-0.01
IS16	0.34	1.08	JS17	-0.58	-1.27
IB17	0.32	0.99	JB07	0.23	0.42

IB19	0.31	1.25	JB12	0.05	0.44
IS20	0.27	1.19	JB04	0.43	0.9
IB21	0.26	0.97	JB21	-0.75	-1.97
IS35	0.17	0.91	JB41	-0.14	-0.13
IS27	-0.26	-0.88	JB02	0.31	0.5
IS26	-0.11	-0.55	JB01	0.26	0.44
IS02	-0.3	-1.17	JB10	0.14	0.23
IS01	-0.48	-1.45	JB15	-0.19	-0.35
JB19	-0.72	-1.84	JS22	-0.82	-2.08
JB18	-0.65	-1.55	JS23	-1.04	-2.24
JS03	0.37	0.57	JS24	-0.85	-2.3
JS05	0.51	1.17	JS26	-0.43	-0.93
JS13	0.29	0.52	JS27	-0.2	-0.01
JB25	-0.55	-1.09	JS31	-0.33	-1.01
JB39	-0.65	-1.64	JS33	-0.64	-1.7
JB29	-0.23	-0.51	JB37	-0.75	-1.71
JS36	-1.61	-3.03	JS40	-0.96	-2.38
JS14	-0.03	0.02	JS35	-0.87	-2.06
JS20	-0.77	-1.99	JB42	0.16	0.27

Appendix C

Logfile HypoDD

```
  IT   EV  CT  CC    RMSCT      RMSCC   RMSST   DX   DY   DZ   DT   OS  AQ
        %   %   %   ms     %   ms     %    ms    m    m    m   ms    m
 1  1 100 100 100  180  -4.1  242  -6.7   644  149  321  683   62    0   0
 2  2 100 100 100  180   0.0  242  -0.1   641    7   31   74    4    0   0
 3  3 100 100 100  180   0.0  242   0.0   641    1    2   11    2    0   0
 4  4 100 100 100  180   0.0  242   0.0   641    0    0    1    0    0   0
 5  5 100 100 100  180   0.0  242   0.0   641    0    0    0    0    0   0
 6  6 100  99 100  129 -28.4  242  -0.1   647   25   61   77   12    0   0
 7  7 100  99 100  126  -2.2  242   0.2   647   16   31   49    7    0   0
 8  8 100  98 100  125  -1.2  242   0.0   656   18   28   45    7    0   0
 9  9 100  98 100  124  -0.6  242  -0.1   657   15   22   48    7    0   0
10 10 100  98 100  123  -0.5  242   0.1   655   16   31   33    6    0   0
11 11  99  98  95  356 188.6  150 -38.0   552  146  146  423   74   51   0
12 12  98  91  95  243 -31.9  114 -24.1   511   36   61  108   25   28   0
13 13  98  91  94  201 -17.0   98 -14.0   507   22   37   67   14   28   0
14 14  98  90  94  191  -5.0   92  -6.4   509   18   26   50    9   28   0
15 15  98  90  94  189  -1.3   89  -3.5   509   17   22   34    8   28   0
16 16  98  90  76  185  -2.1   24 -72.5   391    9   15   21    5   28   0
17 17  98  90  75  183  -1.0   20 -19.0   380    6   11   12    4   28   0
18 18  98  90  74  182  -0.7   17 -12.0   380    4   10   10    3   28   0
19 19  98  90  73  182   0.0   16 -10.0   386    3    6    9    3   28   0
20 20  98  90  73  181  -0.2   14  -8.6   387    3    6    7    2   28   0
21 21  98  90  51  182   0.2   11 -21.6   392    3    5    8    2   28   0
22 22  98  90  50  181  -0.4    9 -17.7   388    3    5    6    1   28   0
23 23  98  90  50  181  -0.1    9  -6.5   398    2    3    5    1   28   0
24 24  98  90  49  181   0.1    8  -4.8   395    2    3    4    1   28   0
25 25  98  90  49  181  -0.1    8  -4.2   397    2    2    4    1   28   0
```

Figure C.1: Logfile of HypoDD.

Danksagung

Günter Asch gilt als meinem Betreuer mein erster Dank. Er war ein erfahrener Lehrer im Feld und auch danach war er immer für mich da, wenn es ihm möglich war.

Michael Weber ist der ”Vater” von DESIRE und hat als Chef an der guten Stimmung in der Sektion 2.2 des GFZ einen großen Anteil. Außerdem stand seine Tür immer offen, wenn ich Fragen hatte. Des weiteren steht er freundlicherweise als Zweitkorrektor zur Verfügung.

Die Arbeit wäre in dieser Form nicht möglich gewesen ohne Christian Haberland. Seine umfangreiche Erfahrung auf verschiedenen Gebieten hat die Arbeit außerordentlich bereichert. Außerdem stammt ein Teil der benutzten Software von ihm. Dafür einen besonders herzlichen Dank.

Eine große Hilfe waren die Studenten, die mich bei der Datenauswertung unterstützt haben. Besonders Oliver hat beim akribischen Suchen auch der kleinsten Events nie die Geduld verloren.

Ariane war, trotz widrigster Umstände, eine fröhliche, hilfsbereite Büronachbarin, die für ausreichend Frischluft sorgte. Sie hat wesentlichen Anteil daran, dass ich immer gern ans GFZ kam. Außerdem hat sie mir bei einigen Abbildungen geholfen.

During all my field trips the GII in Tel Aviv was a great support especially Rami Hofstetter. Furthermore I used their software for the data processing.

Jacek hatte die zweifelhafte Ehre das gesamte Manuskript Korrektur lesen zu dürfen und in halbwegs verständliches Englisch zu bringen. Dafür ein besonderer Dank an ihn. Für weiteres Korrektur lesen und nicht nur fachliche Diskussionen in der Kaffeerunde danke ich Jim Mechie, Trond Ryberg und Christian Haberland. Bei allen computertechnischen Fragen halfen mir mit

Kompetenz und Geduld Matthias Wanjek und Christof Lendl.

Ich danke allen weiteren Beteiligten bei den Feldarbeiten, besonders Ayman Mohsen und Benjamin Heit. Alle im Feld verwendeten Geräte wurden vom Geophysikalischen Instrumenten Pool Potsdam (GIPP) vorbereitet und zur Verfügung gestellt. Dafür geht ein besonderer Dank an Jens Bribach. Das Projekt DESIRE wurde finanziert von der Deutschen Forschungsgesellschaft (DFG).

Meine Familie war mir eine große Unterstützung auf dem langen Weg bis hierher. Ohne ihre Hilfe, Geduld und Liebe hätte ich es nicht geschafft. Danke.

Curriculum Vitae

For reasons of data protection, the curriculum vitae is not included in the online version.